MOUNTAIN-PLAINS CONSORTIUM

MPC 24-518 | N. Raine and M.W. Halling

EVALUATION OF DURABILITY AND STRUCTURAL PERFORMANCE OF CONCRETE WITH EMBEDDED INDUCTIVE COILS

MOUNTAIN-PLAINS CONSORTIUM REGION 8

A University Transportation Center sponsored by the U.S. Department of Transportation serving the Mountain-Plains Region. Consortium members:

Colorado State University
North Dakota State University
South Dakota State University
University of Colorado Denver
University of Denver
University of Utah
Utah State University
University of Wyoming

Technical Report Documentation Page

1. Report No.	2. Government Accession No.	3. Recipient's Catalog No.
MPC-562		

4. Title and Subtitle	5. Report Date
Evaluation of Durability and Structural Performance of Concrete with Embedded Inductive Coils	March 2024
	6. Performing Organization Code

7. Author(s)	8. Performing Organization Report No.
Nathan J. Raine Marvin W. Halling	MPC 24-518

9. Performing Organization Name and Address	10. Work Unit No. (TRAIS)
Dept. of Civil and Environmental Engineering Utah State University 4110 Old Main Hill Logan, UT 84321	11. Contract or Grant No.

12. Sponsoring Agency Name and Address	13. Type of Report and Period Covered
Mountain-Plains Consortium North Dakota State University PO Box 6050, Fargo, ND 58108	Final Report
	14. Sponsoring Agency Code

15. Supplementary Notes

Supported by a grant from the US DOT, University Transportation Centers Program

16. Abstract

Current electric vehicles (EVs) suffer from several drawbacks that prevent widespread public acceptance. Inductive power transfer systems (IPTS) seek to address range and battery life issues by allowing EVs to charge while in transit. This advancement would allow future infrastructure to meet rising demands while simultaneously making EVs more accessible and user friendly.

In order to investigate the durability of the technology, two full size slabs were cast with working electronics and structurally tested while monitoring electrical parameters. The primary focus of this work was to study the durability of the concrete slabs. The secondary focus of the study was to determine how well the technology works under a variety of realistic loadings.

Both slabs with the embedded IPTS were subjected to high cycle fatigue loading and then underwent monotonic loading to failure in order to confirm material properties.

During the fatigue testing both slabs experienced minor cracking, however, it was not until the upper limits of static testing that major failures occurred. Throughout the experiment the embedded IPTS proved to be resilient and suffered little degradation in performance. The IPTS embedded in these concrete pads demonstrated reasonable durability with promise as a viable solution to the growing needs of the EV infrastructure.

17. Key Word	18. Distribution Statement
coils (electromagnetism), durability, electric power transmission, electric vehicle charging, inductance, load tests, paving, portland cement concrete	Public distribution

19. Security Classif. (of this report)	20. Security Classif. (of this page)	21. No. of Pages	22. Price
Unclassified	Unclassified	120	n/a

Form DOT F 1700.7 (8-72) Reproduction of completed page authorized

Evaluation of Durability and Structural Performance of Concrete with Embedded Inductive Coils

Nathan J. Raine
Marvin W. Halling

Department of Civil and Environmental Engineering
Utah State University
Logan, Utah 84321

March 2024

Disclaimer

The contents of this report reflect the views of the authors, who are responsible for the facts and the accuracy of the information presented. This document is disseminated under the sponsorship of the Department of Transportation, University Transportation Centers Program, in the interest of information exchange. The U.S. Government assumes no liability for the contents or use thereof.

TABLE OF CONTENTS

LIST OF TABLES

LIST OF FIGURES

LIST OF ABBREVIATIONS

AASHTO	American Association of State Highway Transportation Officials
ACI	American Concrete Institution
ASCE	American Society of Civil Engineers
E	Modulus of Elasticity
eRoad	Electrified Roadway
EV	Electric Vehicle
GFRP	Glass Fiber Reinforced Polymer
IPTS	Inductive Power Transfer System
LRFD	Load and Resistance Factor Design
LVDT	Linear Variable Differential Transducer
MOR	Modulus of Rupture
OSB	Oriented Strand Board
S-N	Stress to Number of Cycles to Failure
SMASH	Structural, Materials and Structural Health Laboratory
WPT	Wireless Power Transfer
σ	Compressive Strength of Concrete

EXECUTIVE SUMMARY

Current electric vehicles (EVs) suffer from several drawbacks that prevent widespread public acceptance. Inductive power transfer systems (IPTS) seek to address range and battery life issues by allowing EVs to charge while in transit. This advancement would allow future infrastructure to meet rising demands while simultaneously making EVs more accessible and user friendly.

In order to investigate the durability of the technology, two full size slabs were cast with working electronics and structurally tested while monitoring electrical parameters. The primary focus of this work was to study the durability of the concrete slabs. The secondary focus of the study was to determine how well the technology works under a variety of realistic loadings.

Both slabs with the embedded IPTS were subjected to high cycle fatigue loading and then underwent monotonic loading to failure in order to confirm material properties.

During the fatigue testing both slabs experienced minor cracking; however, it was not until the upper limits of static testing that major failures occurred. Throughout the experiment, the embedded IPTS proved to be resilient and suffered little degradation in performance. The IPTS embedded in these concrete pads demonstrated reasonable durability with promise as a viable solution to the growing needs of the EV infrastructure.

1. INTRODUCTION

1.1 Problem Statement

With concerns of using alternative energy, electric vehicles (EV) is considered in transportation for the roadway. Currently, there are several issues preventing the wide range use of EVs today. These problems include time to charge, availability of dedicated charging infrastructure, and battery life. Though many advances are being made, in-motion electric wireless power transfer provides a solution by allowing EVs to charge while in transit. By charging vehicles wirelessly, it would be possible to extend battery life and therefore make EVs more efficient and user friendly. With an inductive power transfer (IPTS) in major roadways, it would be possible to increase the viability of environmentally friendly vehicle choices. Creating such an intricate system is a multidisciplinary effort and has focused mainly on the development of efficient wireless power transfer. Continuing previous experiments and verifying fatigue life over time is just a small part of current research.

This paper mainly seeks to test durability of embedded IPTs in concrete panels with a hydraulic actuator and repeated cyclic loadings simulating from truck tire load. Further testing following three-point bending standards will then determine the failure point of the embedded electronics. The information found will verify current designs and direct their future. It is important to note that the purpose of this research is to verify the functionality of an embedded IPTS. Though strain data will help clarify the functionality of the system, this paper is not repeating research on elastic foundations, nor is it an attempt to replicate experiments on advanced beam mechanics.

1.2 Objective

The purpose of this experiment is to investigate durability of the IPTS in roadway concrete. To continue the development of this technology, this research will need to prove that the embedded systems will withstand the rigors of highway travel as a minimum level of success along with the testing of specimens in laboratory. To accomplish this, the final state of the system, electrically and structurally, will be taken into consideration. In addition, strain data from various surface points will be taken to help define the system response to various traffic loadings. This type of analysis will determine appropriate concrete mixes, reinforcement types, and coil configuration to improve upon designs quantitatively.

1.3 Concurrent Research

Throughout this paper, there are several references to projects or results not directly handled by this paper. Thermal responses by Arden Barnes, modeling and concrete design by Pilaiwan Vaikasi, and electrical performance analysis by Benny Varghese are all critical components to the overall success of this technology. However, it is not the purview of this paper to address or explain the experiments researchers have completed. This paper will only reference the materials they have provided, and further inquiries should be made to the individual researchers for specifics.

1.4 Outline

Chapter 2 contains a review of relevant literature and a history of IPTS in concrete. It also includes information on a Wöhler Curve and data processing and their applications. After a review of the literature, Chapter 3 will detail the experimental program and setup. Chapter 4 will detail the technology used in the experiment and will describe the data analysis method.

Chapter 5 shows the experiment results of the fatigue testing and final beam failure. Chapter 6 is a summary of the experiment and provides recommendations based on the findings of this research.

2. LITERATURE REVIEW

2.1 Historical Background

2.1.1 Inductive Power Transfer

(Covic & Boys, 2013)

This article reviews the important developments in wireless power transfer systems over the last two decades. As the technology vastly varies, Covic focuses solely on the inductive power systems and their applications. Original uses of wireless power transfer were mostly industrial where the distance and alignment of the system was more easily controlled. Embedding an IPTS into concrete introduces further inductance, requiring more power, while having to maintain similar power transfer efficiency as earlier iterations. The authors continue to define the necessary equipment for an IPT system and the challenges of optimization and their implementation into roadways.

Work on wireless power transfer originally started with the development to transfer energy large distances, but with the energy inefficiencies, radio systems were eventually developed. Nikola Tesla's induction motor showed that the change of mechanical force to electrical power was possible, with the downside of having the coupled components a short distance apart. Tesla's technology was used in efforts to power locomotives, but difficulties associated with the technology resulted in perpetuating myths that wireless power transfer could not be done.

A century after Tesla, various projects and research have improved upon the ability to transfer power wirelessly, but it was not until Boys and Green (1991) that a system was developed to define improvable components. One such issue that Covic addresses is the inherent coupling in previous attempts. Inductive coupling is when two conductors are configured such that a change in current in one induces voltage through induction in the other. By decoupling conductors and allowing the receiving end to accept frequency variation, it allows multiple independent uses from a single track without a loss in power transfer. This principle is a requirement for dynamic charging to be successful.

Covic then lists the necessary components of a successful IPTS, which are as follows:

1. A utility to VLF (very low frequency 3.0 – 30 kHz) or LF (low frequency 30.300 kHz) power supply for energizing track
2. The track itself with its frequency compensation and magnetics construction methodology
3. A pickup system for taking power magnetically from the track
4. A controller for controlling the power transfer process to a DC output voltage

Covic then goes into the nuances of selecting an inductor shape, as circular pads allow easy power transfer but do not have a smooth power profile. Rectangular pads would allow more space in between, thereby making each pad more cost effective, rivaling even standard vehicles. Future development involves the direct embedment of ferrite and the required components into concrete. The electrical equipment needs to withstand the dangerous environment for most of the service life of the concrete for the technology to be successful.

2.1.2 Electrification of Roads: Opportunities and Challenges

(Chen & Kringos, 2015)

This article is a summary of various technologies with electrifying roadways. Regarding the IPTS, Chen & Kringos wrote that the embedded technology would need to endure a variety of stresses to be considered for use. Those stresses include repeated traffic loading, climate induced thermal contraction, and the possible moisture flow due to freezing and frost. The electrical components would also need to endure the mechanical fatigue exerted on the road. Chen & Kringos note that structural failure caused by the de-bonding of the IPTS is a major concern.

Another challenge that should be considered is the requirement for the IPTS roadway to have stricter surfacing requirements than normal pavement. Due to the integrated nature of the IPTS, regular maintenance becomes much more difficult, as pavement replacement becomes much more expensive. Regular maintenance will be critical for the long-term success of an electronic road (eRoad).

Chen & Kringos wrote the following about the benefits of directly embedding the ITPS in roadway concrete:

1. The protection of the IPT facilities against accidental traffic and environmental loading damage, and also against water ingress corrosion
2. An overlay that may act a stress relief layer to improve the structural integration and benefit the eRoad's long-term performance
3. Enhanced cost effectiveness as maintenance and rehabilitation actions will be confined to only the overlay
4. Avoiding safety issues related to the voltages present in the IPT system

However, the IPTS is not without its disadvantages as there are a variety of engineering challenges associated with wide-scale use. Direct embedment inherently increases the distance from the charging coils to the receiving pad, which correlates to a decrease in the efficiency of power transfer. Further challenges are listed below.

1. There is an increased need for higher surface quality.
2. The risks for cracking and de-bonding failures around the discontinuous interface are relatively high and will accelerate the structural deterioration.
3. Current lack of consideration regarding the practical road infrastructure, cost-effective construction, and maintenance will be key challenges.

Chen & Kringos finish by commenting that the environmental impact of the system will be critical. To reduce the overall use of traditional vehicles would signify that the electronic alternative was as effective or more so. Monitoring and maintenance systems would also have to be integrated and must be considered in the development of the system. It was noted that the ITPS has been shown to actively diminish battery limitations in EVs. This article identified key issues related to the implementation of an IPTS, and which considerations should be taken for future iterations of the technology.

2.1.3 Wireless Power Transfer Roadway Integration

(Gardner, 2017)

Gardner's research focuses mainly on the engineering challenges associated with the embedment of an ITPS into electric roadways; specifically, the electrical performance and structural implications under typical stresses experienced by roadways. The research also includes a review of Covic (2013) as the IPTS used in Gardner's research follows the recommendations suggested by the findings of the article.

The research covers the testing of various materials and embedding techniques with the intent to determine the effects on the electrical capabilities under stress. The inductance and resistance of the electrical wires were tested in three types of concrete as the concrete approached failure. Results of the concrete testing showed no observable change in the electrical ability.

Further testing on individual components was performed, confirming that aluminum plating under the coil did not adversely affect the electrical performance and in fact added to the structural integrity of the slabs slightly. Holes were drilled into the plate to increase concrete workability during the pouring process.

Additional testing was performed on the insulation of the Litz wiring used in the IPTS. Without a lining, it was found that a Litz wire in direct contact with the concrete had a resistive element 18 times higher than a control wire. To combat the increase in resistance, several coatings were tested as insulation for the Litz wire. Nylon coating, plastic jackets, and rubber coatings were tested, and data of the electrical process was recorded over the 28-day concrete curing process. A resulting trend showed that in each case inductance dropped in the system and then slowly regained the original value as the concrete cured. Isolating the wire in a rubber coating did not have a similar drop in inductance, though it was difficult to maintain a constant thickness with spray coating.

Gardner's final tests involved fatigue testing scaled models. The scale model also used scaled AASHTO loadings. Gardner noted a possibility that discontinuities created by the embedded technologies could be the source of early cracking found in his tests. The paper concludes by stating that the electrical properties of the system did not diminish significantly over the testing period.

2.2 Durability

2.2.1 GFRP (ACI 440.1R-15)

There are a variety of papers with research regarding fiber reinforced polymers (FRP), but the American Concrete Institute (ACI) is the design standard. FRP reinforcement use can be traced to the end of World War II and the expanding use of composites. Commercial uses included golf clubs and fishing rods, but it was not until the expansion and subsequent maintenance requirements of the national highway system that FRP was considered for concrete reinforcement. With deicing salts becoming more popular, a need for a material that could resist corrosion became apparent, though it was not until the 1990s that they were used as a primary reinforcement in areas with heavy corrosion. With the advent of Magnetic Resonance Imaging, (MRI), FRP use also became standard in construction where magnetically inert materials were required.

Recent uses of FRP, such as the Emma Park Bridge in Utah constructed in 2009, have accelerated bridge construction with the application in precast concrete deck panels. Glass fiber reinforced polymer (GFRP) replaced epoxy reinforcement in a sea wall in Maui, Hawaii, in 2012. In 2013, the I-635 bridge decks in

Kansas City, Kansas, were replaced with GFRP mat replacements, showing that GFRP is capable of handling larger and higher traffic bridges.

Though GFRP is applicable in many situations, consideration should be taken before selecting FRP as a reinforcement material due to the stark changes between it and steel reinforcement. ACI provides a list, found below, of several criteria that should be considered before its use.

Why should FRP bars be considered?

A. Impervious to chloride ion and chemical attack
B. Tensile strength is greater than steel
C. Light weight – one-fourth to one-fifth the weight of steel reinforcing bar
D. Transparent to magnetic fields, radio frequencies (glass FRP only)
E. Thermally and electrically non-conductive (glass FRP only)
F. Less concrete cover is possible
G. Admixtures to reduce corrosion are not needed
H. High fatigue endurance
I. Easily "consumed" by excavation equipment when used in temporary structures
J. In corrosive environments, service life is much greater than that of steel
K. Has a better damage tolerance in the field than epoxy coated steel and no touch-ups are required post installation.

Differences between FRP and steel:

A. FRP is linearly elastic until failure, whereas steel will yield at the same point
B. FRP is anisotropic, whereas steel is isotropic
C. Due to a lower modulus of FRP bars, design for serviceability often controls
D. FRP bars have a lower creep-rupture threshold than steel
E. The coefficient of thermal expansion is different in the longitudinal and radial directions
F. Endurance time elevated temperature conditions are less than that of steel
G. Should degradation of FRP bars occur, the degradation mechanism is benign to the surrounding concrete; this is unlike steel, which expands and causes failure of the member.

Where should FRP bars be considered?

A. Any concrete member susceptible to corrosion by chloride ions or chemicals
B. Any concrete member requiring non-ferrous reinforcement due to electromagnetic considerations
C. As a cost-effective alternative to epoxy-coated and galvanized reinforcement
D. Where machinery will "consume" the reinforced member, such as tunneling and mining applications
E. Applications requiring thermal non-conductivity
F. In mass concrete exposed to marine chlorides near chloride exposure in hybrid applications with steel

FRP, when loaded in tension, does not exhibit any plastic behavior before failing. Depending on the type and manufacturing method, FRP can have greater tensile strength than equivalent rebar. In terms of compressive strength, FRP has been measured to show as low as 20% of the tensile strength. Similarly, most FRP composites do not perform well in shear.

Previous fatigue testing with GFRP dowel bars show fatigue behavior like that of steel for cyclic transfer shear loading up to 10 million cycles. The testing shows that an equivalent performance can be achieved by changing the diameter of the FRP bar or the spacing. It is further shown that fatigue stress ranges for

FRP are dependent on the manufacturing process, environmental conditions, and type of fatigue load applied. In various projects it can be shown that the heat transfer of FRP bars in concrete is similar to that of slabs reinforced with steel reinforcement.

All the aforementioned considerations are directly applicable to the use of FRP in an IPTS. Inert to inductance, similar fatigue response to steel and resistance to corrosion for use in varied locations makes FRP, and GFRP specifically, ideal for reinforcement in an embedded IPT system.

2.3 Surface Cracking in Pavements

2.3.1 Analysis of Periodic Cracks in Surface Layer of Pavement Structures

(Xu et al., 2010)

This article covers pavement cracking in the surface layer of roadway concrete. Water penetration can reduce the effectiveness of the subbase and is the main cause of surface cracking. As such, cracking has a direct correlation to the quality and service life of pavements. Xu observes that the primary cracking is in the bending zone of the pavement, and cracks quickly propagate parallel to the original crack.

Xu notes that although significant research has been dedicated to the crack patterns and the analysis of single cracks in pavements, little has been done to investigate periodic surface cracking. Understanding and correct modeling of cracking would allow further insight into the fatigue life of the pavement. Xu focuses his research on the evolving process of periodic crack arrays.

A four-point bending test was developed to show the process of periodic cracks through a variety of layers. It was found that the appearance of cracking was predictable and entirely dependent on crack spacing. Researchers also found that horizontal stress is at a maximum between two existing cracks. After a certain spacing is achieved, no more cracks will form, and each crack opens with the increasing external load.

Testing a slab composed of multiple layers was then performed to determine what effect the various layers had on crack spacing. It was found that the base layer thickness had little effect on the overall spacing, but that minor surface thickness changes have a large effect on the crack spacing. Xu concludes that crack spacing had a linear correlation with the thickness of the surface layer.

2.4 Flexural Response

2.4.1 Fatigue Analysis of Plain Concrete in Flexure

(Hwan, 1986)

With a variety of structures subjected to fatigue loadings, it is becoming increasingly more important to determine the behavior of concrete under those loadings. Most concrete structures design concrete to crush or crack before the reinforcement materials. This design philosophy has made the understanding of concrete fatigue behavior trail behind the understanding of other materials under similar loading.

Hwan uses an S-N curve or Wöhler curve to interrelate applied fatigue curves and the fatigue life of concrete. Using the S-N curve, it is possible to estimate the mean fatigue life of concrete given a constant amplitude cyclic stress. The article's purpose is to investigate the fatigue strength of plain concrete subjected to flexural loading and implement probabilistic analysis to protect against fatigue failure.

S-N curves are found empirically and use several samples to determine the exact extent of the curve, and they are more commonly used in metals. For concrete, the S-N curve uses the applied maximum stress divided by the modulus of rupture for the specimen to determine design points. Comparing the maximum stress to the number of cycles until failure allows an optimization in design to determine the stresses needed to withstand larger cycling. Hwan concludes with various mathematical proofs of the probabilistic uses of the S-N curve, which are not necessary for the application in this paper.

2.4.2 Fatigue Resistance of Concrete Pavements

(Roesler, 2006)

This paper focuses on accelerated pavement testing of full-scale concrete pavement sections. Such tests allowed for the verification of Miner's Hypothesis in order to explain specific contributions to concrete fatigue failure. Roesler notes that concrete slab strength is much greater than that of a beam, with several factors related to loading and slab geometry. It was also found that the flexural capacities of slabs were 1.3 to 3.5 times higher than comparable beams. Testing results show that a fatigue model incorporating stress range and a stress ratio is superior to predicting fatigue life.

Most research is conducted on small-scale specimens or the monitoring of in-field sections. The research into small-scale beams and cylinders has been extensive, whereas research into full-scale slabs has been limited to the U.S. Army Corps of Engineers in the 1940s, 50s, and 70s. The Army Corps' experiments were the data source of research for the following 30 years. It was found that concrete fatigue equations are mainly dependent on four main factors. The four variables are as follows:

1. Specimen size and geometry, loading configuration, and boundary conditions (generally called the size effect)
2. Theoretical model for stress calculation (plate theory or layered elastic analysis)
3. Bending stresses included (temperature and moisture curling and mechanical loading)
4. Method of counting stress repetitions

This article also discusses testing done to explore the effects of stress range and load pulse type. Using a soil containment box and a slab constrained to achieve an infinite pavement, researchers used stress ratios to determine their effect on fatigue life. A photo of their setup is shown in Figure 2.1.

Figure 2.1 Roesler Test Setup

Roesler used the findings to determine a fatigue life equation shown below. Through the development of the equation, it was confirmed that beam fatigue curves underrepresented the resulting S-N fatigue curve. The cause of the curve can be attributed to the estimation of beam strength.

$$N_f = \left[\frac{2.689}{\left(\frac{\sigma}{MOR_{beam}}\right)}\right]^{21.79} \tag{2.1}$$

In high-cycle fatigue testing, peak stress and stress range were found to be more impactful to the overall number of cycles to failure. Roesler concludes by suggesting that the use of an S-N curve can be supplemented with fracture mechanics.

2.4.3 Application Hints for Savitzky-Golay Digital Smoothing Filters

(Bromba et al., 1981)

The article features the use and boundaries of using a Savitsky-Golay filter (S-G filter). This paper focuses on the use of a digital filter to smooth and process low level noise out of a signal. Instead of least square linear fit, this type of filtering is polynomial in nature. Several equations are listed in the use and application of the data filtering.

Bromba recommends using an S-G filter when peak deformation would cause significant error. For S-G smoothing filters the noise reduction reduces to the inverse square root of all coefficients. The effect of smoothing has been demonstrated to smooth up to ±2σ. In spectrometry, which is the paper's original use for S-G filters, the use of Gaussian or Lorentzian line filters are also considered. There are several requirements to use this type of filtering and include that the sum of all coefficients is one and all higher moments following a data filtering model are also zero.

S-G filtering truncates some amount of the frame lens data, and to avoid the loss of data at the beginning and the end of the record it is suggested to have a combination of least squares fitting and least squares smoothing. Bromba ends by saying that the application of an S-G filter when applied to “straightening through smoothing” is an advantageous use of the system.

2.4.4 Savitzky Golay Smoothing Filters

(Press et al., 1990)

This article expands on the *Application Hints for Savitsky Golay Digital Smoothing Filters* presented in 1981. Instead of using mathematical definitions, a focus on practical calculation and demonstration of the noise reducing effects are shown. Most data filtering functions transform the Fourier data by multiplying them by a filter function. The transforming technique allows various filtering, such as high pass or low pass, to be accomplished with the least number of polynomial coefficients.

S-G filtering does not use Fourier transforms to filter noise. Instead, it can be useful to replace data points with averages within a data window. Because each point measures the same underlying value, a moving average can remove the varying noise without biasing the data significantly. Data smoothing can provide a valuable tool in data processing, but Press raised the concern of the ethical issue of using smoothed data, as the resulting data may completely change. Press suggests that S-G filters and data smoothing in general is most justified when used as a graphical tool to roughly visualize noisy data.

Using just a moving window average introduces an undesirable data bias by reducing the underlying values of the data points. The idea of an S-G filter is to find a polynomial function with coefficients that preserve peak data and effectively preserve datasets. A least-squares fit is done at every point with a moving window. Hand calculations involve a linear matrix inversion and would be very time consuming. Press indicates that fourth order polynomials are recommended as there will never be an ill-conditioned matrix.

Press uses a fourth order in the following example, with a 33-point width. As demonstrated, higher order allows further development as the width of peak decreases at the cost of decreasing smoothing on wider peaks. If used with data that do not have significant variation in peak width, S-G filtering provides phenomenal results by smoothing data while increasing resolution. If the peaks are about the width of the moving window, then these filters have no significant advantage over other filtering devices. Press finalizes by indicating concerns of irregularly spaced data points, as it would be impossible to accurately fit polynomial coefficients to the data.

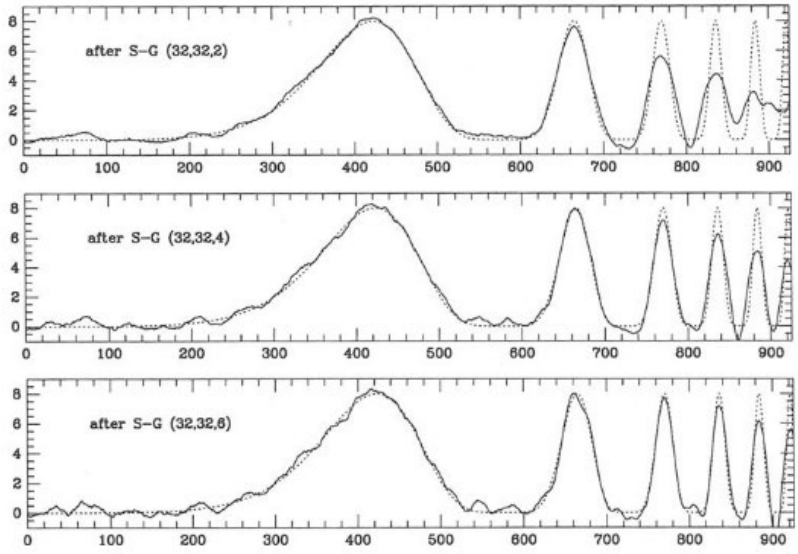

Figure 2.2 Example of an S-G Filter

3. TESTING PROCEDURE

3.1 Introduction

This chapter details the experiment that was designed and performed to determine the fatigue life of an IPTS embedded in roadway concrete. Future use of this technology is expected to have a similar lifespan to the current roadway designs, which experience both environmental and traffic loadings. The Litz wire, a multi-strand cable used to cause magnetic inductance, is near the cover requirement for concrete. It is important that the ITPS does not experience additional stress that can negatively affect the electronics' lifespan while embedded in concrete. Effective design of the ITPS, which includes efficient power transfer and resilient design, will allow future infrastructure to aid the usability of EVs.

In typical roadways, repeated tension loading from traffic is the main cause of cracking and roadway failure (Xu et al., 2010). Finding the stress at the midspan is a way that allows the quantification of the structural integrity of the system. This chapter discusses a simplified approach to simulate the loading from both traffic and environmental effects. These simplified loadings can then be used to determine the properties of an embedded IPTS.

Two slabs will be tested, one with steel reinforcement and the other with glass fiber reinforced polymer (GFRP) reinforcement. They will undergo the same loading to compare both types of reinforcement, and then both slabs will be put in a three-point bending test to verify the electric performance of the embedded electronics.

3.2 Slab Specifications

Two slabs were used to prove the long-term use of inductive tower transfer over the course of this experiment. Specimen 1 had steel reinforcement and specimen 2 had GFRP reinforcement. They were poured on the same day from the same mix and experienced the same number of environmental factors, fatigue cycling, and various component testing. Each slab is 8 ft. x 4 ft. x 1 ft. with the same reinforcement schedule. A cross section of the slabs is shown in Figure 3.1. The Ferrite and Litz wire being above the reinforcement is a concern for the overall durability of both pieces, but electric design requires the two inducting plates to be as close as possible. The current configuration follows clear cover for the concrete slab and in theory should not debilitate the slab strength.

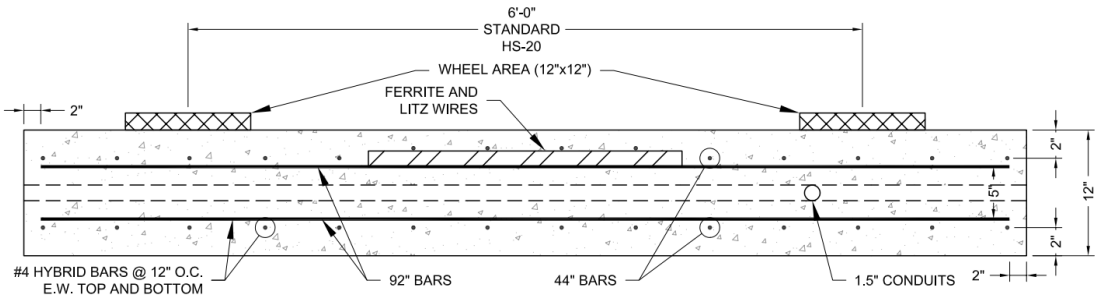

Figure 3.1 Cross-Section of System

In August 2019, three slabs were poured with an intended compressive strength of 4,500 psi. The 28-day strength only reached 3,224 psi. based on the average of three cylinders (Figure 3.2). There were no compressive cylinders available to verify the strength of concrete at time of testing, so an estimation method based on the flexural strength will be covered in depth in Appendix G.

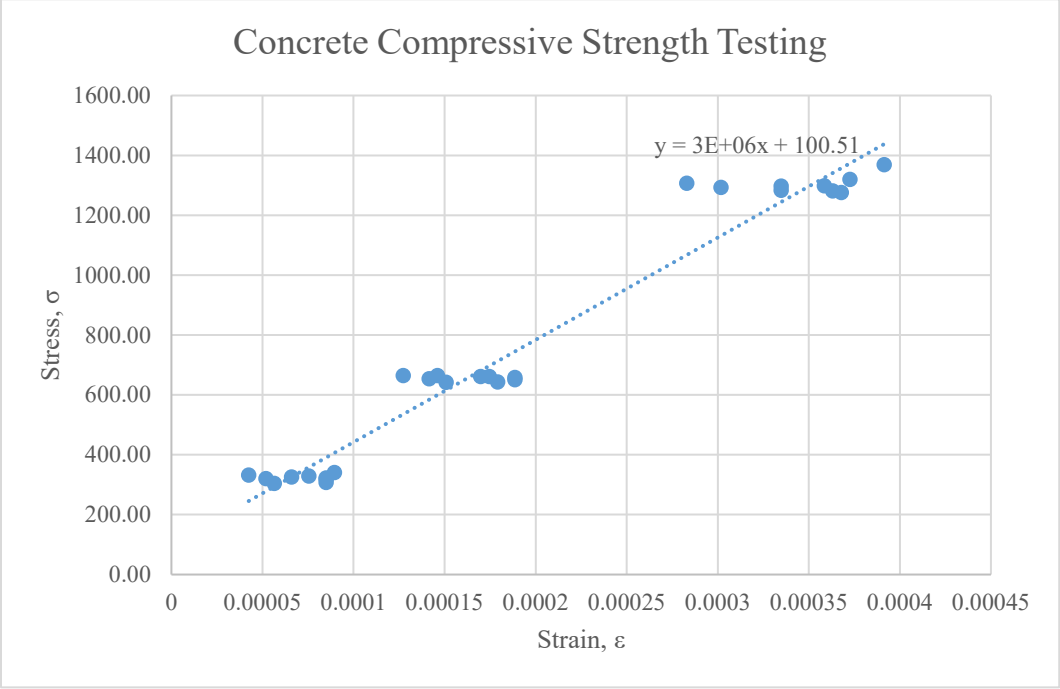

Figure 3.2 Compressive Strength Testing Results (Vaikasi, 2021)

The slabs were subjected to a variety of environmental factors until the slabs were moved to the Systems, Materials and Structural Health (SMASH) laboratory for fatigue testing in May 2020. Figure 3.3 shows part of the moving process. In the several months before the move, concurrent research such as Barnes (2020), Vaikasi (2021), and Varghese (2021) used the time to test various components of the system. Arden's experiments focused on the heat dissipation in a full powered slab, as residual heat would pose serious issues for the electrical components and structural integrity of the slabs. Varghese focused on the electrical design and testing, while Vaikasi's research focused on the internal mechanics of the slabs.

Figure 3.3 Moving the Slabs

3.3 Testing Equipment

To artificially age the concrete, the experiment used a 110-kip MTS 244.41 DuraGlide Hydraulic Actuator. This ram was mounted at the USU SMASH laboratory on a strong frame capable of handling 1200 kips in shear. The slabs were supported by a gravel bed situated on a 3/4-inch oriented strand board (OSB). This change from standard simple beam configurations found in bridge decks was intentionally done to create an infinitely supported slab, allowing a more realistic response from the fatigue cycling. Data were recorded on a Campbell Scientific CR3000, with BDI ST350 strain gauges; specifics of the data acquisition and the Campbell Scientific will be discussed in a later chapter.

Figure 3.4 Gravel Containment Box

The MTS ram runs proprietary software, and two sets of testing protocols were created using the software. The fatigue loading starts at 0 pounds and then ramps to 10% of the maximum loading within 20 seconds. The force then cycles between the minimum and maximum for the determined number of cycles while recording the displacement and force of the ramp; an example of the fatigue program is shown below. Fail-safes were implemented to prevent damage to the equipment.

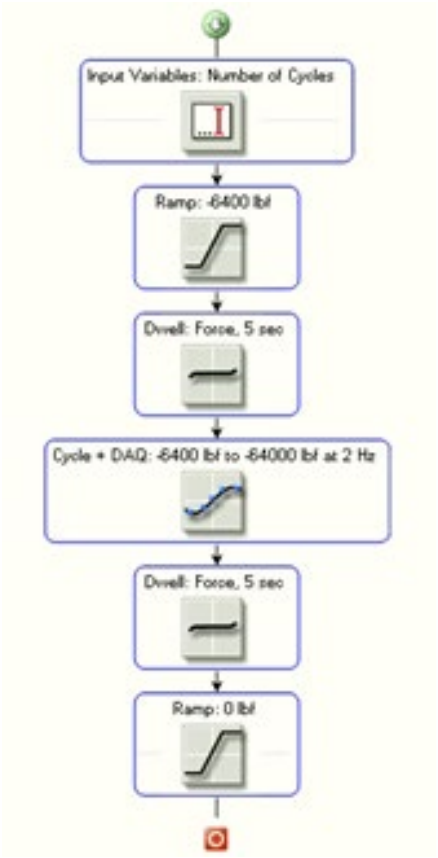

Figure 3.5 Diagram of the Fatigue Program Used

The static testing program is more simplified, consisting only of a ramping force induced by a constant displacement. Data such as force and displacement are recorded, which can then be taken and analyzed. For this experiment the maximum force experienced by the slab can be used to determine material qualities of both slabs.

3.4 Procedure

To properly simulate traffic conditions, this experiment used AASHTO's HS-20 design load, shown below. The 32,000-lb. axle loading is the basis of the forces exerted on the slab and to simulate the passage of vehicles, cyclic loading was used. An approximation of traffic loading was required so a 2 Hz sinusoidal cyclic wave was selected.

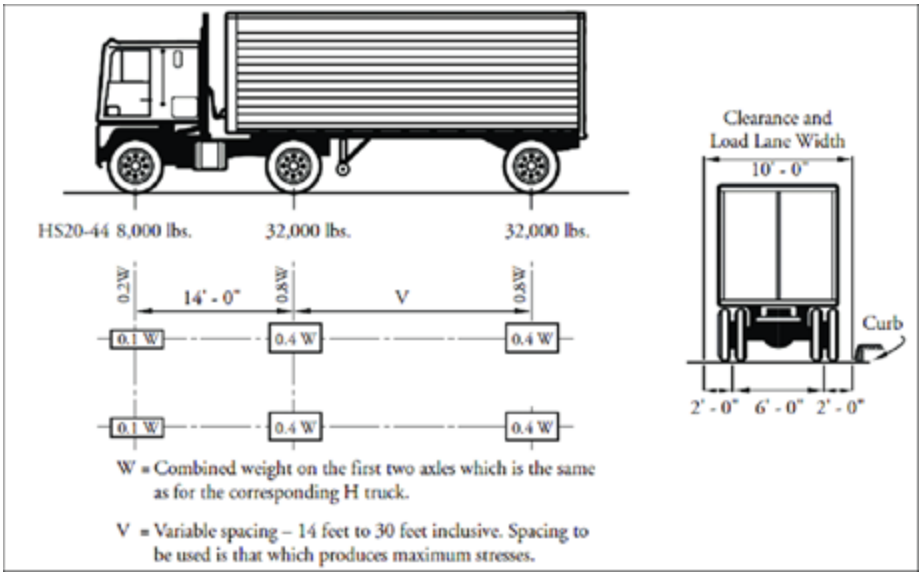

Figure 3.6 Standard AASHTO HS-20 Design Loads

To determine the number of cycles to run for the experiment, Kumar et al. (1998) found that 2,000,000 cycles can be conservatively used as 80% of the fatigue life of a bridge deck. He also found that the majority of cracking occurs within the first 500,000 cycles. The experiment split the cycling into three phases, the first phase used 300,000 at 32,000 lbs. or 32 kip. Some states allow the overloading of their highways, sometimes up to 58 kips, as such the second phase of the experiment was chosen to cycle 100,000 times at 50 kip. The third and final phase consisted of 64,000 pounds for the remainder of the number of cycles.

Though it is expected that the slabs would crack under normal loading before the full 500,000 cycles have completed (Kumar 1998), increasing the force is multipurpose. First, it tests the structural configuration of the slab; second, this is the first time a full-scale embedded ITPS was tested structurally. Testing the system at probable loadings allows a verification of the peripherals of the ITPS and is critical for further improvements. Photos of the finalized setup are shown below.

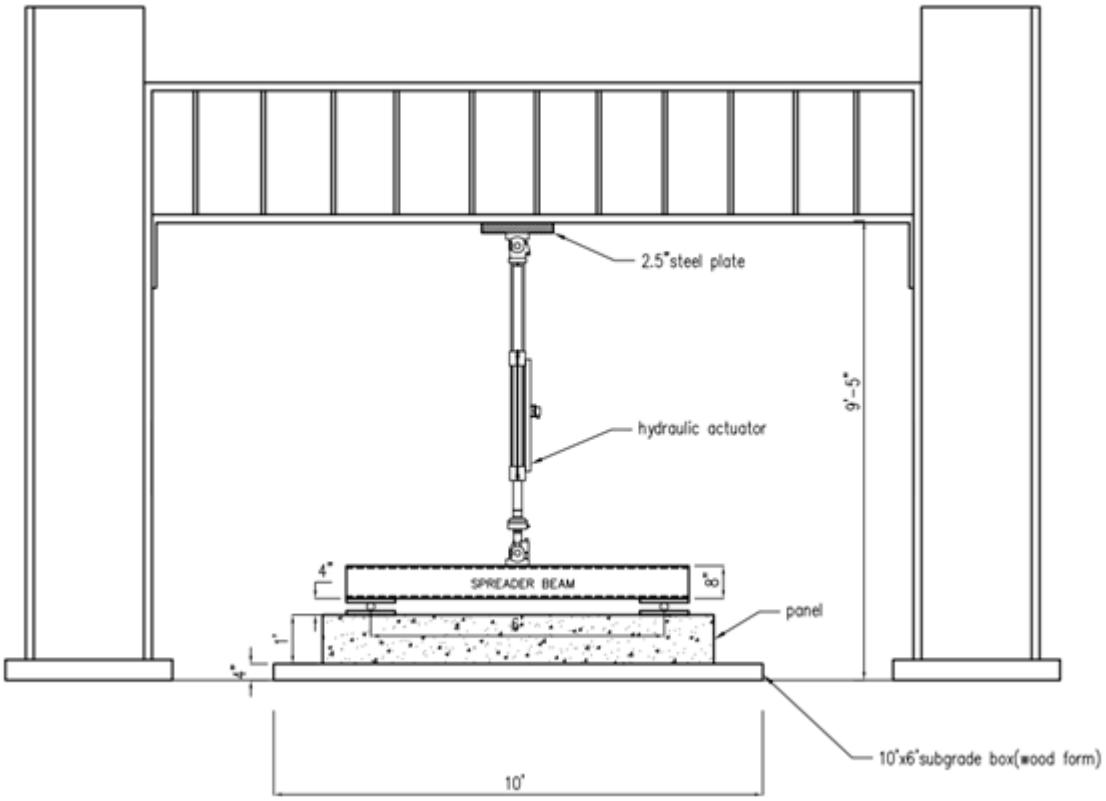

Figure 3.7 Drawing of the Fatigue Setup

Figure 3.8 Finalized Testing Setup

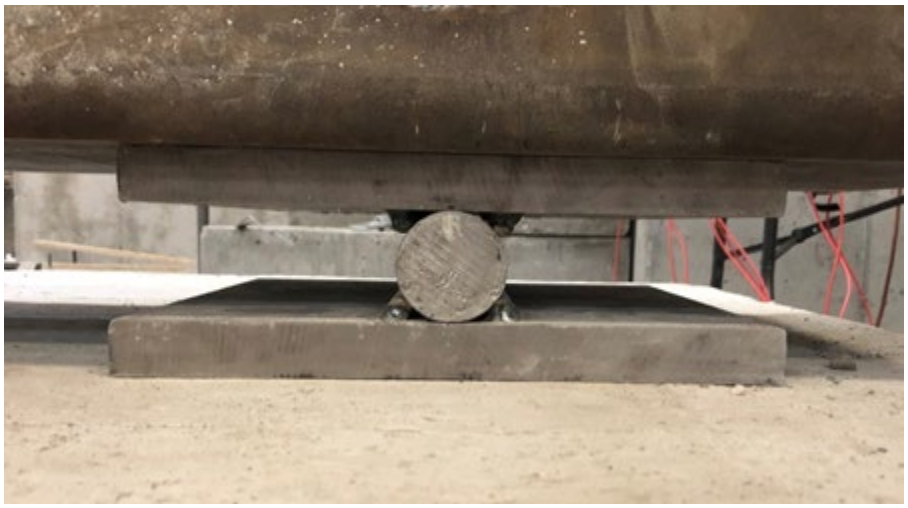

Figure 3.9 Pinned Connection

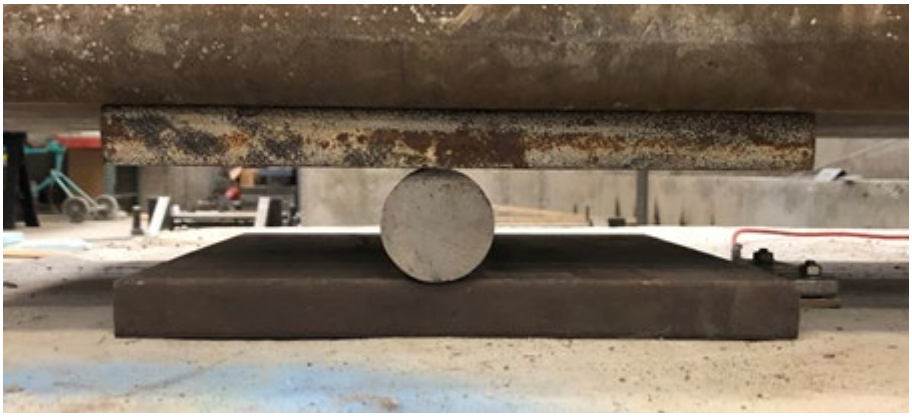

Figure 3.10 Roller Connection

Both slabs then went through static failure with the setup as shown below. To maintain tension on the same face of the slab throughout both portions of the experiment, the slabs were inverted. Additionally, during the three-point bending test, the electrical system was supplied with power and monitored to determine the quality factor throughout the breaking process. The quality factor is a measurement that relates a measurement of reactance versus the resistance, which in this case indicates the ability of the IPTS to transmit power efficiently. This determines the overall resiliency of the system in a worst-case scenario. A full explanation of this experiment's quality factor can be found in Varghese (2021).

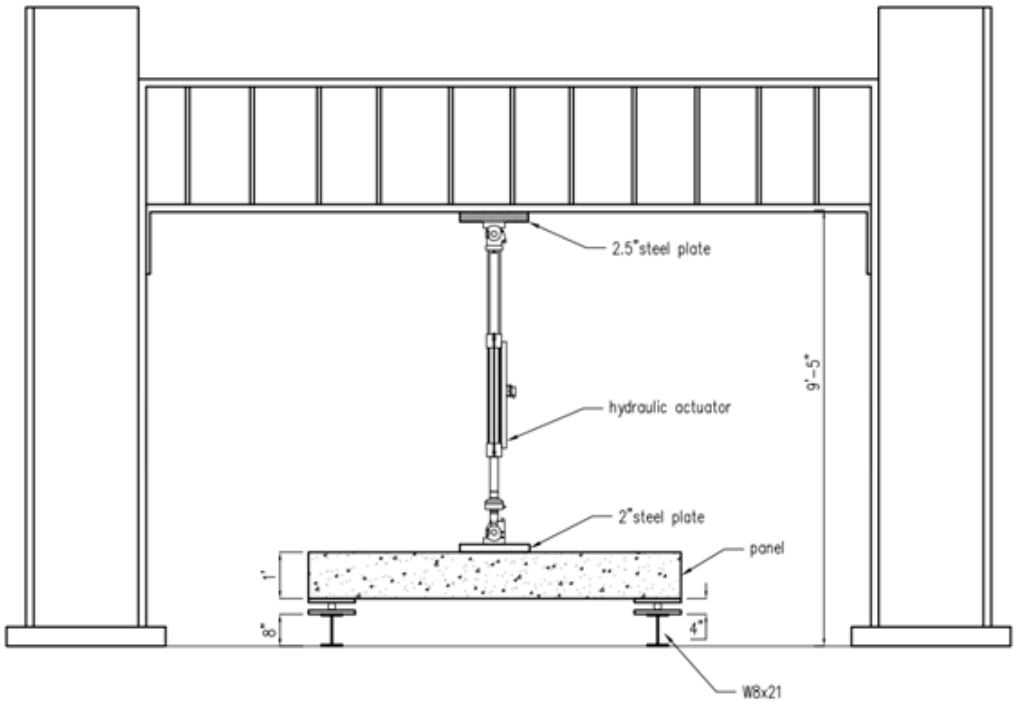

Figure 3.11 Drawing of the 3-Point Test

Figure 3.12 Static Test Setup

To complete the three-point bending test, information from ACI (2009) and ASTM (2017) recommends a displacement controlled test. The recommended rate of .10 in./min. was selected. Converting to units, the MTS will use the finalized rate of .00167 in./s. The W8 x 21 support beams that were used to achieve a simple beam connection were calculated to have a maximum capacity of 75,000 lbs. before buckling (AISC 2005), so protocols were set in place to stop the MTS and test if the force approached the limit.

3.5 Cracking Mechanism in Roadway Concrete

Concrete fatigue is the process in which concrete ruptures through repeated loadings. Each loading exceeds the material strength. Concrete cracking is generally classified by the number of cycles done in the test, mainly low-cycle fatigue and high-cycle fatigue. The process starts with crack initiation followed by crack propagation, and finally rupture. Various conditions influence crack imperfections.

Xu et al., (2010) indicate that the cracking is most likely to occur at the location of the maximum moment. During the three-point bending test, where the slab is inverted to maintain tension, it is expected that the middle of the slab will crack first. After midspan failure, it is possible cracking will occur at third points, parallel to the original cracking. The information gained from the static failure of the experiment allows a calculation of the modulus of rupture (MOR) of both concrete slabs.

3.6 Fatigue Analysis

Concrete beams have a known method of analysis; however, the reality is that the analysis of a beam has several idealizations. Roesler (2006), previously summarized, states that:

> "Large-scale slab fatigue testing in the laboratory has demonstrated that the fatigue life of concrete slabs is much greater than the beam fatigue and the increase in fatigue life is dependent on the slab geometry, thickness, loading configuration, concrete material, and boundary conditions."

The increased capacity can be up to "1.3 to 3.5 times higher" than comparable flexural beam specimens. In 1998, Roesler confirmed the differences in monotonic load fatigue testing on slabs designed for airway use. It was found that a single slab curve could not accurately predict the fatigue life of pavements without knowing the slab strength, something that is specimen dependent. Without multiple slabs, it is improbable to estimate the fatigue life with any accuracy.

Hwan (1986) investigated the fatigue strength of concrete subjected to flexural loading and used the data to generate S-N curves. The S-N curve, or Wöhler curve, is a way to quantify the stress response in comparison to the flexural strength of concrete. In 2003, Roesler used this method to compare various laboratory results. The S-N curve was used by this experiment's predecessor, Gardner (2017), and so it is imperative that the method is used to compare past results to current and future results. Chapter 5 discusses the implementation and presents a comparison between slabs and the previous experiment.

4. DATA ANALYSIS METHODS

4.1 Introduction

This chapter discusses the data analysis methodology used in this experiment. It also covers the various equipment upgrades performed throughout the testing process. Specifics of the strain gauges used in the experiment are given. Finally, the advantages and disadvantages of the data analysis methods are covered.

4.2 Campbell Scientific Upgrades

The Campbell Scientific CR3000 was used in this experiment. This data logger has the ability to have up to nine different connectors, which allowed for monitoring the IPTS in several critical locations. This experiment used eight strain gauges with three gauges available in each of the VX terminals of the CR3000. A figure of the interface is shown below; VX channel 1 and 2 had three gauges apiece and channel 3 had the remaining two. Campbell Scientific provides a detailed diagram of its device found below.

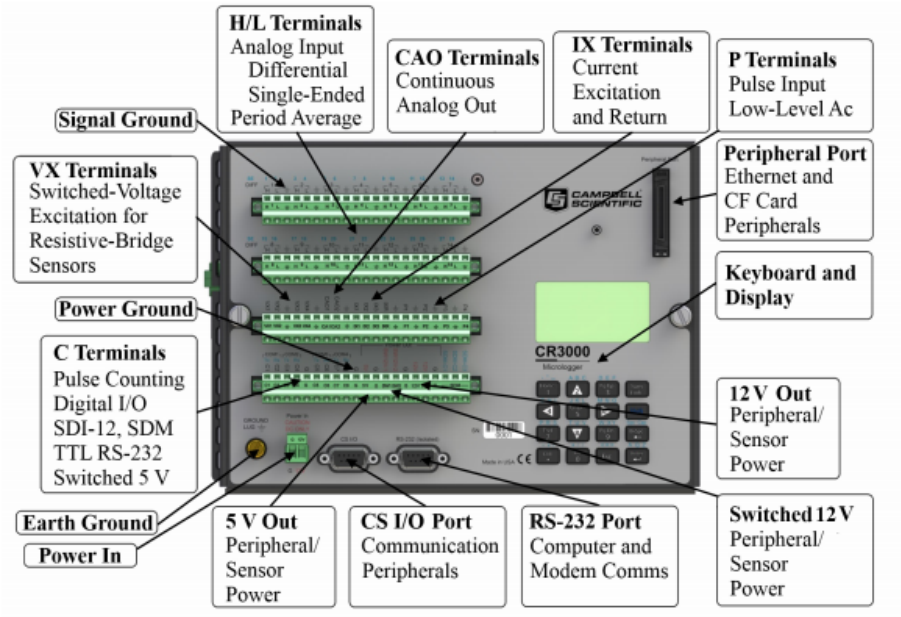

Figure 4.1 Campbell Scientific Interface (Campbell Scientific)

BDI ST350 strain gauges are full Wheatstone bridges, which allow the gauges to be connected to the CR3000 as a resistive bridge. This type of bridge circuit is best used to detect minute changes in resistance due to strain. Each circuit bridge has four strain gauges of known electrical resistance. By passing a known voltage through the excitation channel, the strain causes the resistance to fluctuate, and the Campbell Scientific reads the minute differences in the outgoing excitation voltage. A diagram of the circuit is provided by BDI in Figure 4.2.

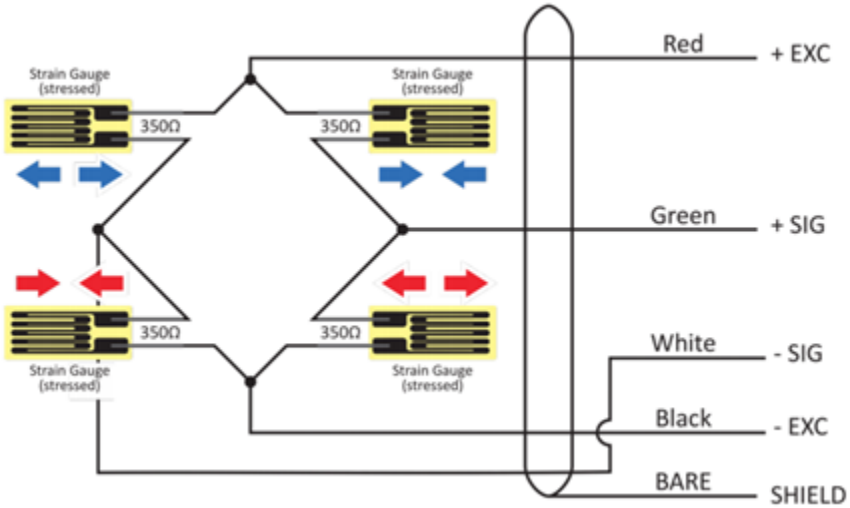

Figure 4.2 BDI ST350 Wheatstone Diagram (BDI)

Using the 5-volt excitation voltage and the resulting outgoing millivolt reading, the Campbell Scientific then applies a general gauge factor (GGF) to convert the outgoing voltage to a strain measurement. Equation 4.1 shows the units of a GGF and Equation 4.2 shows the calculation of micro strain from the Campbell Scientific voltage readings. Data processing after the experiment will handle further data needs since the Campbell Scientific is only handling the initial conversion to micro strain.

$$GGF = \#\ \mu\varepsilon / mV_{out} / V_{exc}$$

$$\mu\varepsilon = GGF \times V_{out} \tag{4.1}$$

Where:

- V_{exc} = Excitation Voltage, 5 V
- mV_{out} = Output Voltage, mV

Each gauge ends in an Intelliducer Connection designed to maintain the fidelity of the sensory under less-than-ideal conditions. To work with the data acquisition system, the gauges need to be directly wired into the system without the connector. Cutting the connectors would compromise their future integrity, so a short length of cable with a compatible connector was made so that the gauges could be removed and added as needed. The upgrade also allows for gauge maintenance and future testing. See Figure 4.3 for a photo of the new connectors. Working with the technicians at Campbell Scientific, a wiring diagram for this experiment was determined and is included with an excerpt of the code used in Appendix B. Several mechanical upgrades were also completed, allowing the new cables to be permanently wired, eliminating variability for future testing. Figures 4.4 shows the finalized wiring used in the experiment.

Figure 4.3 Manufactured Connectors

Figure 4.4 Finalized Wiring

4.3 Sensor Calibration

The Campbell Scientific measures voltage going in and out and then uses a gauge factor to convert the data to micro strain, as previously described. Over time, these gauges can lose their calibration; as such, a method was devised to calibrate and verify the sensors data. This also ensures calibration for future testing. A beam of a known shape and size was set up in a simple beam configuration and the strain gauges were fixed over the midspan. A series of weights were then placed to take readings for calibration. A photo of the system is shown below.

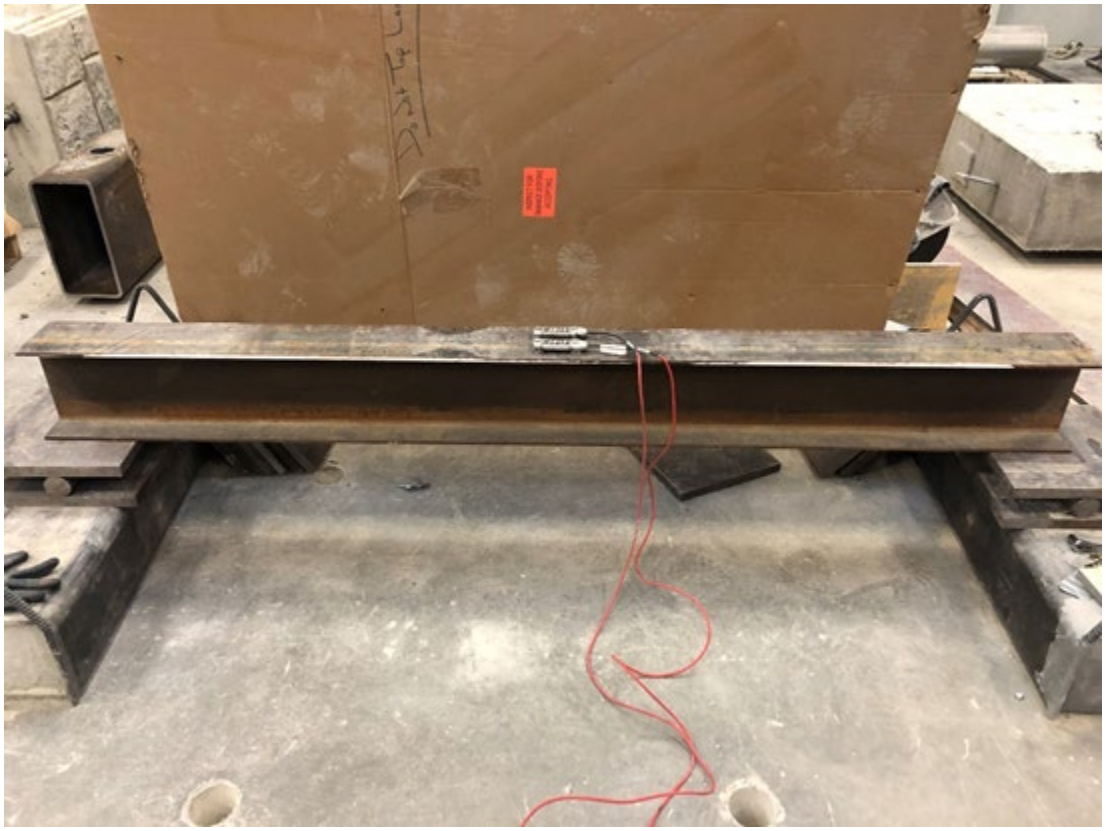

Figure 4.5 Strain Gauge Calibration Setup

The setup allows a moment to be known at the center with two equal loadings equidistant from the support. To calibrate the sensors, a gauge reading was taken at each successive loading and then graphed. Using a linear regression method, a trendline was then fitted to the graph. The trendline allows the calculation of R-squared, a value that gives an estimation of the data relationship of the expected to the found values. As R-squared approaches 1.00, the data can be directly correlated and the found value variance is minimal. Shown below is an example table and graph used in the calibration process. All strain gauge calibration data are found in Appendix F.

Table 4.1 Example Strain Gauge Calibration Table

Strain 1	1996	GGF	579.5
		Expected	Reality
Load (P)	**σ=My/I**	**με**	**CR3000**
0	0	0	552.42
80	105.179	3.627	547.56
120	157.769	5.440	544.5
200	262.948	9.067	538.89
240	315.538	10.881	535.02
	R^2	Y intercept	Offset
	0.9949	0.6264879	346.4107

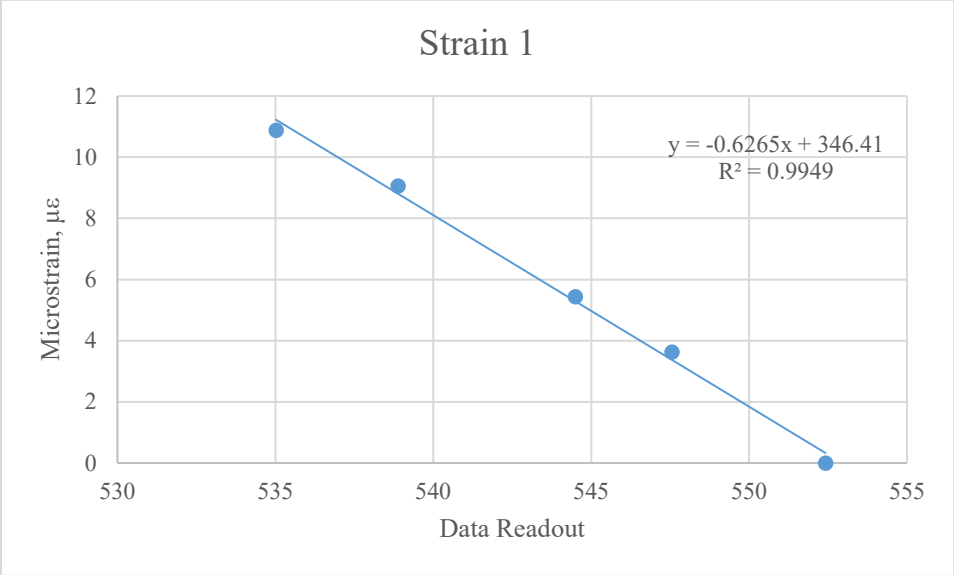

Figure 4.6 Example Trendline Fit

Each gauge was assigned a specific connector in the Campbell Scientific and then each was loaded at 80 lbs., 120 lbs., 200 lbs., and 240 lbs. Each gauge was assigned a specific channel so the code would convert the unique gauge factor and gauge variance could be eliminated. If the R-squared value was found to be less than .99, the original gauge factor was multiplied by the slope of the trendline and retested. Following this process, strain gauge #3 was the only gauge that needed further calibration.

Vaikasi's (2021) concurrent research has developed an FEA model to determine the critical areas of stress. The diagram in Figure 4.7 is an instrumentation plan that was developed for the fatiguing process. The gauges were set in locations that will give the most information on the status of the IPTS as the testing is performed. As it is critical that the gauges maintain contact, they were epoxied to the face of the concrete slab and allowed to set before testing begins.

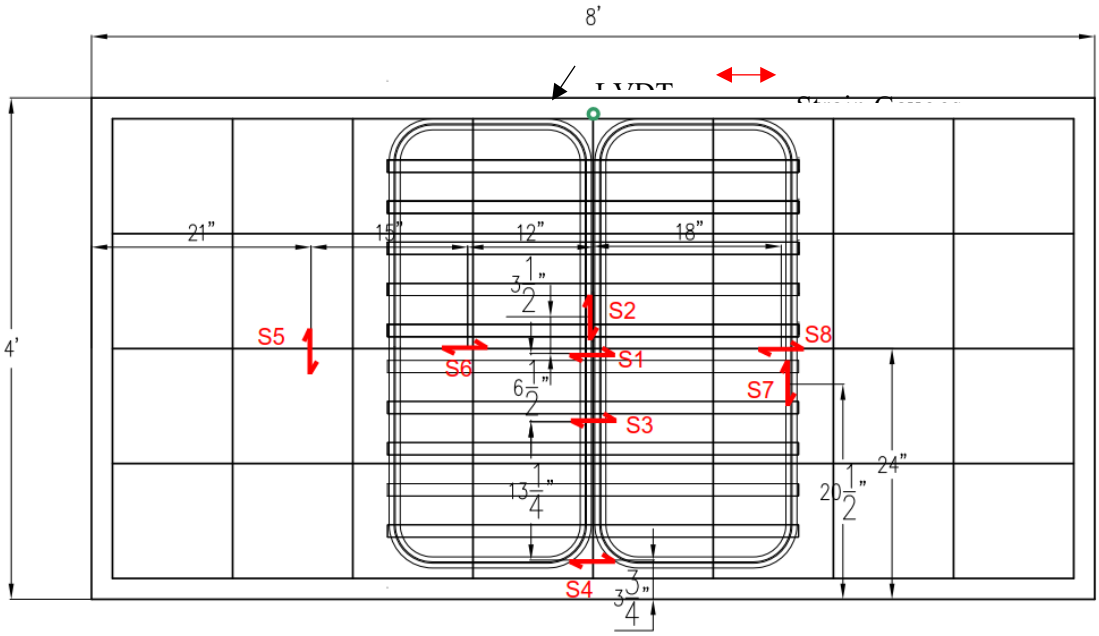

Figure 4.7 Instrumentation Plan (Vaikasi, 2021)

4.4 Data Processing

The Campbell Scientific was set to have a sampling rate of 10 Hz through the entire runtime of the experiment. A higher sampling rate was not selected for the sole purpose of memory allocation; at nearly three full days of data collection, the experiment pushed the capacity of the available memory. Noise suppression methods are possible in the Campbell Scientific but ultimately not considered to maintain the original data. As signal noise is a concern, it was decided that post processing methods would be the most effective way to sort through the large data files.

The Campbell Scientific CR3000 gets its readings of micro strain directly by reading the outgoing voltage. Because multiple gauges are in each excitation channel, the machine differentiates by sending slightly different voltage through each gauge. Because of the different starting points, an offset to centralize each gauge is necessary. Shown below is an example of the post processing offset data.

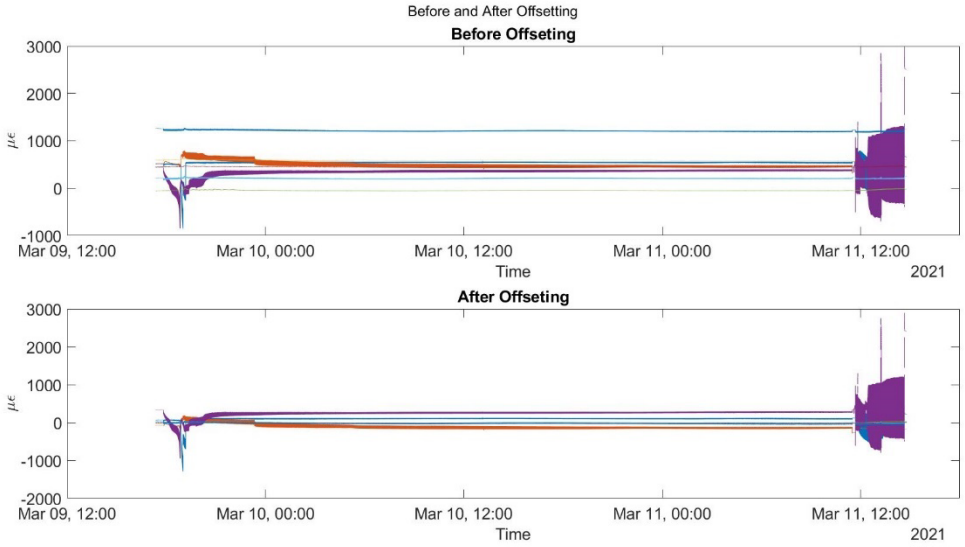

Figure 4.8 Example Offsetting

Once the data have been offset, a data smoothing filter is then used to help visualize the results. S-G filtering was chosen for its ability to smooth the data without significantly removing the extremes of the data. Though the polynomial filtering can take on a variety of forms, a fourth-order polynomial was selected (Press et al., 1990). An example of filtering is provided below. It is important to note that the smoothed graph is only used as a visual tool to better understand the strain instead of an analysis tool. (Press et al., 1990)

To fully analyze the slab, a sinusoidal function followed by a Fourier transformation to isolate the 2 Hz signal was used. This process eliminated noise by fitting a sinusoidal curve over a period of data. Though not used for long-term analysis in this research, an example is shown below.

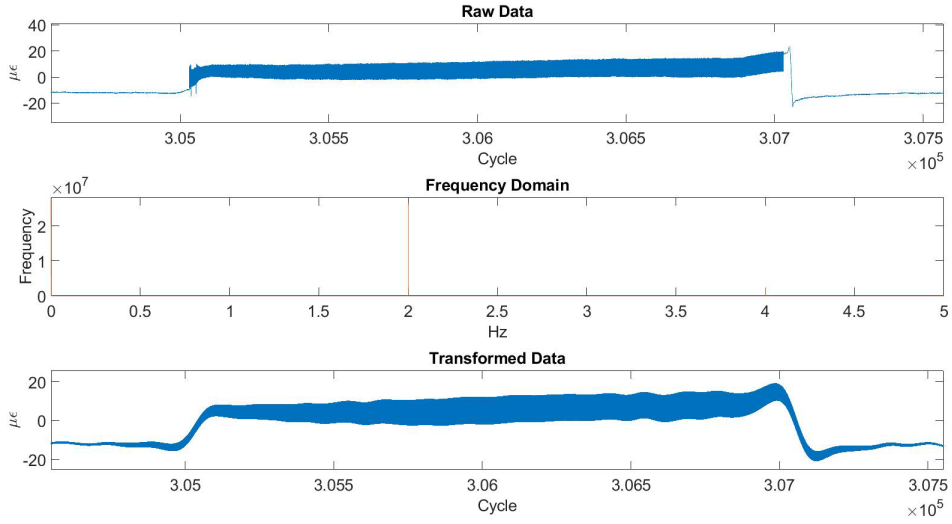

Figure 4.9 Fourier Transform on Steel Data

5. COMPARISONS AND DISCUSSION OF RESULTS

5.1 Introduction

This chapter discusses the results of the experiment performed. The data obtained were analyzed and the long-term viability of the IPTS is evaluated. Recommendations are also given for future experiments based on the results. Though not every variable can be accounted for during any experiment, this particular experiment provided actionable information for future designs. Understanding how the loading affects the behavior of the embedded IPTS allows engineers to design the next generation to better fit necessary strength requirements.

Two concrete slabs with embedded IPTSs, and different reinforcement materials were tested. The fatigue testing was designed to assess the ITPS response to long-term mechanical fatigue. The second test was designed to confirm material properties and test the serviceability of the electrical system. The data presented include the number of cycles to failure, strains at various locations, and the forces experienced by both slabs throughout both testing phases. To optimize testing times and to reduce waste, the fatigue tests were performed consecutively, followed by the three-point bending tests.

The objective of this research was to prove that the IPTS is ready for implementation in real world applications. This testing is critical to the future of the technology, as failure would delay critical progress for EVs. Success can be determined by several parameters, though the most critical success for this research is the ability of the internal electronics to work far past what the equivalent road would take. Though internal gauges are referenced, specifics of their use, calibration, and analysis should be pursued through Vaikasi's (2021) Research.

5.2 Testing Results

5.2.1 Steel Reinforced Slab (Specimen 1)

The first pad that was artificially aged has both compression and tension steel reinforcement. The first fatiguing phase, the 3-to-32.kip 2 Hz cycling, ran without any issues regarding the testing equipment. Several upgrades were previously carried out due to the intense operation time. The planned 300,000 cycles were completed with no data acquisition system or MTS ram problems.

A noticeable crack occurred at the midspan close to 2,000 cycles. The crack location and propagation caused strain gauges 1 and 3 to de-bond from the slab surface and as such their resulting data are not considered in the final criteria analysis. After the cracking initially developed, the crack propagated quickly for the next few thousand cycles before other minor cracking occurred in other parts of the midspan. The initial cracks grew in length but did not widen as cycling continued. Instead, it was found that the crack opening only increased in size with the adjustment to higher loadings. Photos of the de-bonding and crack propagation are found in Figure 5.1 and Figure 5.2.

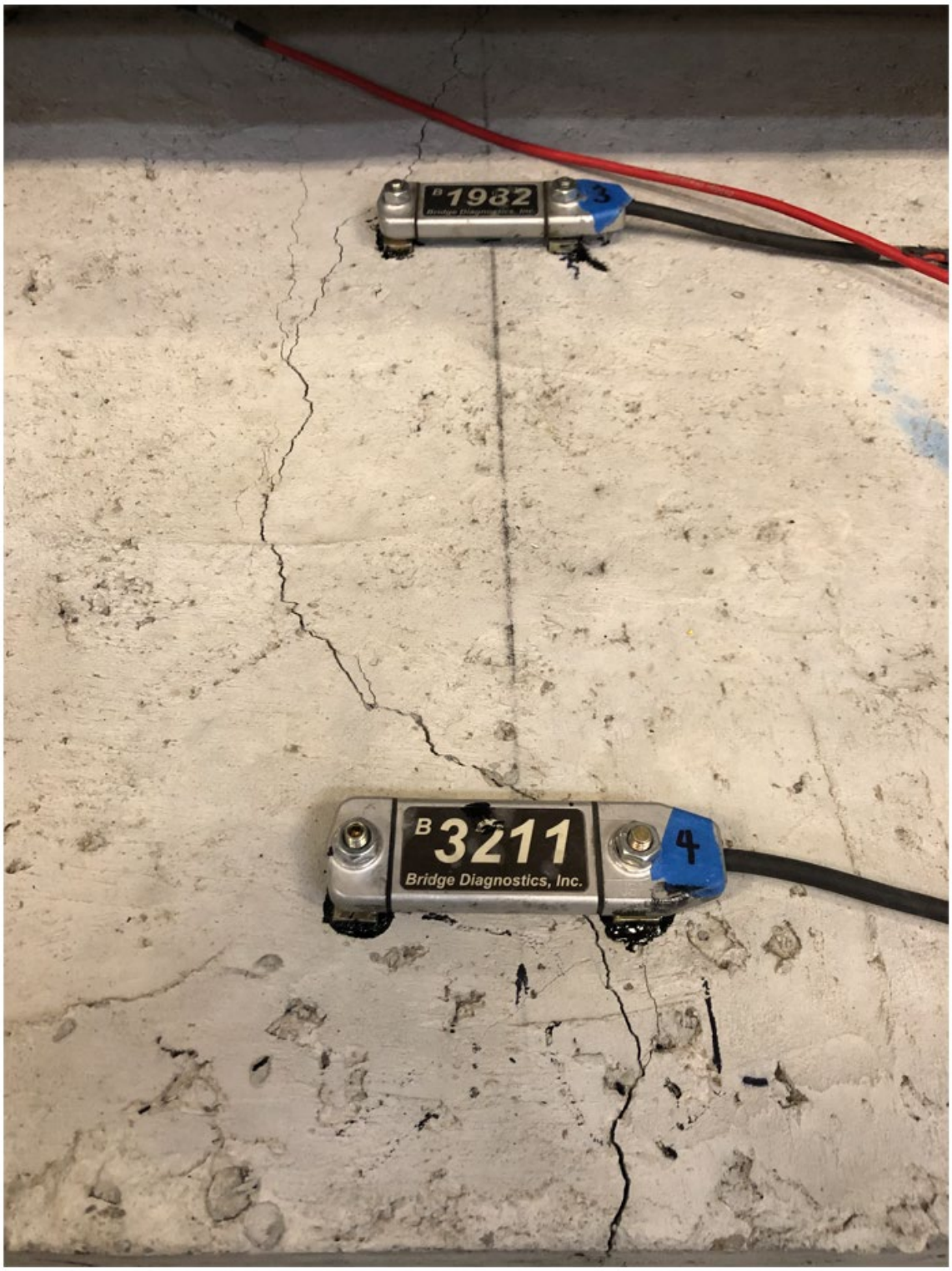

Figure 5.1 Surface Crack Propagation on Steel

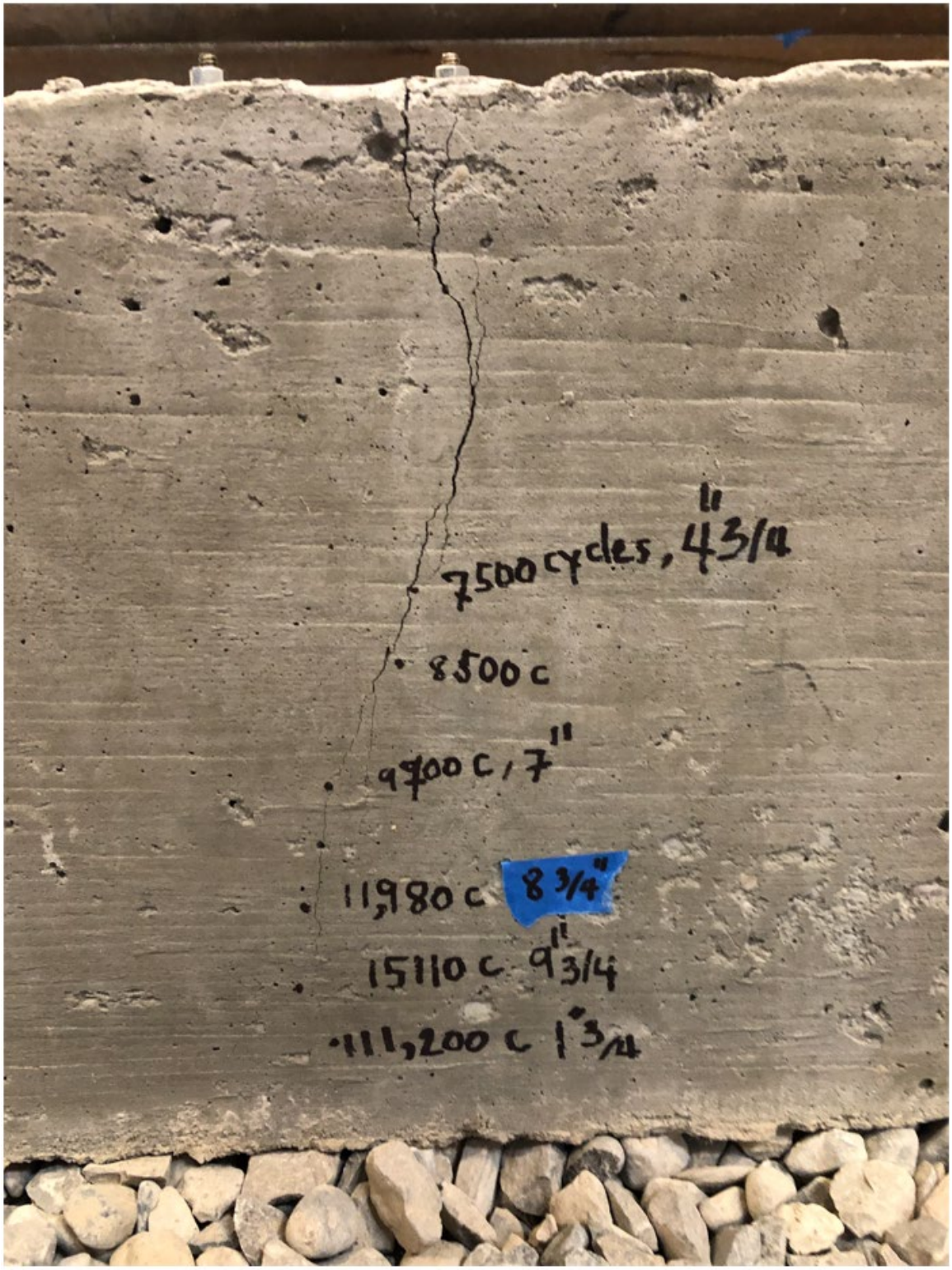

Figure 5.2 Side Crack Propagation in Panel with Steel Reinforcement

After completion of the first phase, a brief time was taken to evaluate equipment before continuing. As systems looked operational the second phase was then started, but ultimately paused as the hydraulic ram overheated and was forced to have a cool-down period. This time accounts for the second period of stress relaxation. No further issues occurred throughout testing. Phases 2 and 3 were designed to be extreme cases to assess the slab's ability to protect the electrical systems. Due to the early cracking found in phase 1, cycling for subsequent phases was reduced from 100,000 cycles to 10,000. This was done for two reasons: first, that the purpose of the second and third phases were to crack the concrete and since that had already been completed, the large number of cycles was no longer needed; Second, since there had already been a maintenance period, mechanical failure of the ram was a concern.

The following figure shows an example response during artificial aging. Gauge 4, shown below, was compared to the theoretical strain. In addition, it was compared to the internal strain gauges from Vaikasi (2021) and was found to be consistent with both the internal and theoretical strain. The variation over time is thought to be attributed to the settling of gravel and release of strain through microcracks.

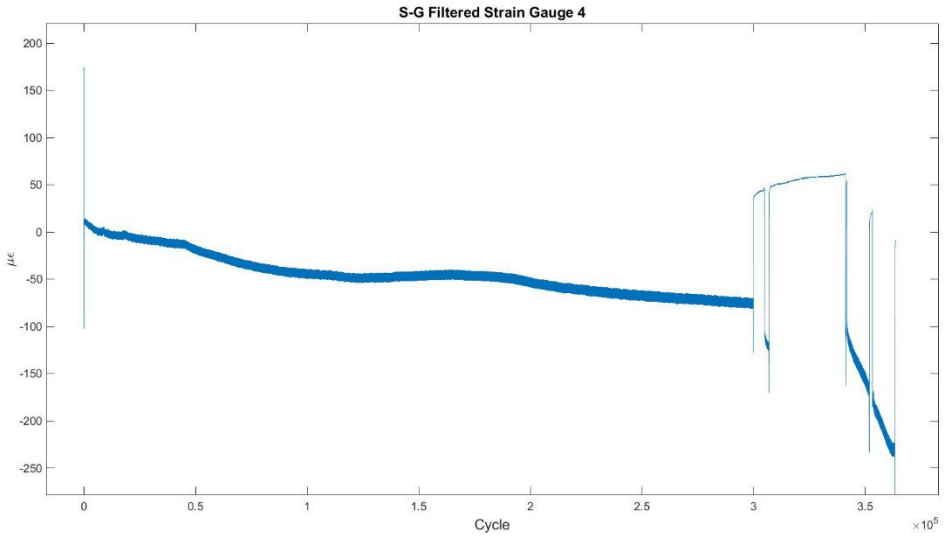

Figure 5.3 Strain Gauge 4

Note that the cracking in the middle of the slab is flexural cracking directly attributed to the bending of the slab. The major crack on either side can be attributed to flexural cracking as well, changing to shear at the head of the crack. Compression failure at the mid-span was also noted during the three-point bending test. Compression stress at the spreader beam contact was not found.

The results of the three-point bending test were very promising, and it was not until 25,000 lbs. that additional signs of failure were found. Several photos below show the progression of the flexural cracking. During the original loading, a slight misalignment caused bending in the supports, which never allowed a greater force than approximately 40,000 lbs. in the slab. After realigning the supports and starting the bending test again, the maximum force increased to 50,000 lbs., as shown in Figure 5.8. A graph of the second loading until failure is found in Figure 5.4. Following that are the photos of the expanding cracks and a graph that confirms the testing protocol with the internal MTS sensors.

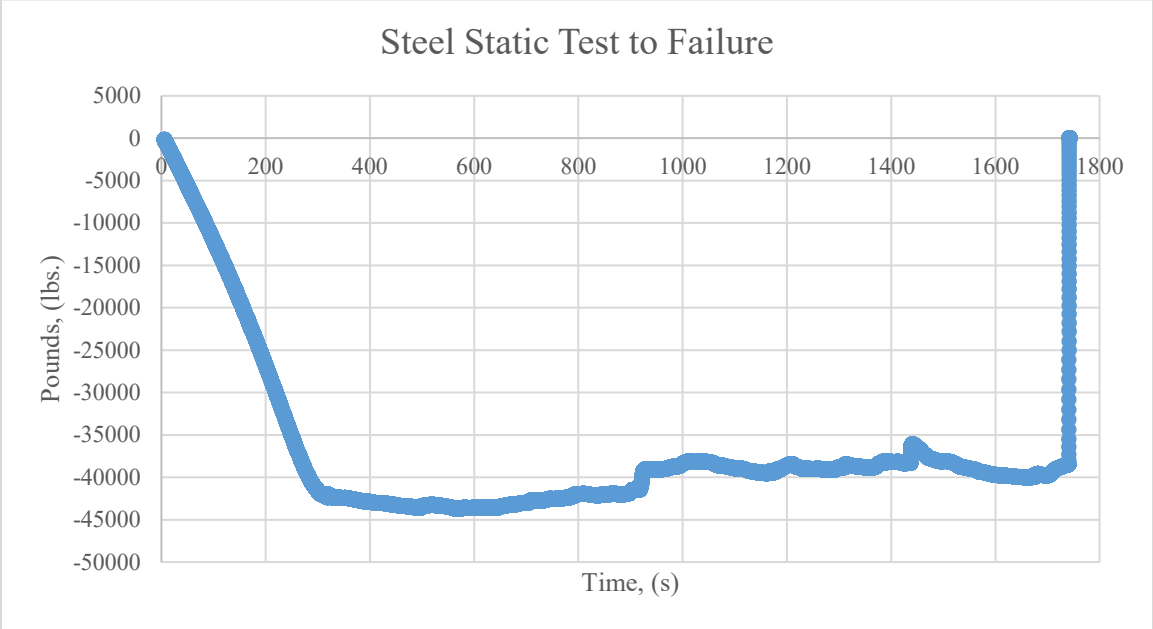

Figure 5.4 3-Point Bending Failure

Figure 5.5 Steel Cracks at Failure

Figure 5.6 Steel Cracks Reverse Side

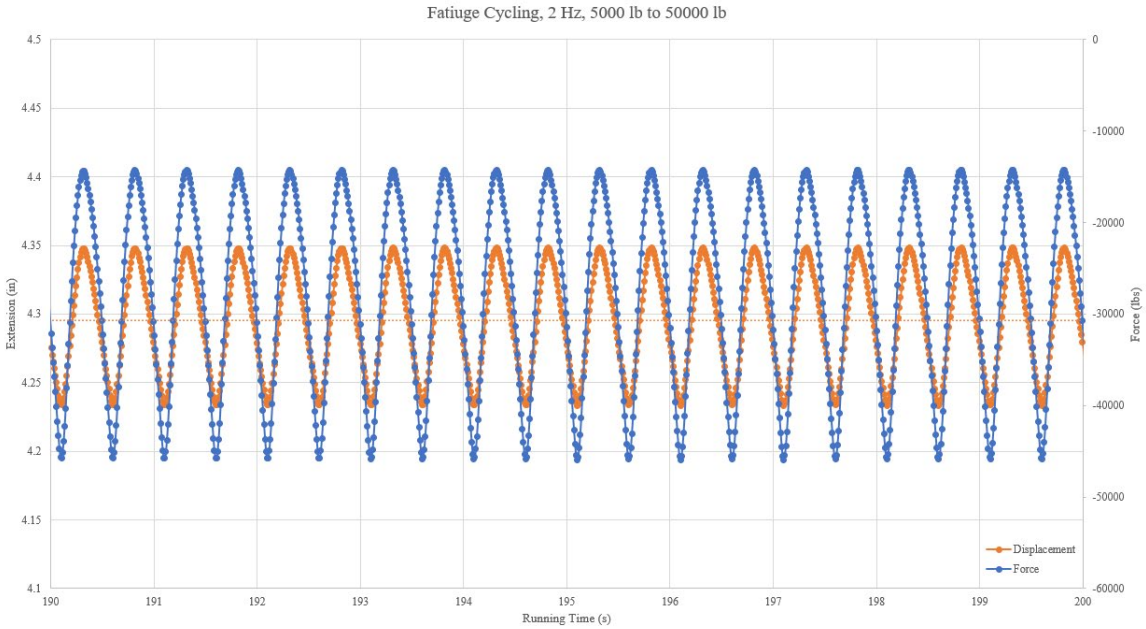

Figure 5.7 Fatigue Data From MTS

Though the midspan cracking grew, it was not the main mode of failure as originally predicted. A flexural-shear crack became the mode of failure. Concurrent research by Varghese (2021) showed that, although the concrete slab was drastically deformed, the embedded ITPS was still functional. According to the same research, the readings taken from the IPTS indicate the system will continue to work in some capacity until the Litz wires are sheared. Figure 5.13 shows that even under the extreme failure shown, no cable shear was detected. Due to the material properties of the Litz wire, it is unlikely to shear through any realistic loadings. This verifies work done by Gardner (2017) with the coating of the cables, and further serves to verify the ability of the system.

Figure 5.8 Steel Cracking at Midspan

Figure 5.9 Spalling Slab with Steel Reinforcement

Figure 5.10 Panel with Steel Reinforcement Catastrophic Failure

Figure 5.11 Steel Reinforcement Failure

Figure 5.12 Face of Steel Reinforced Slab After Failure

Figure 5.13 Litz Wire

5.2.2 GFRP Reinforced Slab (Specimen 2)

The material properties of GFRP indicate it is a critical material for the future of this research. Resistance to corrosion and interactivity with the electronics in the slab demonstrate that the success of this test is indicative of the technology's future. There were no mechanical issues during specimen 2's fatiguing process. Similar to specimen 1, early cracking occurred, though at a slightly later cycling time of 5,000 cycles. Due to the early cracking, phases 2 and 3 were reduced from 100,000 cycles to 10,000 cycles. Strain gauges 1 and 4 de-bonded as cracks propagated across the surface. The data collected from those sensors will not be considered as part of the final criteria evaluation.

Gauge 8, shown below, is indicative of the strain near the end of the embedded ITPS coils. Although a comparison of the midspan strain to the steel reinforced concrete panel would be beneficial, surface cracking propagated directly under the gauge at the midspan. Gauge 8 has expected values for its locations and will be sufficient for criteria analysis. As mentioned during the fatigue test of specimen 1, it is thought that the slight increase in strain over the first portion of phase one is a result of bed settlement. Gauge 8 is shown below.

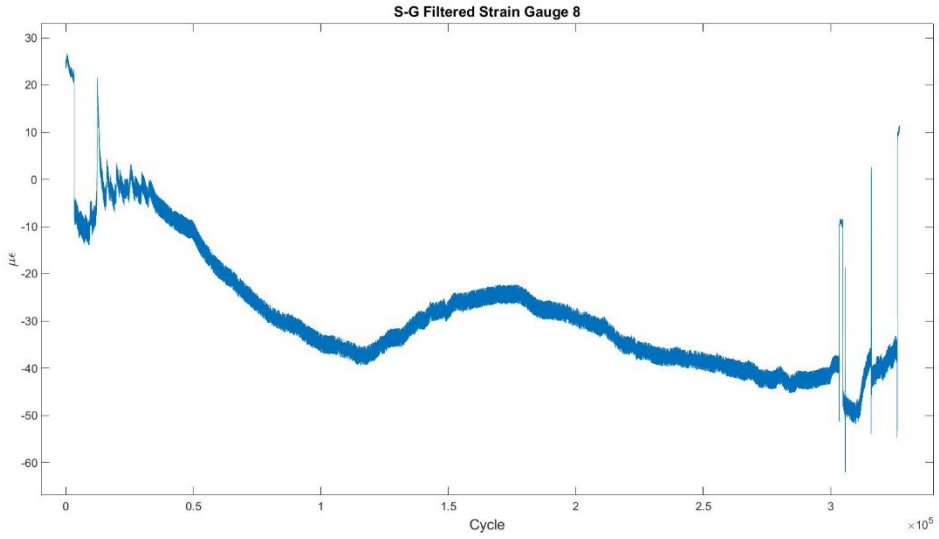

Figure 5.14 GFRP Strain Gauge 8 Fatiguing Results

Specimen 2 response seems to be more consistent with that of the steel reinforced slab. The difference in the strain data comes in the second and third phases where it seems the GFRP strain increases surpass the steel data, possibly suggesting that the overloading of the slab is causing the reinforcement to rupture. Cracking also seems to be more localized with fewer offshoots than in specimen 1. The following photos show the propagation of the crack over the face of the slab during the fatigue testing.

Figure 5.15 GFRP Surface Cracking

Figure 5.16 GFRP Side Cracking

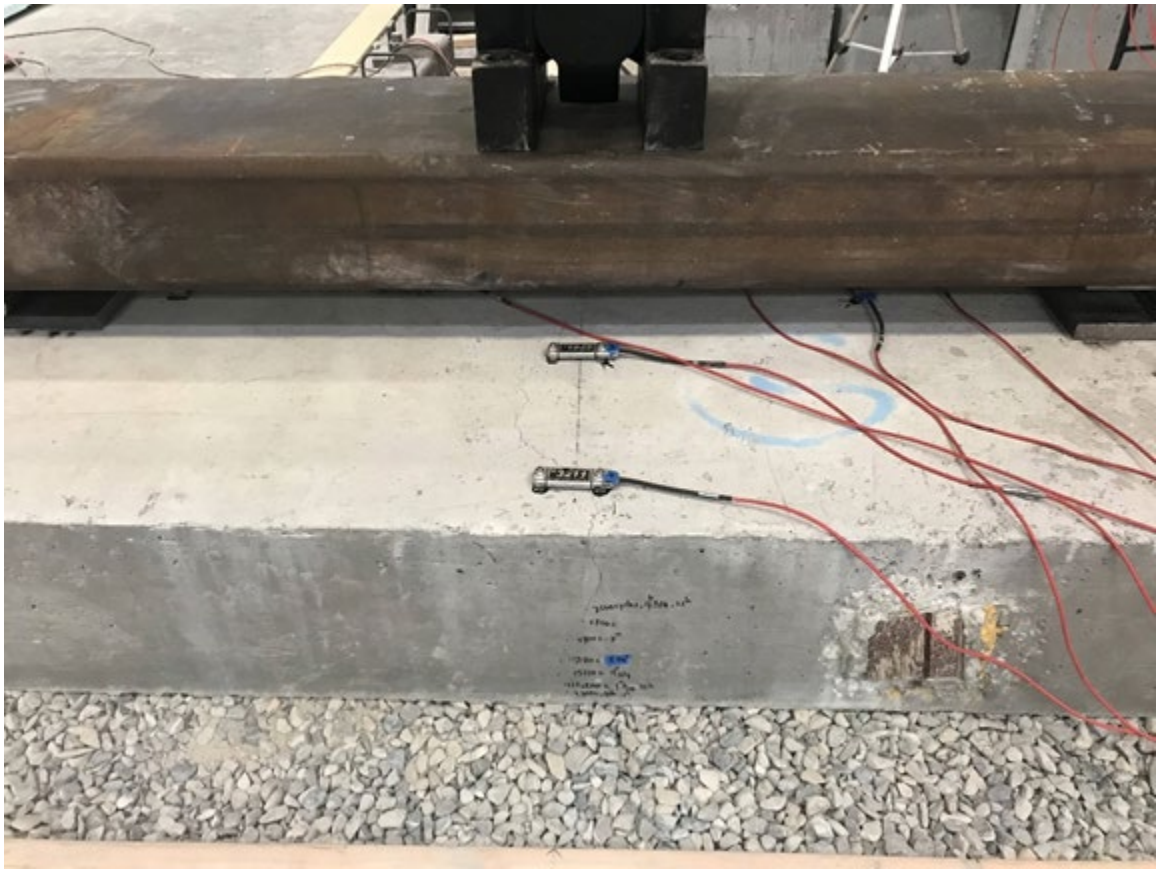

Figure 5.17 Overview of GFRP Fatigue Test

Figure 5.18 shows the full width of the test and the catastrophic failure that occurred close to 54,000 lbs. The relaxations seen in the 30,000 to 45,000 lbs. range can be attributed to cracking and increased flexure. Each lowering of force was accompanied with a new or increased crack until catastrophic failure. After the failure, the test followed unloading protocols. The full test proves that the testing protocol worked as designed. The mode of failure seems to be similar to specimen 1 except that the GFRP reinforcement ruptured, due to the lack of elastic behavior, causing a section to break apart completely. Figure 5.2 and Figure 5.3 show that the cracks started near the end of the electrical components.

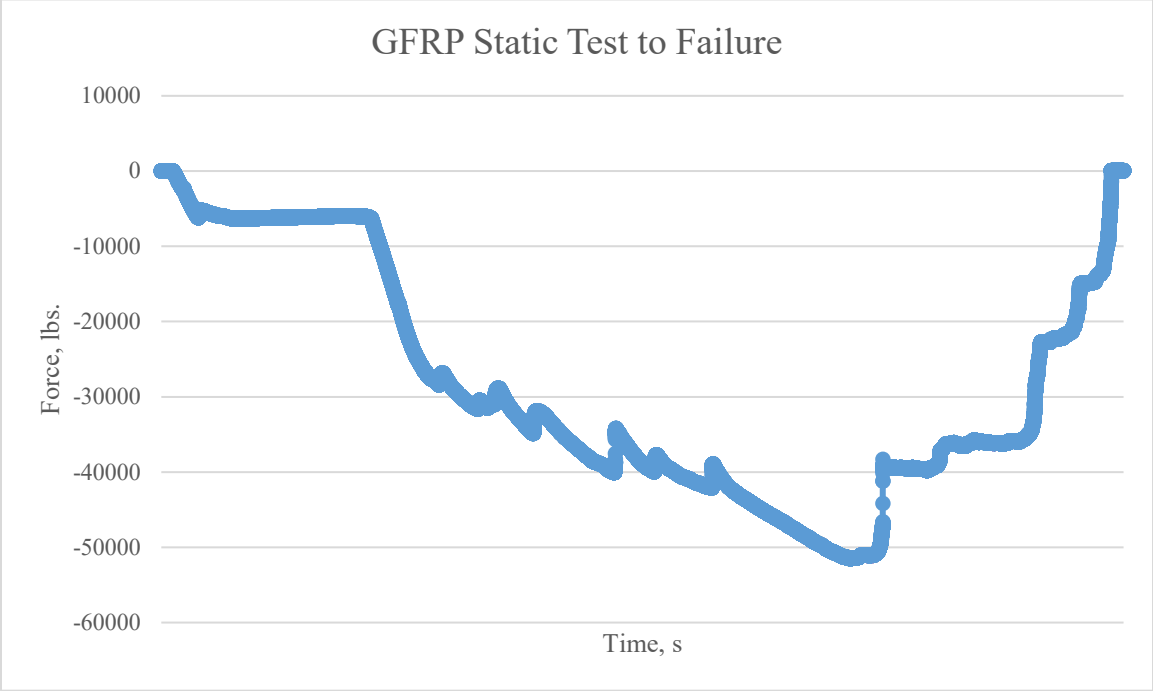

Figure 5.18 GFRP Static Test to Failure

Figure 5.19 Cracking During Static Test

Figure 5.20 GFRP Catastrophic Failure

Figure 5.21 GFRP Reinforcement Failure

Figure 5.22 GFRP Rupture Exposed

Figure 5.23 Face of GFRP Reinforced Slab After Failure

5.3 Other Results

5.3.1 Concrete Strength at Testing

No compressive cylinders were available at the time of testing, which would be critical to confirm the concrete strength at time of testing. As such, another method was used to estimate the concrete strength. The three-point bending test allows a calculation of the corresponding flexural strength or MOR. Following ACI 330.R, it is then possible to correlate the flexural strength to the compressive strength. Due to the nature of the three-point bend test, there is an inherent margin of error. The following shows the application of the calculations developed.

The calculation for the modulus of rupture for a rectangular slab in a three-point bending test is found in Equation 5.1 in which the dimensions of the slabs are known and given with the variables.

F is the load in pounds (lbs.)
L is the support span in inches (in.) at 72 inches.
b is the width in inches (in.) at 48 inches.
d is the thickness of the specimen in inches (in.) at 12 inches.
σ is the compressive strength of the concrete in lb/in^2

$$MOR = \frac{3FL}{2bd^2} \tag{5.1}$$

The max loading for the steel reinforced slab was found to be 43,730 lbs., and 51,475 lbs. for the GFRP reinforced slab. These values are used as the force (F). The equation to get the flexural strength from the compressive strength is found in ACI 330.R and is shown below in Equation 5.2. A hand check of the calculation in its entirety and the estimation of the compressive strength of concrete at time of testing are found in Appendix G.

$$MOR = 2.3\sigma^{2/3}$$

Rearranging to find the compressive strength.

$$\sigma = (\frac{MOR}{2.3})^{3/2} \tag{5.2}$$

An important consideration is that three-point bending testing can have a 10.15% increase in flexural strength when compared with a four-point bending test. As such, the MOR calculated will be decreased to show a more conservative value. Though conservative, this will be the closest value without more samples or compressive cylinders.

5.3.2 Internal vs External

This chapter has focused on the external gauges and the direct effects of the testing. The focus is due to the jurisdiction of this research; Vaikasi (2021) embedded fiberglass gauges to monitor the response the reinforcement has during testing. Calibration processes, advantages, and applications should be followed up through the corresponding research.

Without a comparison to the internal gauges, however, the external data lacks context. To effectively compare results, direct comparisons to both sets of data must be achieved. In addition, the data should in all cases reflect the theoretical strain found using basic static equations. First, through the theoretical strain using Equation 5.3, found below, we will be able to find the stress in units of psi.

$$\sigma = \frac{My}{I} \tag{5.3}$$

The y value is just the distance from the center of the beam to the face of the slab. The force is a known value, which can then be used to separate the single actuator force into the two supporter beam reactions. This creates a moment that can be calculated and subsequently used. The moment of inertia, Ix, is a much more difficult value to obtain. For a doubly reinforced concrete beam, the equations can provide an accurate value. However, the tested slabs have additional components that may affect the overall strength of the slabs.

To accurately estimate the material properties would prove impossible; however, taking the data strain and then using the known moment and distance y to calculate the necessary moment of inertia would provide a very accurate value over a few data points. The second moment of inertia for doubly reinforced concrete beams will be the minimum value, so that will be calculated and used as the conservative value. Appendix H shows the full calculation of the estimated modulus of inertia.

As can be seen in strain gauge 4, (Figure 5.3) specimen 1 does show a proportional response to the testing parameters. Other gauges, however, do not have the same clear response. Instead of the estimated values, the graphs show strain that is much lower than anticipated. It is theorized that the crack forced the slab to act as two separate pieces, which then caused the beam assumptions to break down. In addition to the crack development early into the testing, it is also on top of a semi elastic foundation. Though the previous calculations work until a point, they indicate the data were consistent with the theoretical findings without major manipulation.

5.3.3 S-N Curve

Concurrent research (Varghese, 2021) shows that the electrical performance, quantified by the quality factor, did not decrease significantly during the fatiguing results. In fact, it was only about 10% degradation even under double the design loading. Varghese (2021) indicates that the only test that caused significant damage was the static failure of specimen 2, and even with the failure shown in Figure 5.21, only a 50% decrease from the starting value was reported. This proves that the IPTS is sufficiently protected with roadway concrete. The IPTS will also be able to work in overloaded conditions, something that will allow the use of the technology in adverse conditions and increase the applicability of the technology.

The S/N factor was found for both slabs and graphed on the following figure. A table with the associated values is also included. Following the S/N equations, the data suggest that when compared with previous tests (Gardner 2017) an increase to the fatigue life of the slabs is found in the slabs. This test compares the stress experienced by a specimen to the modulus of rupture, which makes it ideal to compare slabs of different sizes and strengths.

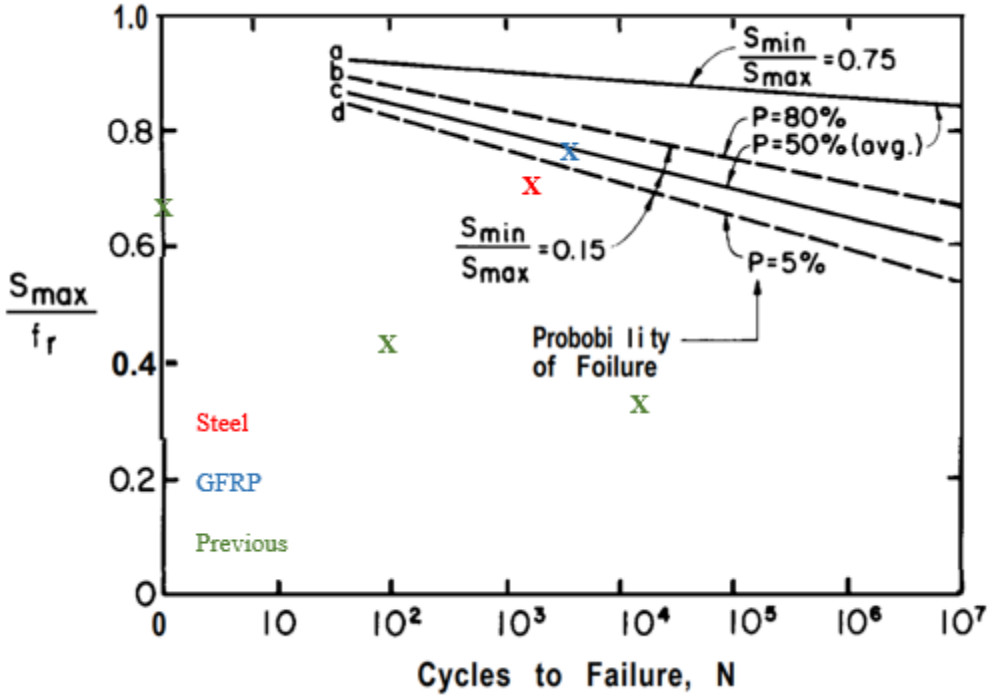

Figure 5.24 S/N Graph (ACI 1997)

Table 5.1 S/N Graphing Data

Test	N	S
Steel	2000	0.66
GFRP	5000	0.73
Previous Test 1	91	0.41
Previous Test 2	10053	0.322
Previous Static	1	0.69

5.3.4 Strain Gauge Temperature Drift

The BDI strain system results assume that there is little to no temperature change during any testing sequence. Although temperature variations during the time of testing can be upwards of 11 degrees overnight, the SMASH lab was set to maintain a constant temperature. In addition, full Wheatstone bridges are known to minimize minor temperature fluctuation because each part of the resistive bridge is affected the same way, ultimately not changing the end result. Due to the minimal temperature changes, no temperature drift was considered.

5.4 Future Considerations

This experiment proves that the current system can withstand loading much greater than what would be seen during standard traffic conditions. Future experiments should consider additional or more densely spaced reinforcement to delay the cracking of the slabs. Ensuring the concrete strength for future pours is a first step; refining the strain gauge placement and gauge of the data collector would free up needed memory. These simple changes would allow an increase in sampling frequency, and this would help further determine a baseline to compare the before and after of the cracks.

As previously stated, no experiment is without flaws. Future considerations should be made to ensure the continual safe use of this technology. OSB was selected as a base to ensure gravel containment without breaking to the high forces during the experiment. Though the OSB was successful in that aspect, it was noted that in some parts of the experiment there was a definite flexural of the gravel container. This flexural may have had a significant effect in the early cracking or the reduction of strain experienced by the slab, thereby making the slab perform better than an exact replica of the road. Future testing may consider a stiffer material for the gravel box to eliminate base flexure as a variable. More testing should also be considered to provide a statistically significant dataset.

The fatigue test took place over three days. Though care was taken to use realistic loadings, rest periods may have an additional effect and prolong concrete lifespan (Castro, 2006) In addition, the experiment was performed inside a laboratory where the temperature and humidity were controlled. No tests were done for probable weather aging or environmental effects such as ice buildup. Rain and snow and subsequent freezing and re-freezing is known to increase crack widths and is a major concern of many states; the cracking found during the experiment could be a critical point of failure for internal electronics. Future research should include the effects that freeze-thaw cycles will have on the performance of the electrical system. Note that the testing done was proven successful, confirming previous research in both Gardner (2017) and Varghese (2020). Below is a graph of the impedance, or effective resistance, showing the change in resistance after the static testing. The minor change indicates that the technology is still viable after failure and future experiments may include a larger sample size to further determine the effectiveness of the technology.

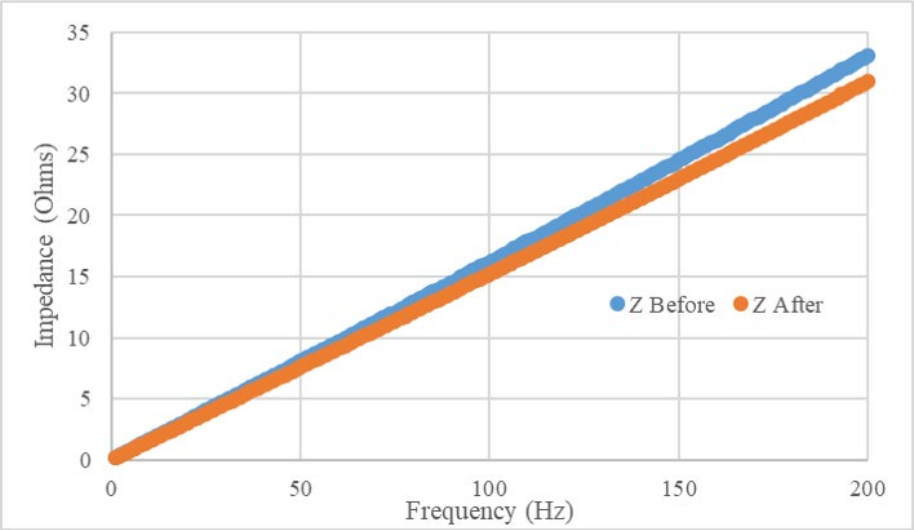

Figure 5.25 Impedance After 3-Point Bending

5.5 Summary

Two reinforced slabs were artificially aged, and the gathered data were analyzed. The summarized results can be seen in Table 5.2. The two criteria at the start of the experiment were the concrete serviceability and the performance of the ITPS during testing. It is clear that even under overloaded situations, both specimens were able to maintain the fidelity of the electric system. The system's performance under extreme conditions also suggests the technology has promise for practical use. In regard to the first criteria, the early cracking that occurred can be an indicator of a failure in the concrete or reinforcement. In the scope of the testing protocols, it can be said that both specimens successfully protected the electrical system and maintained its performance.

Table 5.2 Study Summary

Summary	Specimen 1 (Steel)	Specimen 2 (GFRP)
1st Crack (Cycles)	2000	5000
Major Cracking (Cycles)	15,000	10,470
Ultimate Static Load (lbs.)	50,000	54,000
Compressive Strength (psi)	4,567	
Total Cycles	120,000	
S/N	0.66	0.73

The slabs were shown to have acceptable strength and fatigue life over the course of testing. It was found that the alternative reinforcement, GFRP, showed a greater resistance to both fatigue and static loading. The data gathered from both specimens were actionable and comparable to previous results, and any further testing on similar slabs should be able to use the data to measure quantifiable improvements. Though improvements to the base design can be made, it is clearly seen that the technology fulfills both main criteria set out for the success of the project. The IPTS is technology that is feasible for long-term use in roadways.

6. CONCLUSIONS

Electronic vehicle usage has increased over the last few years with many car manufacturers resolving to completely convert to EVs within the next few decades. The ability to dynamically charge vehicles may be important for the future of infrastructure improvements. Embedding IPTSs in roadway concrete with GFRP reinforcement is a way to allow the technology to be protected from the rigors of everyday travel while providing long-term utility. The experiments have shown that an embedded IPTS is a viable solution.

The testing of two slabs with embedded IPTSs were subjected to fatigue and static loading. All fatigue loading was performed at 2 Hz over 320,000 cycles at three separate force loadings. Static loading consisted of a constant rate until catastrophic failure was reached. Data were gathered from a variety of strain gauges arranged at critical locations on the slabs. The gauges were placed with the intent to evaluate the IPTS capabilities under adverse conditions. Based on experiment results, the following conclusions can be made about the long-term feasibility of the embedded IPTS.

1. Both slabs continued to function electronically during the fatigue cycling.
    a. Cracking occurred early, but relatively minor adjustments would allow the slabs to have longer lifespans.

2. Even after failure, both IPTSs were functional.
    a. Both the static and fatiguing tests prove that this technology will survive adverse conditions and loadings.
    b. This technology is a viable solution for long-term use in roadway concrete.

3. The aggregate in the slabs was found to be well distributed with no settlement. This indicates that pre-casting could be a viable production method for the IPTS.

4. The loading and testing protocols used were able to provide actionable data and could be used in future experiments.

By comparing the steel reinforced slab to the GFRP reinforced slab, the experiment was able to confirm that the fiberglass reinforcement is a viable alternative to steel reinforcement in roadway concrete. Both portions of the experiment showed that the alternative material and current design were adequate for the design criteria. Current material properties would also prove valuable over the lifespan of the technology. Implementation of the GFRP reinforcement means that more eco-friendly technology will be able to compete with standard design more directly.

Future research should include steps to understand the environmental response and heavy use of the technology. To that end, additional research is currently being performed to further both the efficiency and durability of an IPTS. The system will be installed at the Electronic Vehicle and Roadway test track at Utah State University, a laboratory that further tests the capabilities of electric vehicles in realistic conditions. More GFRP reinforced slabs should also be tested in simple beam configurations to further understand the life cycle of the IPTS.

7. REFERENCES

Abdelkarim, O. I., Ahmed, E. A., Mohamed, H. M., & Benmokrane, B. (2019). "Flexural strength and serviceability evaluation of concrete beams reinforced with deformed GFRP bars." *Engineering Structures*, 186, 282–296. https://doi.org/10.1016/j.engstruct.2019.02.024

ACI Committee 325. (2002). ACI 325.12R.02: *Guide for Design of Jointed Concrete Pavements for Streets and Local Roads*. American Concrete Institute.

ACI Committee 440. (2015). ACI 440.1R-15: *Guide for the Design and Construction of Structural Concrete Reinforced with Fiber-Reinforced Polymer Bars*.

ACI Committee 544. (2018). ACI 544.4R.18: *Guide to Design with Fiber-Reinforced Concrete*. American Concrete Institute.

American Institute of Steel Construction. *Manual of Steel Construction, 15th Edition*. (2005). Chicago: AISC 2005.

BDI Structural Testing & Monitoring Systems. (2020, November 3). ST350 Strain Transducer. BDI Structural & Monitoring Systems. https://bditest.com/product/st350.strain.transducer/.

Bromba, M. U. A. A., & Ziegler, H. (1981). "Application hints for Savitzky-Golay digital smoothing filters." *Analytical Chemistry*, *53*(11), 1583–1586. https://doi.org/10.1021/ac00234a011

Campbell Scientific. (n.d.). CR3000 – Measurement and Control Datalogger. CR3000: Measurement and Control Datalogger. https://www.campbellsci.com/cr3000.

Chen, F., Taylor, N., & Kringos, N. (2015). "Electrification of roads: Opportunities and challenges." *Applied Energy*, *150* (15 July 2015), 109–119. https://doi.org/10.1016/j.apenergy.2015.03.067

Coni, M., Isola, R., Oliveira, J. R. M. M., Portas, S., & Isola, R. (2008). "FE evaluation of 4-point bending test for fatigue cracking assessment." *Pavement Cracking: Mechanisms, Modeling, Detection, Testing and Case Histories*, *June 2008*, 271–281. https://doi.org/10.1201/9780203882191.ch27

Covic, G. A., & Boys, J. T. (2013). "Inductive power transfer." *Proceedings of the IEEE*, *101*(6), 1276–1289. https://doi.org/10.1109/JPROC.2013.2244536

Deng, P., Matsumoto, T., Gaedicke, C., & Roesler, J. (2010). "Fracture-Based Method to Determine Flexural Capacity of Concrete Beams on Soil." *Road Materials and Pavement Design*, *11*(2), 361–385. https://doi.org/10.1080/14680629.2010.9690280

Gardner, T. (2017). "Wireless Power Transfer Roadway Integration" [Utah State University]. https://doi.org/10.1017/CBO9781107415324.004

Hanson, J. M., Antrim, J. D., Brown, E. I., Hiisdorf, H. K., Segner, E. P., & Hawkins, N. M. (1997). "Considerations for Design of Concrete Structures Subjected to Fatigue Loading Reported by ACI Committee 215." *Design*, 74.

Hsu, T. T. C. (1982). "Fatigue of Plain Concrete." *ACI Journal Proceedings*, *78*(4), 292–304. https://doi.org/10.14359/6927

Hwan, O. B. (1986). "Fatigue Analysis of Plain Concrete in Flexure." *Journal of Structural Engineering*, *112*(2), 273–288. https://doi.org/10.1061/(ASCE)0733.9445(1986)112:2(273)

Kumar, S. V., & GangaRao, H. V. S. (1998). "Fatigue Response of Concrete Decks Reinforced with FRP Rebars." *Journal of Structural Engineering*, *124*(1), 11–16. https://doi.org/10.1061/(asce)0733.9445(1998)124:1(11)

Lee, J., & Lopez, M. M. (2014). "An Experimental Study on Fracture Energy of Plain Concrete." *International Journal of Concrete Structures and Materials*, *8*(2), 129–139. https://doi.org/10.1007/s40069.014.0068.1

McRory, J. (2020). "Experimental Static and Cyclic Behavior of Hybrid Non-Metallic Bridge Decks Reinforced with Discrete GFRP Rebar and GFRP Macrofiber." [Master's thesis] Utah State University.

Onar, O. C., Miller, J. M., Campbell, S. L., Coomer, C., White, C. P., & Seiber, L. E. (2013). "A novel wireless power transfer for in-motion EV/PHEV charging." *2013 Twenty-Eighth Annual IEEE Applied Power Electronics Conference and Exposition (APEC)*, 3073–3080. https://doi.org/10.1109/APEC.2013.6520738

Press, W. H., & Teukolsky, S. A. (1990). "Savitzky-Golay Smoothing Filters." *Computers in Physics*, 4(6), 669. https://doi.org/10.1063/1.4822961

Roesler, J. R. R. (2006). "Fatigue resistance of concrete pavements." *6th International DUT–Workshop on Fundamental Modelling of Design and Performance of Concrete Pavements*, *September*. https://pdfs.semanticscholar.org/0336/fbc6399315fdc18ccb2bb6a959f018a55b79.pdf

Trejo, D., Aguiñiga, F., Yuan, R. L., James, R. W., & Keating, P. B. (2005). "Characterization of Design Parameters for Fiber Reinforced Polymer Composite Reinforced Concrete Systems." *Security*, *7*(2).

Vaikasi, Pilaiwan. (2021). "Constructability and Durability of Wireless Charging Systems Embedded into Concrete Pavements for Electrical Vehicles." [Unpublished doctoral dissertation]. Utah State University

Varghese, Benny. (2021). "Roadway-Embedded Transmitters and Multi-Pad Receivers for High Power Dynamic Wireless Power Transfer." [Unpublished doctoral dissertation]. Utah State University.

Xu, C., Anzhi, Y., Liao, M., & Chunan, T. (2011). "Analysis of periodic cracks in surface layer of pavement structures." *Engineering Failure Analysis*, 18(1), 411–420. https://doi.org/10.1016/j.engfailanal.2010.09.023

8. APPENDICES

APPENDIX A. STRAIN GAUGE FACTORS

The following tables and graphs are the complete calibration and linear estimations required or the strain gauge used in the experiment. Their creation and use are discussed in Chapter 4. This appendix also contains a verification of expected strain values.

Table A.1 Strain Calibration Table for Strain Gauge 1

Strain 1	1996	GGF	579.5
	Expected		Reality
Load (P)	**σ=My/I**	**με**	**CR3000**
0	0	0	552.42
80	105.179	3.627	547.56
120	157.769	5.440	544.5
200	262.948	9.067	538.89
240	315.538	10.881	535.02

R^2	Y intercept	Offset
0.9949	.0.6264879	346.4107

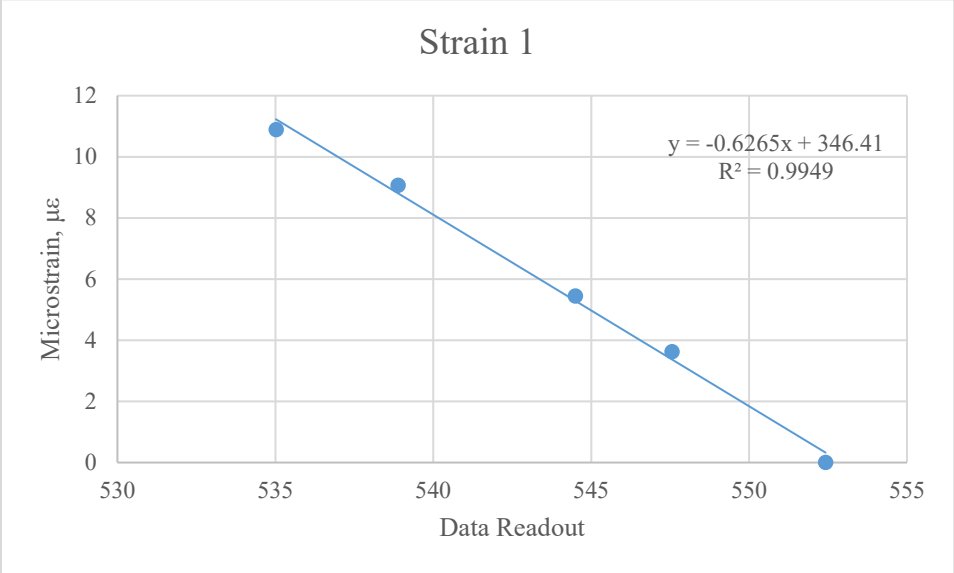

Figure A.1 Linear Estimation Graph from Strain Calibration Table

Table A.2 Strain Calibration Table for Strain Gauge 2

Strain 2	1990	GGF	517.5
	Expected		Reality
Load (P)	**σ=My/I**	**με**	**CR3000**
0	0	0	.221.71
80	105.179	3.627	.223.87
120	157.769	5.440	.225.25
200	262.948	9.067	.227.84
240	315.538	10.881	.228.87

R^2	Y-intercept	Offset
0.9981	.1.485474	.329.1834

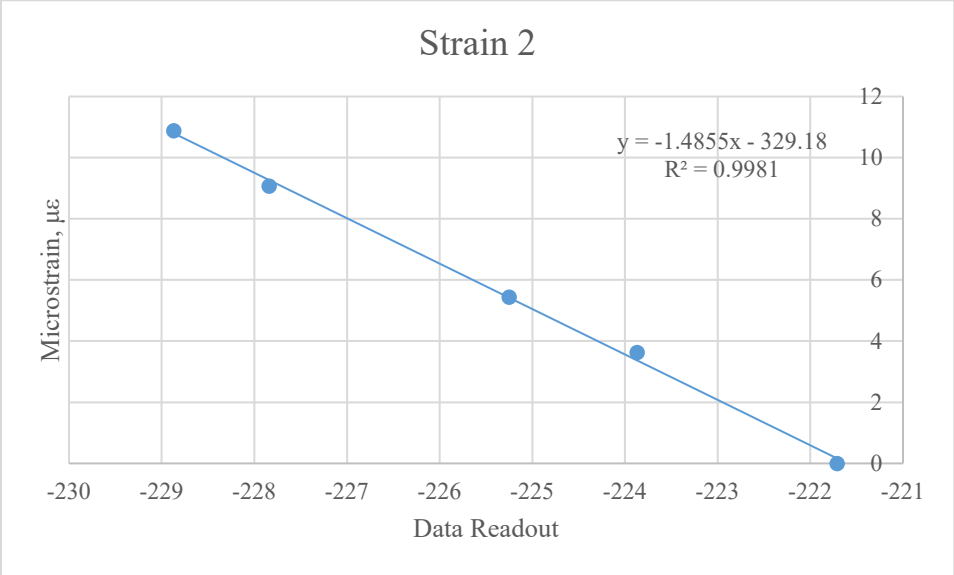

Figure A.2 Linear Estimation Graph from Strain Calibration Table

Table A.3 Strain Calibration Table for Strain Gauge 3

Strain 3	1982	GGF	422.2684
	Expected		Reality
Load (P)	**σ=My/I**	**με**	**CR3000**
0	0	0	.1016.47
80	105.179	3.627	.1022.65
120	157.769	5.440	.1024.77
200	262.948	9.067	.1030.83
240	315.538	10.881	.1033.37

R^2	Y-intercept	Offset
0.9983	.0.6440136	.654.709

Original GGF 508.8, R^2 .9787, slope .82993

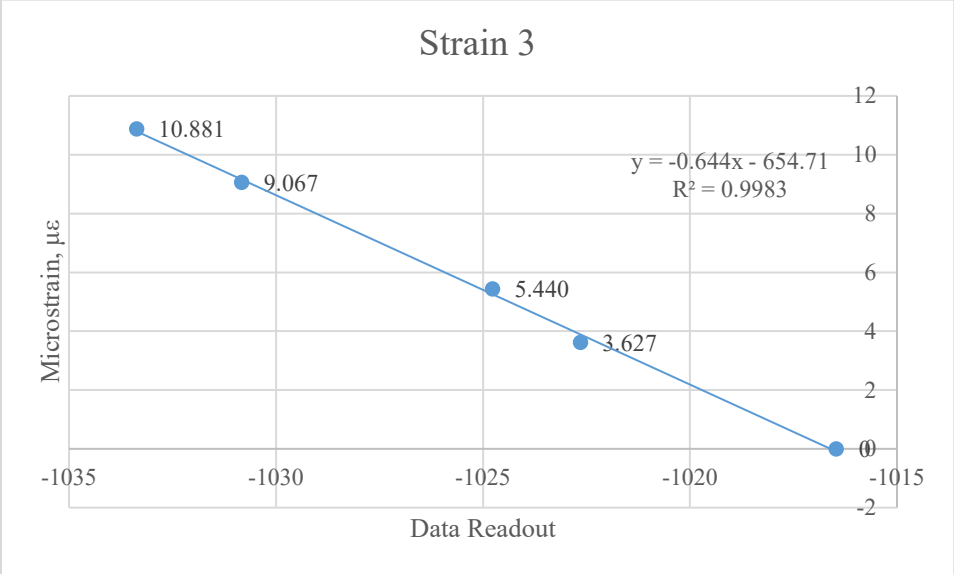

Figure A.3 Linear Estimation Graph from Strain Calibration Table

Table A.4 Strain Calibration Table for Strain Gauge 4

Strain 4	3211	GGF	499.2
	Expected		Reality
Load (P)	**σ=My/I**	**με**	**CR3000**
0	0	0	.394.24
80	105.179	3.627	.397.56
120	157.769	5.440	.399.56
200	262.948	9.067	.404.56
240	315.538	10.881	.405.9

R^2	Y-intercept	Offset
0.9921	.0.888308	.349.8437

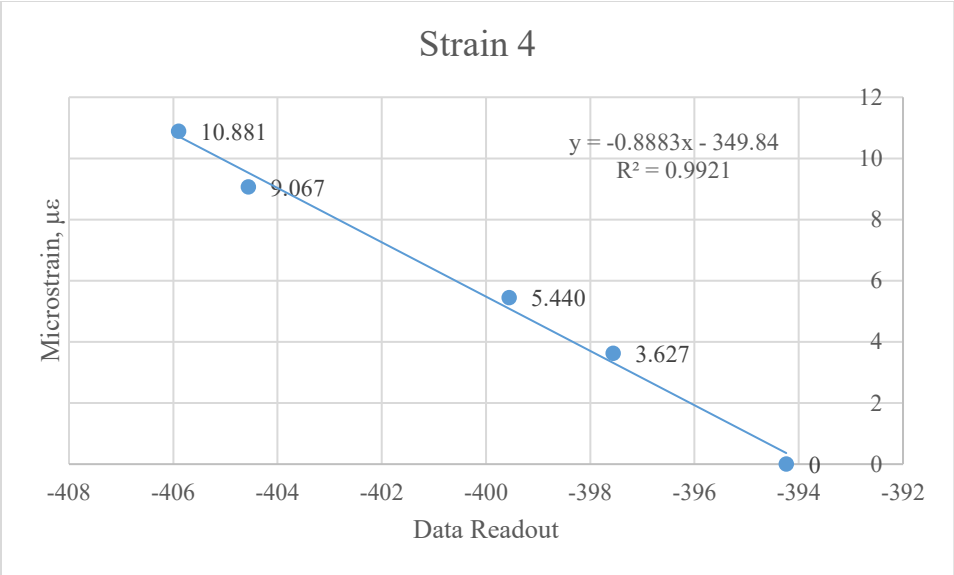

Figure A.4 Linear Estimation Graph from Strain Calibration Table

Table A.5 Strain Calibration Table for Strain Gauge 5

Strain 5	1972	GGF	527.8
	Expected		Reality
Load (P)	**σ=My/I**	**με**	**CR3000**
0	0	0	212.14
80	105.179	3.627	209
120	157.769	5.440	207.21
200	262.948	9.067	204.03
240	315.538	10.881	201.74

R^2	Y-intercept	Offset
0.9969	.1.0578077	224.583

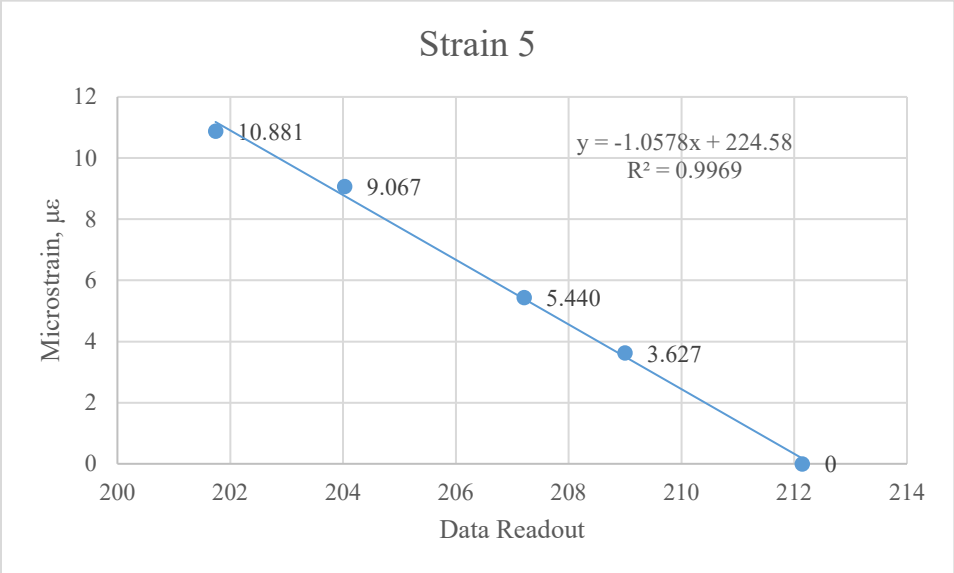

Figure A.5 Linear Estimation Graph from Strain Calibration Table

Table A.6 Strain Calibration Table for Strain Gauge 6

Strain 6	2611	GGF	539.5
	Expected		Reality
Load (P)	**σ=My/I**	**με**	**CR3000**
0	0	0	423.32
80	105.179	3.627	420.36
120	157.769	5.440	418.73
200	262.948	9.067	415.13
240	315.538	10.881	412.61

R^2	Y-intercept	Offset
0.9916	.1.018406	431.52734

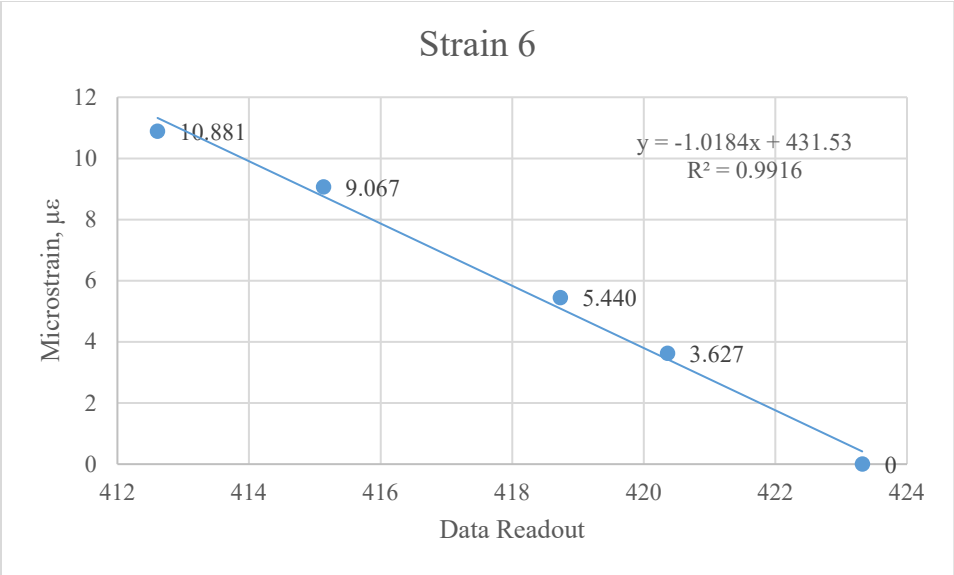

Figure A.6 Linear Estimation Graph from Strain Calibration Table

Table A.7 Strain Calibration Table for Strain Gauge 7

Strain 7	2612	GGF	515.9
	Expected		Reality
Load (P)	**σ=My/I**	**με**	**CR3000**
0	0	0	.39.75
80	105.179	3.627	.44.43
120	157.769	5.440	.47.7
200	262.948	9.067	.53.38
240	315.538	10.881	.56.66

R^2	Y-intercept	Offset
0.9965	.0.6370761	.25.0213

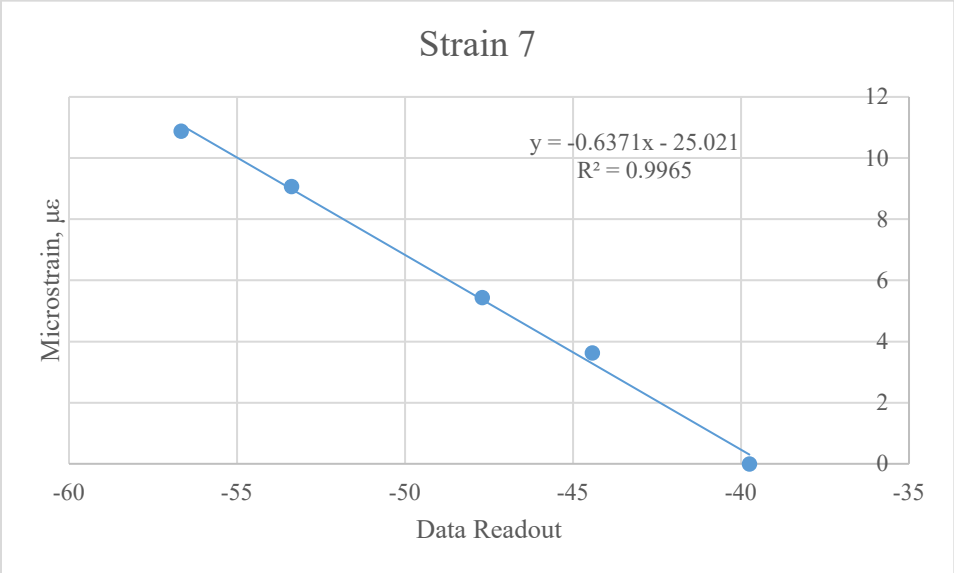

Figure A.7 Linear Estimation Graph from Strain Calibration Table

Table A.8 Strain Calibration Table for Strain Gauge 8

Strain 8	1973	GGF	509.6
	Expected		Reality
Load (P)	**σ=My/I**	**με**	**CR3000**
0	0	0	.170.96
80	105.179	3.627	.173.34
120	157.769	5.440	.174.7
200	262.948	9.067	.177.59
240	315.538	10.881	.179.63

R^2	Y-intercept	Offset
0.9918	.1.257673	.214.5966

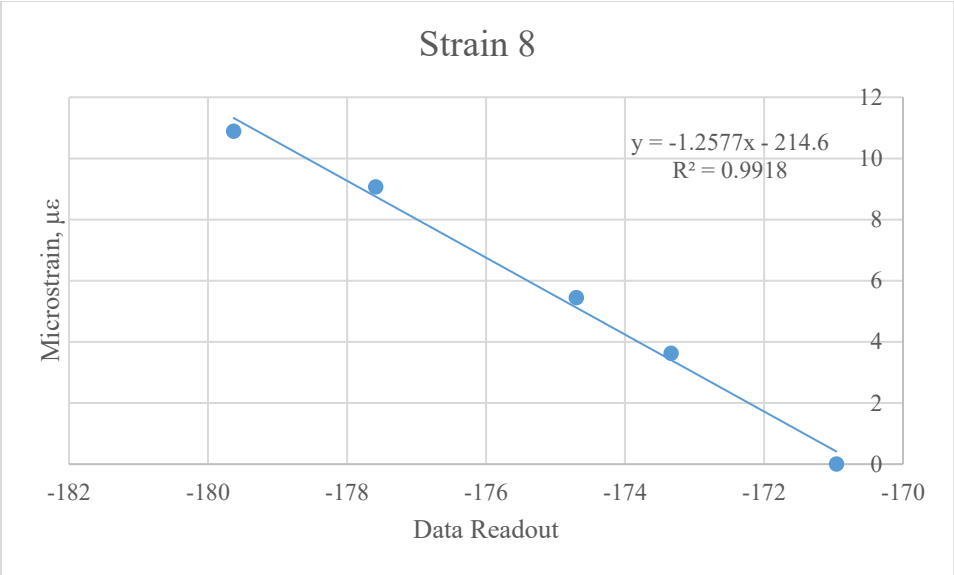

Figure A.8 Linear Estimation Graph from Strain Calibration Table

Table A.9 Calibration Data for LVDT

LVDT	
Expected	Reality
Dist (in.)	**CR3000**
0	.30.2
0.250	.28.12
0.500	.22.19
0.750	.14.46
1.000	.8.78
1.250	.2.14
1.500	4.77
1.750	11.64
2.000	18.67
2.250	26.13
2.500	30.1
R^2	0.9955
Y-Intercept	Offset
0.034592	0

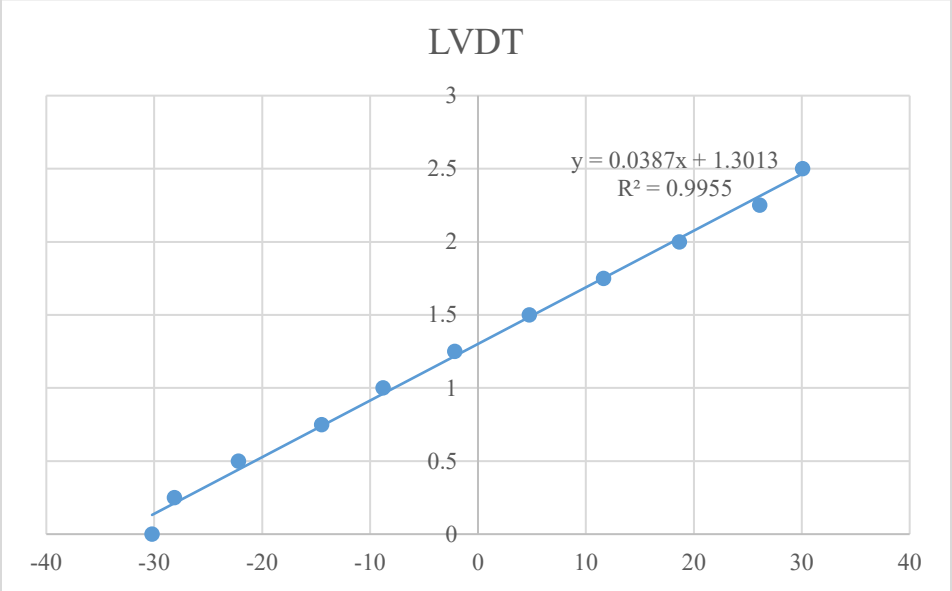

Figure A.9 Linear Estimation for LVDT

Strain Gauge Calibration Hand Check

Moment Diagram from the AISC Manual, 15th edition

Beam used: W8x21

$Iy := 75.3\ in^4$

$y := 4.125\ in = 0.3438\ ft$

$E := 29000000\ \frac{lb}{in^2}$

$L := 7\ ft$

$a := 2\ ft = 24\ in$

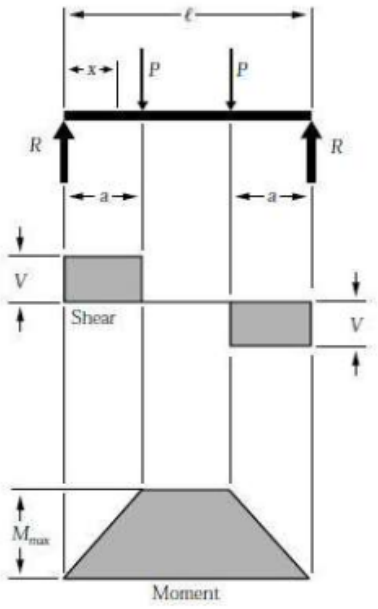

Weight of Plates, w

$w := 40\ lb$

w.x is w times the amount of plates for the total weight used, P

$w_0 := w \cdot 0 = 0\ lb$

$M_0 := w_0 \cdot a = 0\ lb\ in$

$\sigma_0 := \frac{M_0 \cdot y}{Iy} = 0\ \frac{lb}{in^2}$

$\mu\varepsilon_0 := \frac{\sigma_0}{E} \cdot 10^6 = 0$

$w_{80} := w \cdot 2 = 80\ lb$

$M_{80} := w_{80} \cdot a = 1920\ lb\ in$

$\sigma_{80} := \frac{M_{80} \cdot y}{Iy} = 105.1793\ \frac{lb}{in^2}$

$\mu\varepsilon_{80} := \frac{\sigma_{80}}{E} \cdot 10^6 = 3.627$

$w_{120} := w \cdot 3 = 120\ lb$

$M_{120} := w_{120} \cdot a = 2880\ lb\ in$

$\sigma_{120} := \frac{M_{120} \cdot y}{Iy} = 157.7689\ \frac{lb}{in^2}$

$\mu\varepsilon_{120} := \frac{\sigma_{120}}{E} \cdot 10^6 = 5.44$

$w_{200} := w \cdot 5 = 200\ lb$

$M_{200} := w_{200} \cdot a = 4800\ lb\ in$

$\sigma_{200} := \frac{M_{200} \cdot y}{Iy} = 262.9482\ \frac{lb}{in^2}$

$\mu\varepsilon_{200} := \frac{\sigma_{200}}{E} \cdot 10^6 = 9.067$

$w_{240} := w \cdot 6 = 240\ lb$

$M_{240} := w_{240} \cdot a = 5760\ lb\ in$

$\sigma_{240} := \frac{M_{240} \cdot y}{Iy} = 315.5378\ \frac{lb}{in^2}$

$\mu\varepsilon_{240} := \frac{\sigma_{240}}{E} \cdot 10^6 = 10.881$

Figure A.10 Hand Check of Strain Gauge Calibration

APPENDIX B. EXCERPTS OF THE CAMPBELL SCIENTIFIC CODE

Excerpts to the Campbell Scientific code used for data acquisition are given below.

'DiffVoltCh11H_SECh_21: ST350#05_Signal+

'DiffVoltCh11L_SECh_22: ST350#05_Signal.

'DiffVoltCh12H_SECh_23: ST350#06_Signal+

'DiffVoltCh12L_SECh_24: ST350#06_Signal.

'DiffVoltCh13H_SECh_25: ST350#07_Signal+

'DiffVoltCh13L_SECh_26: ST350#07_Signal.

'DiffVoltCh14H_SECh_27: ST350#08_Signal+

'DiffVoltCh14L_SECh_28: ST350#08_Signal.

'AnalogGrond_AG : Return ground for ST350 excitations. All AGs (upside down trees) are same ground.

'Excitation_Ch_Vx1 :

'Excitation_Ch_Vx2 : Excitation for ST350's #01.#03

'Excitation_Ch_Vx3 : Excitation for ST350's #04.#06

'Excitation_Ch_Vx4 : Excitation for ST350's #07.#08

'#################

VoltDiff(LVDT_mV,1,mV5000,2,True,0,250,1.0,0.0)

LVDT_Distance = (LVDT_mV*LVDT_Mult)+LVDT_oSet

BrFull(ST350_mVPV(),8,mV50,7,Vx2,3,5000,False,False,0,250,1.0,0.0)

'\\

ST350_uStrainraw()=(ST350_mVPV()*ST350_Mult2())+ST350_oSet2()

'//

'#################

APPENDIX C. MATLAB CODE EXCERPT

An excerpt of the MATLAB code used to analyze and graph the data is presented here.

```
mlvdt=.0387;

m1=..626488;

m2=.1.485474;

m3=..644014;


lvdt = main. Data(:,2)*mlvdt;

ustrain1 = main.data(:,3).*m1;

ustrain2 = main.data(:,4).*m2;

ustrain3 = main.data(:,5).*m3;


off_lvdt = mean(lvdt(10:100,:),1);

off_strain1 = mean(ustrain1(10:100,:),1)*m1;

off_strain2 = mean(ustrain2(10:100,:),1)*m2;

off_strain3 = mean(ustrain3(10:100,:),1)*m3;


figure();

%11

plot(cycle,sgolayfilt(strain_z(:,1),5,51));

title('S-G Filtered Strain Gauge 1');

xlabel('Cycle');

ylabel('\mu\epsilon');


figure();

%20
```

```
subplot(2,1,1)
title('Unfiltered Data');
plot(cycle,strain_z(:,1));
xlabel('Cycle');
ylabel('\mu\epsilon');

subplot(2,1,2)
title('S-G Filtered Data');
plot(cycle,sgolayfilt(strain_z(:,1),4,31));
xlabel('Cycle');
ylabel('\mu\epsilon');

sgtitle('Before and After of S-G Filtering Gauge 1');

smax = min(strain_z);
%max tensile strain
disp('Maximum micro.strain per sensor');
disp(smax);
max_v = abs(smax(:,1));
disp(max_v);
f_r = (3*50000*96)/(2*48*12*12);
smax_stress = (max_v)*(1/1000000)*57000*sqrt(3200); % in psi

S=smax_stress/f_r;
```

APPENDIX D. SPREADER BEAM HAND CHECK

This appendix shows the hand calculations to make sure the spreader beam will not fail under load. The calculations also make sure that the overall stiffness is high enough that the full force will be transferred to the slab instead of losing force to the bending of the beam. Using the AISC steel manual, the spreader beam capacities were found. An HSS 8” x 16” x 1/2” has a max moment of 213 kip-ft., which translates to a maximum deflection of .1655 in. Each of the loading’s deflections and moments were calculated to verify the beam would not fail.

Spreader Beam Deflection Check

Moment Diagram from the AISC Manual, 15th edition

Beam Used: HSS 8"x16"x1/2"

$I_x := 679\ in^4$ $\quad L := 6\ ft$

$I_y := 230\ in^4$ $\quad E := 29000\ ksi$

$y_{str} := 5.70\ in$

$y_{weak} := 2.53\ in$

Δ_{max} at point of load = $\frac{PL^3}{48 \cdot EI}$

M.max at point of load = $\frac{PL}{4}$

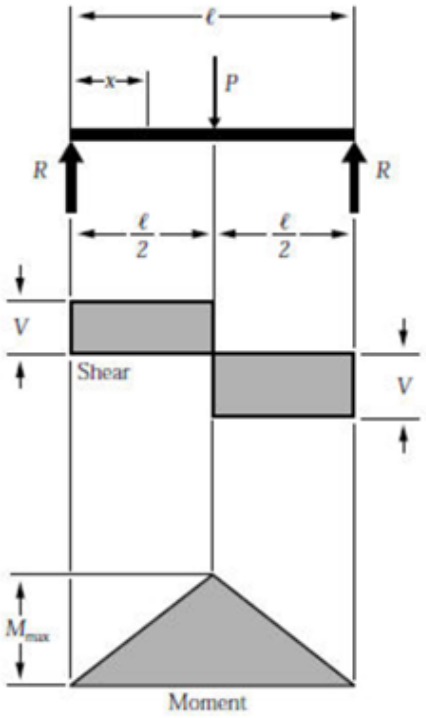

Taking the max bending moment from the AISC manual, it is possible to find the max deflection the beam can handle.

$\Delta_{max} := \frac{P \cdot L^3}{48 \cdot E \cdot I}$ ... M.max *4 = P*L

$\Delta_{max} := \frac{M_{max} \cdot 4 \cdot L^2}{48 \cdot E \cdot I}$

Max Moment of the Spreader Beam

$M_{max} := 213\ kip\ ft$ $(AISC)$

Deflections at each of the loadings

$P_{32} := 32\ kip$ $\quad P_{50} := 50\ kip$ $\quad P_{64} := 64\ kip$

$\Delta_{32} := \frac{P_{32} \cdot L^3}{48 \cdot E \cdot I_y} = 0.0373\ in$

$M_{32} := \frac{P_{32} \cdot L}{4} = 48\ kip\ ft$

$\Delta_{50} := \frac{P_{50} \cdot L^3}{48 \cdot E \cdot I_y} = 0.0583\ in$

$M_{50} := \frac{P_{50} \cdot L}{4} = 75\ kip\ ft$

$\Delta_{64} := \frac{P_{64} \cdot L^3}{48 \cdot E \cdot I_y} = 0.0746\ in$

$M_{64} := \frac{P_{64} \cdot L}{4} = 96\ kip\ ft$

$\Delta_{max} := \frac{M_{max} \cdot 4 \cdot L^2}{48 \cdot E \cdot I_y} = 0.1655\ in$

$\Delta_{max} > \Delta_{64}$ $\quad OK$

$\Delta_{max} > \Delta_{50}$ $\quad OK$

$\Delta_{max} > \Delta_{32}$ $\quad OK$

The beams deflection will provide sufficient stiffness during experimentation

Figure D.11 Hand Check for Spreader Beam

APPENDIX E. FOURIER TRANSFORM EFFECT

The effect of S-G filtering over a cyclic analysis method like a Fourier transform is of concern during the analysis of the data gathered from this research. As previously proven, the overall differences in this instance are small enough that either method would be effective. Savitzky-Golay filtering is best used to reduce noise and to better visualize data (Press et al., 1990). Because raw data were used for comparisons and conclusion determination, small percentage differences did not matter. Shown below in Figure E.1 is an example of the filtered data. In Figure E.2 a figure of the Fourier transformed data is shown.

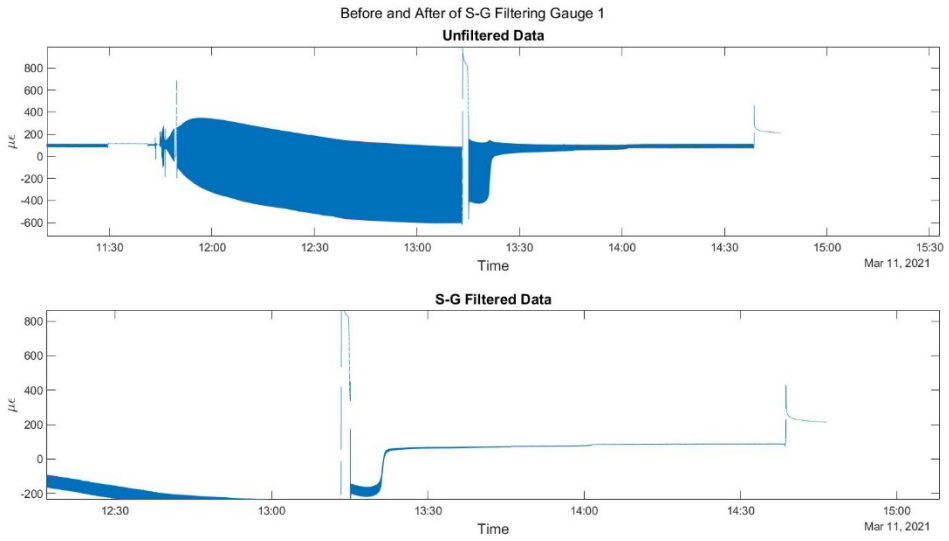

Figure E.1 S-G Filtering

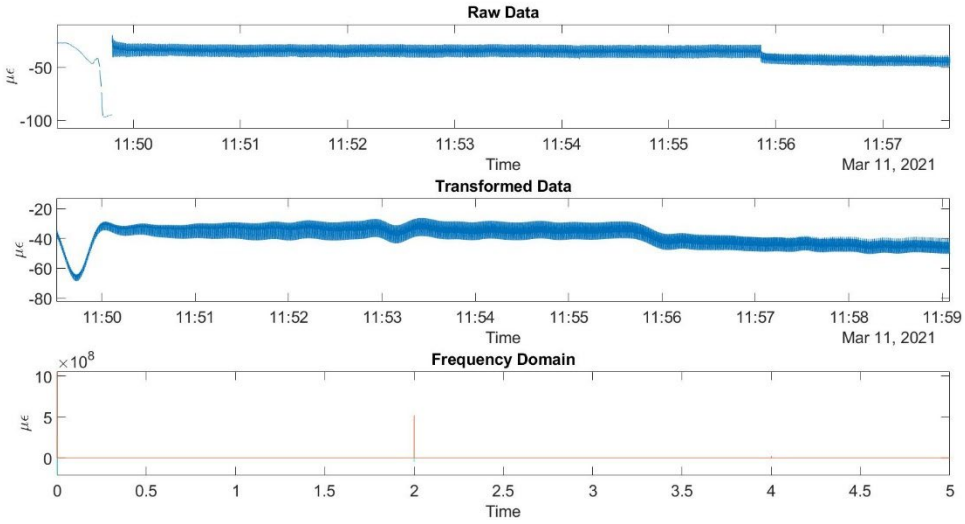

Figure E.2 Effect of the Fourier Transform

As can be seen, the Fourier transform confirms in the frequency domain that 2 Hz is the predominant force behind the experiments. The 0 Hz can be inferred to be machine interference, most likely from the DC output for the sensors. MATLAB's built-in function FFT were used for the graphing. Note that the raw data and the transformed data after the Fourier transform are nearly identical. The S-G filtered data at the same time also show a similar value, with analysis showing up to a 5% difference.

APPENDIX F. COMPLETE COMPENDIUM OF INTERNAL STRAIN GAUGE DATA

Due to the large amount of data gathered, it is prudent to present only a selected set of graphs in the paper, as several gauges had footing failures and cannot be considered in the final design criteria. All graph data will be presented here in the following order: raw, filtered, and cyclic trend.

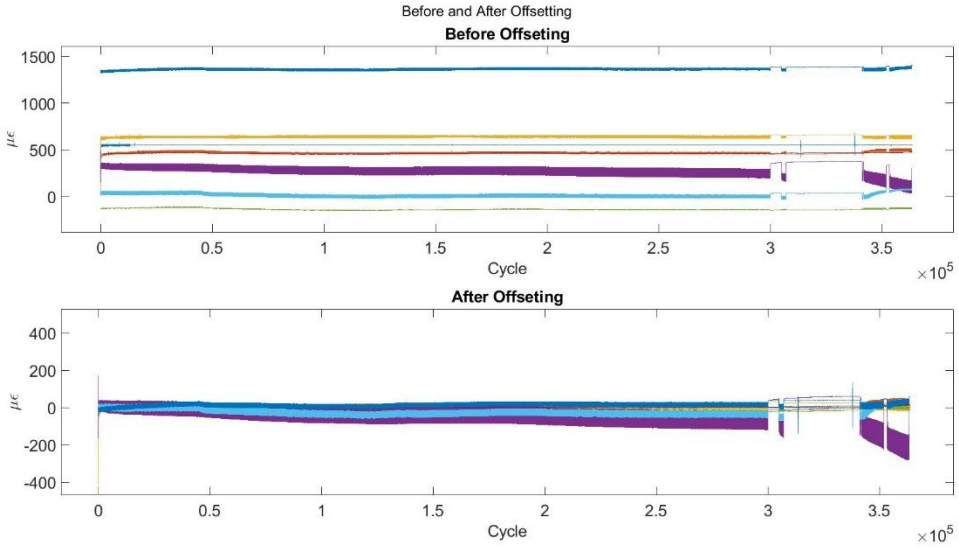

Figure F.1 Steel Raw Data and Offset

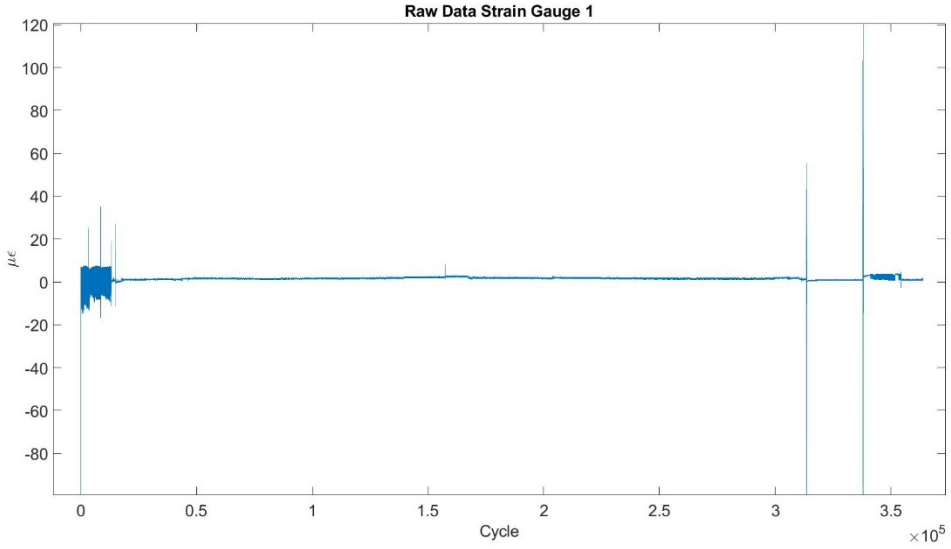

Figure F.2 Steel Gauge 1 – Raw

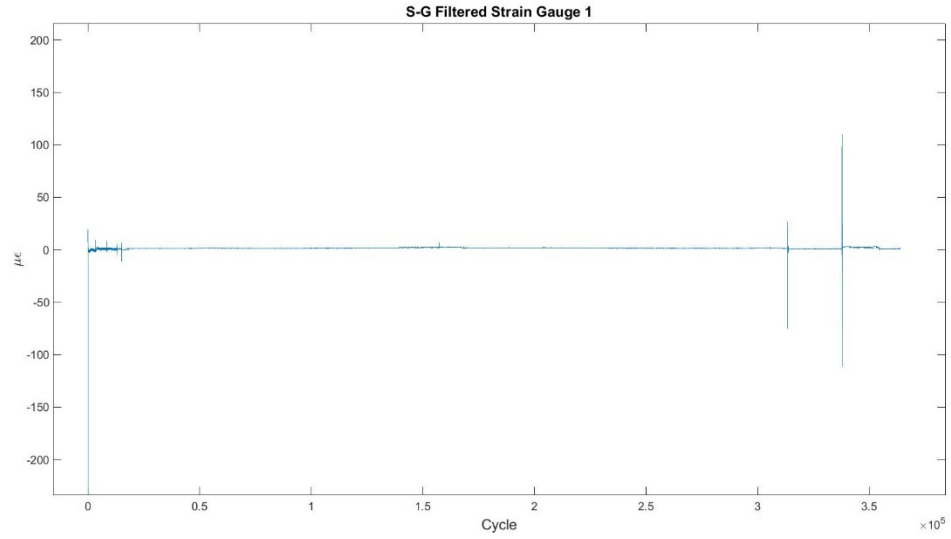

Figure F.3 Steel Gauge 1 – Filtered

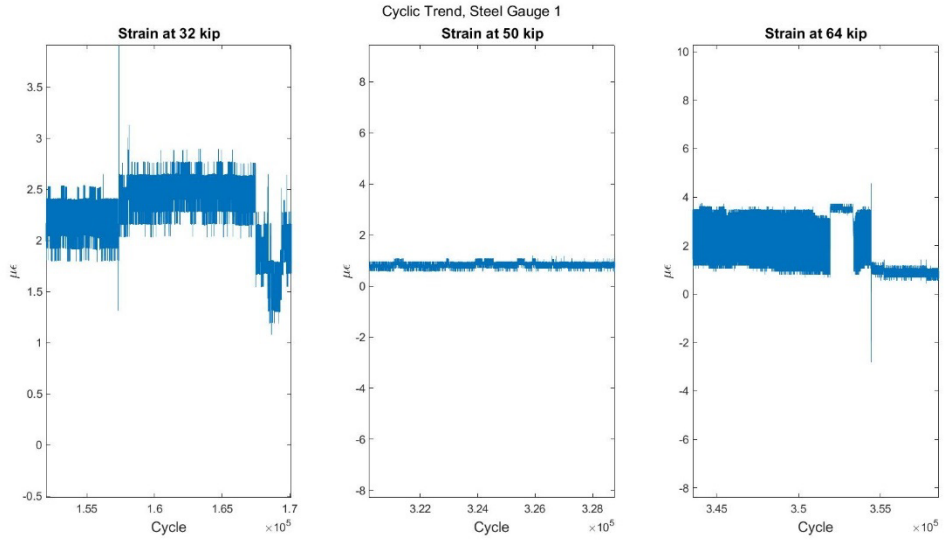

Figure F.4 Steel Gauge 1. Cyclic Trend

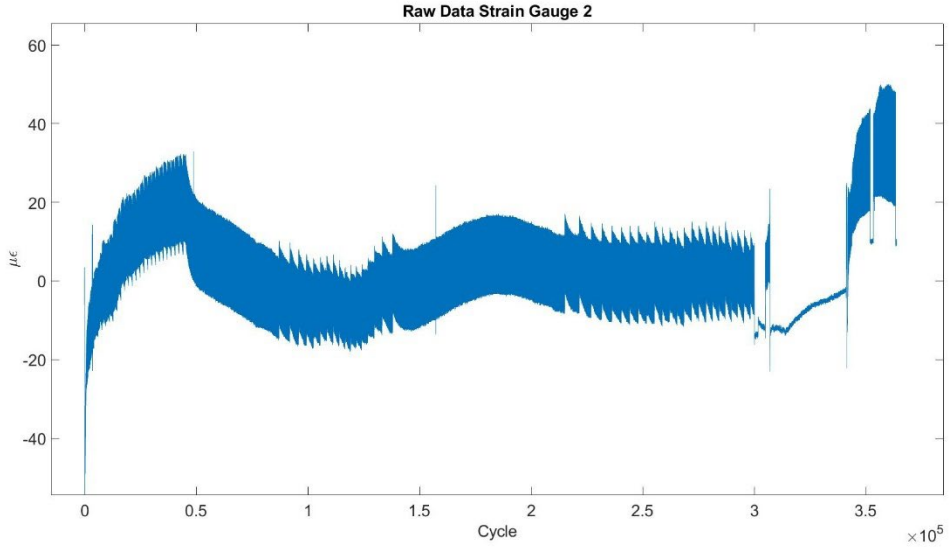

Figure F.5 Steel Gauge 2. Raw

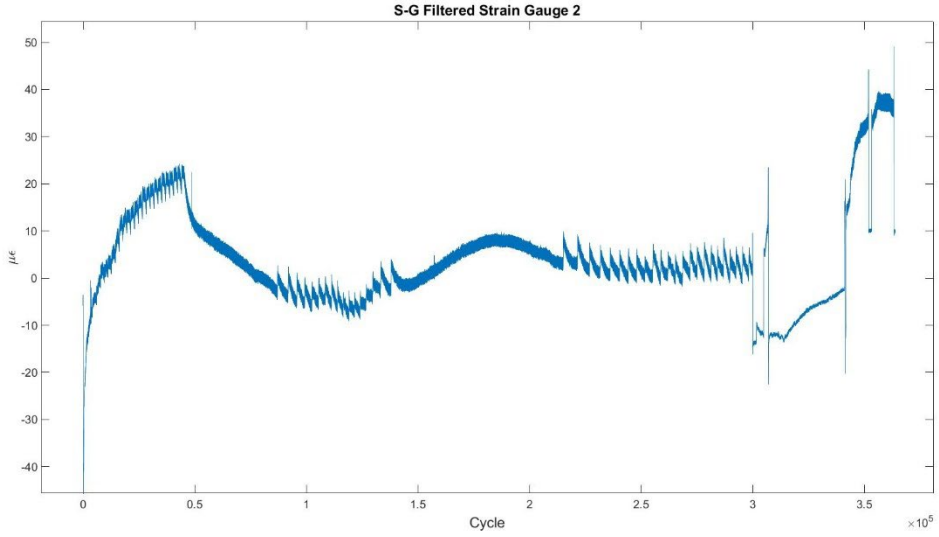

Figure F.6 Steel Gauge 2. Filtered

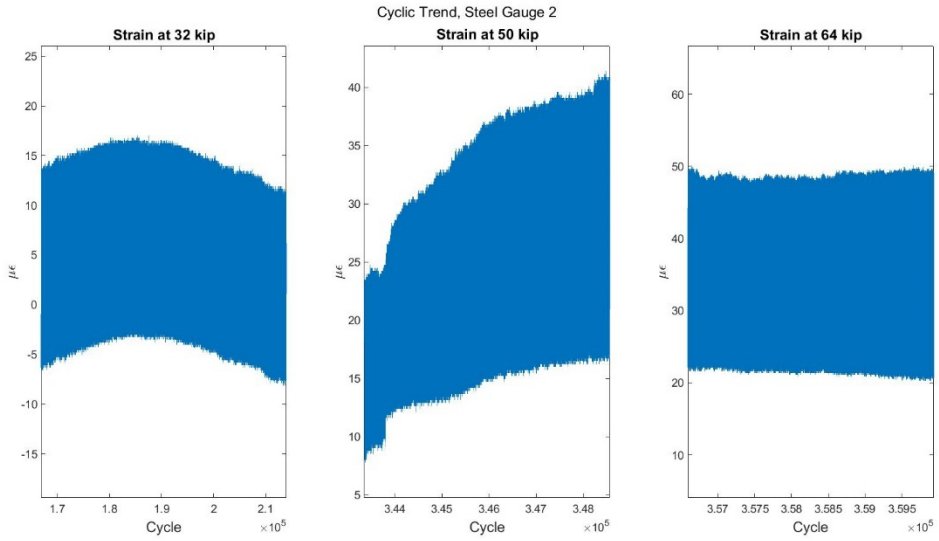

Figure F.7 Steel Gauge 2. Cyclic Trend

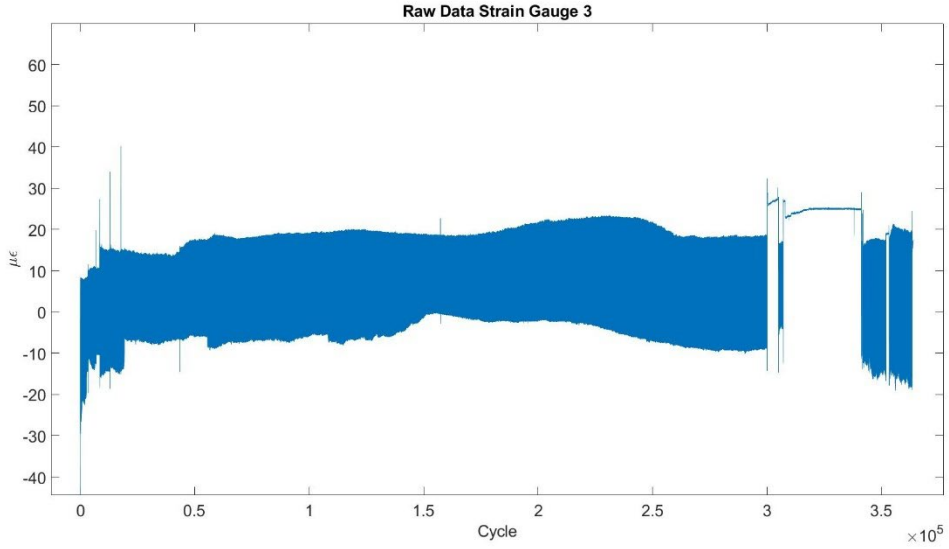

Figure F.8 Steel Gauge 3 – Raw

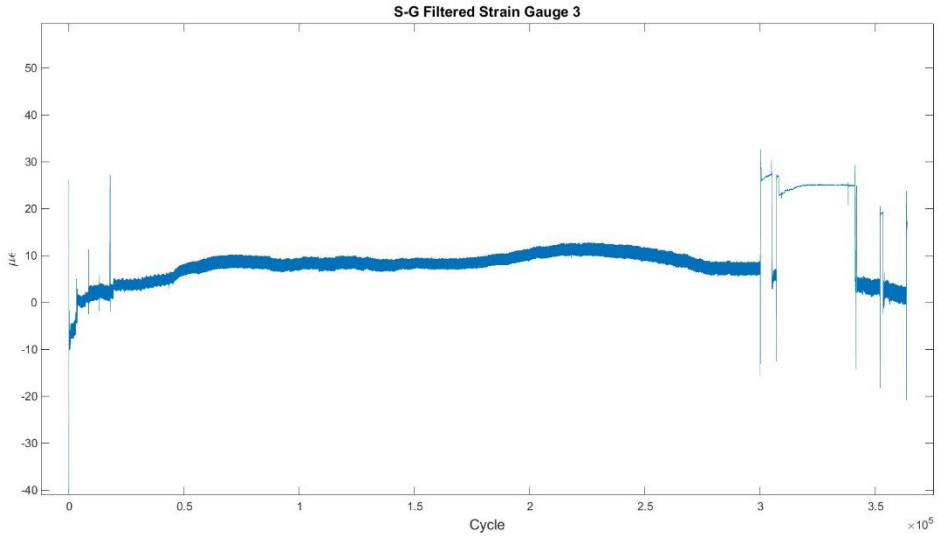

Figure F.9 Steel Gauge 3 – Filtered

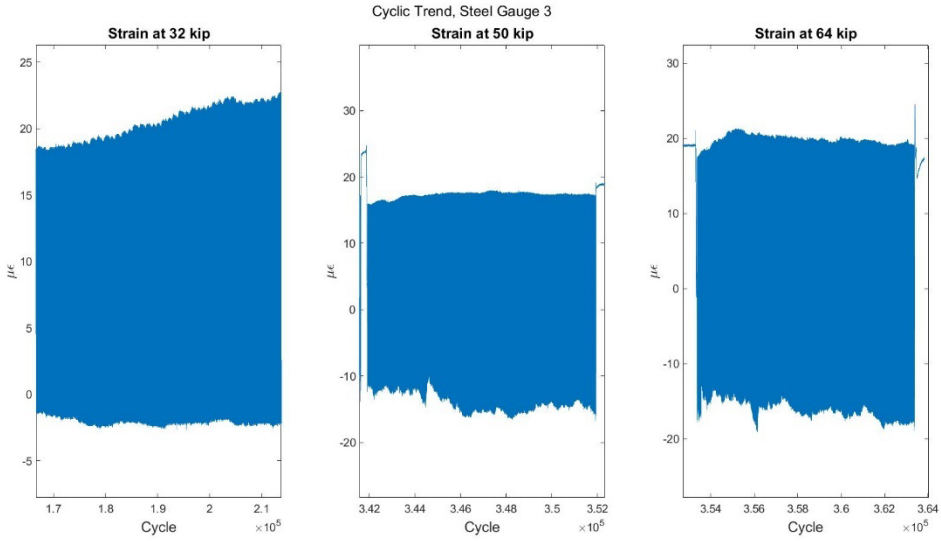

Figure F.10 Steel Gauge 3 – Cyclic Trend

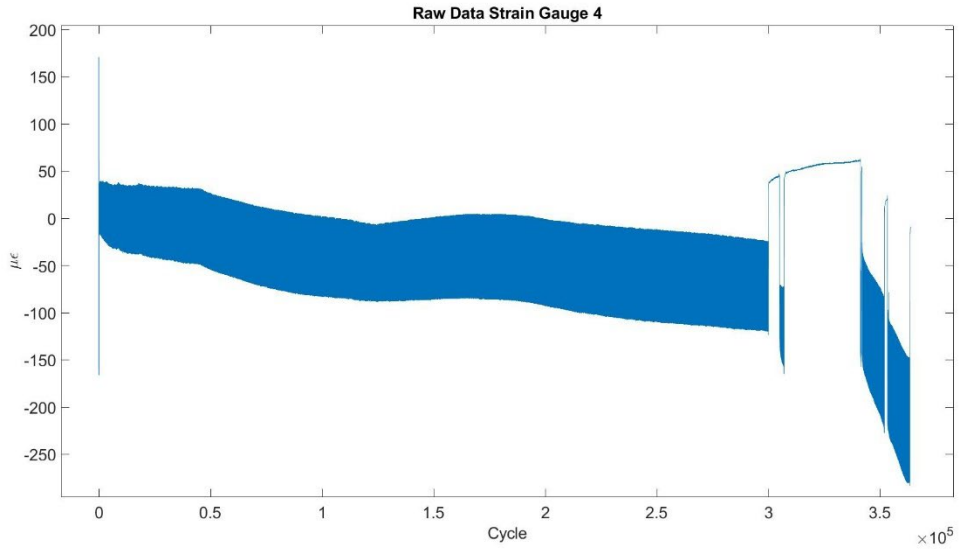

Figure F.11 Steel Gauge 4 – Raw

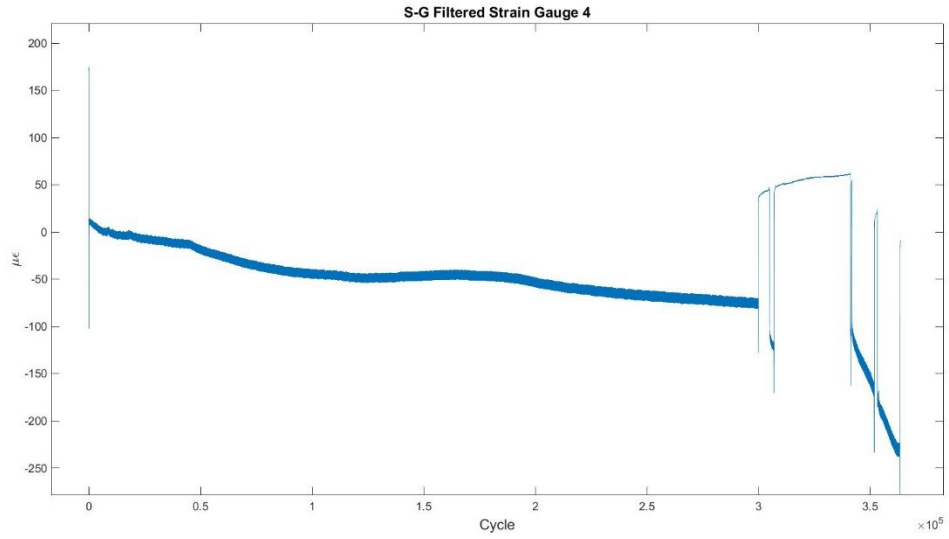

Figure F.12 Steel Gauge 4 – Filtered

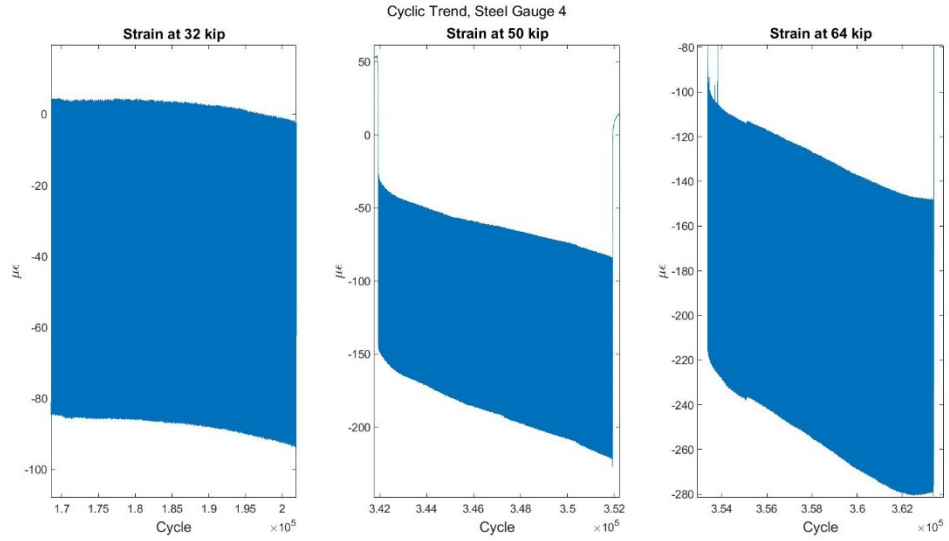

Figure F.13 Steel Gauge 4 – Cyclic Trend

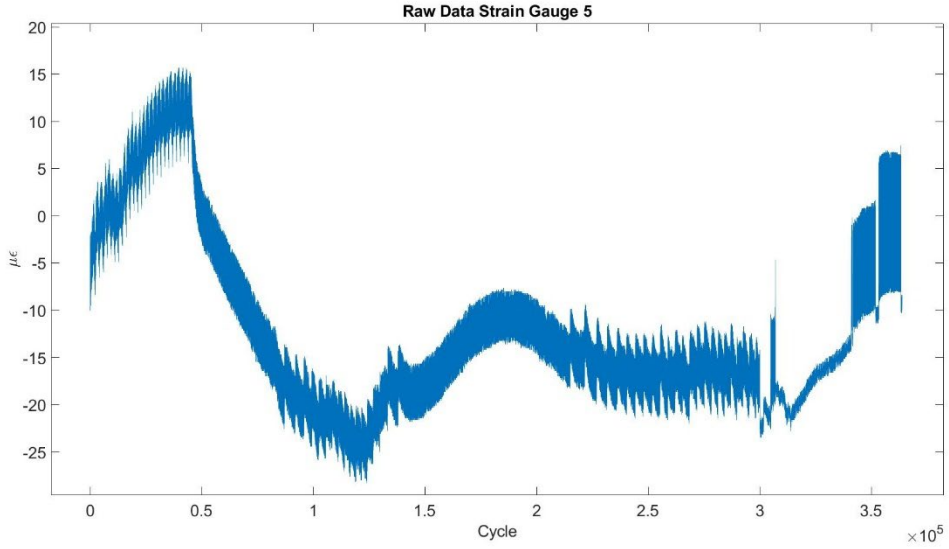

Figure F.14 Steel Gauge 5 – Raw

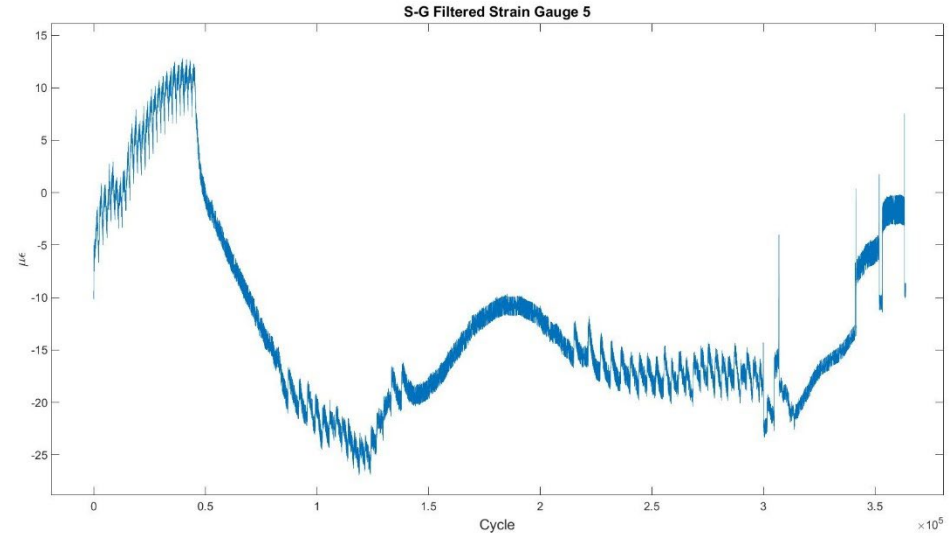

Figure F.15 Steel Gauge 5 – Filtered

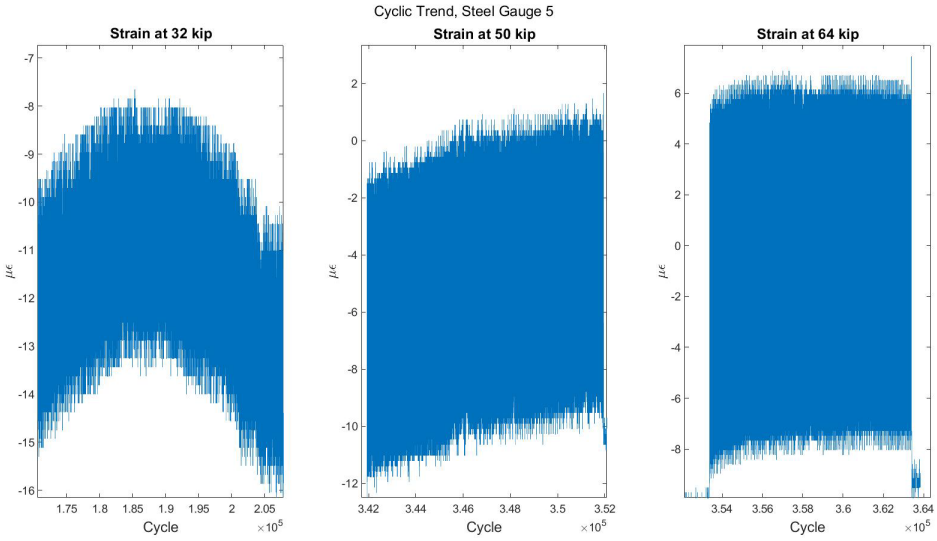

Figure F.16 Steel Gauge 5 – Cyclic Trend

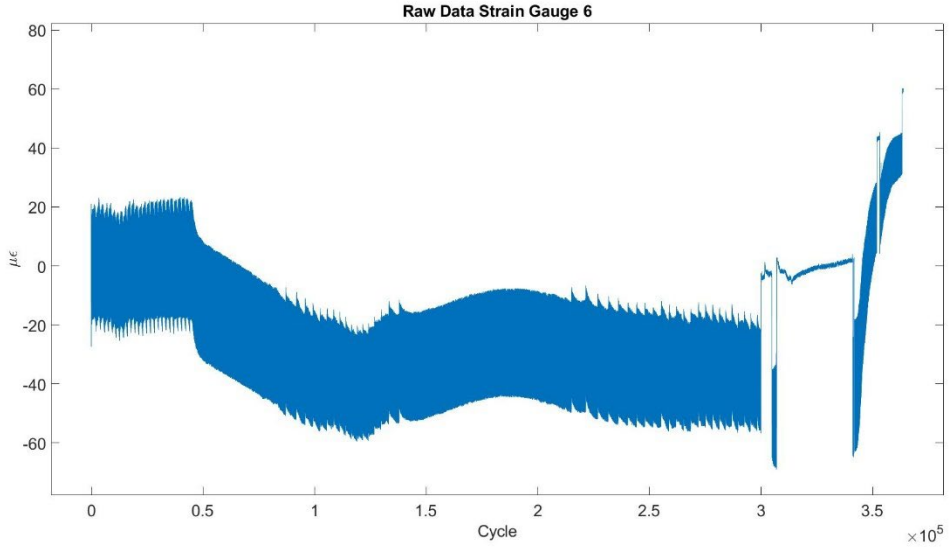

Figure F.17 Steel Gauge 6 – Raw

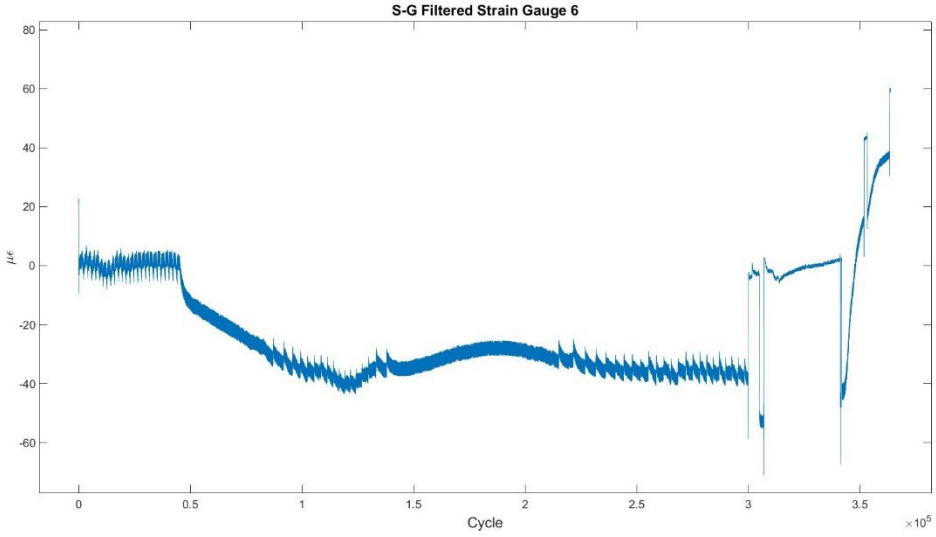

Figure F.18 Steel Gauge

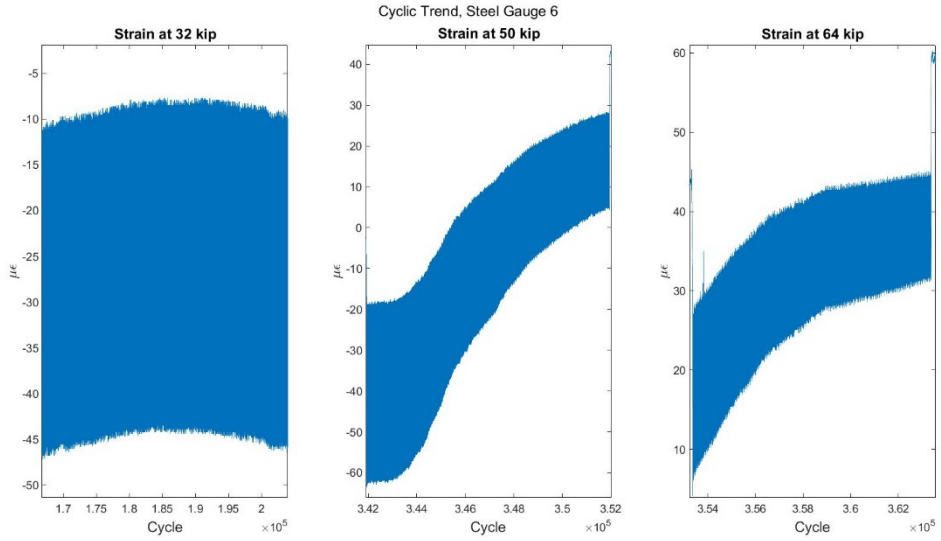

6 – Filtered

Figure F.19 Steel Gauge 6 . Cyclic – Trend

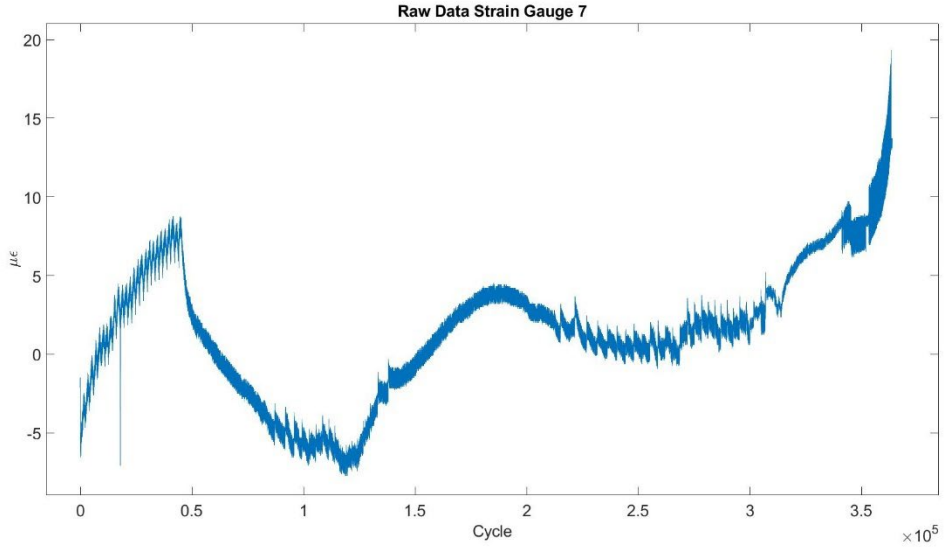

Figure F.20 Steel Gauge 7 – Raw

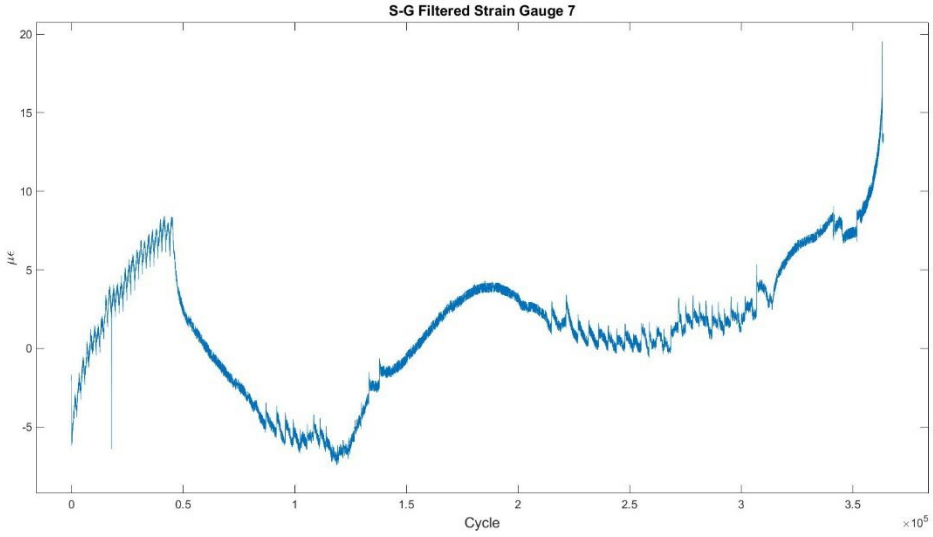

Figure F.21 Steel Gauge 8 – Filtered

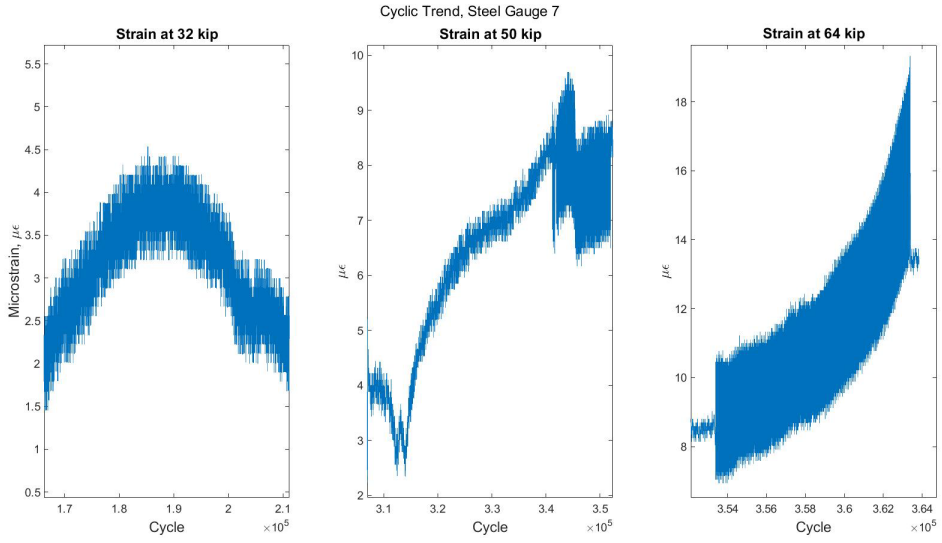

Figure F.22 Steel Gauge 7 – Cyclic Trend

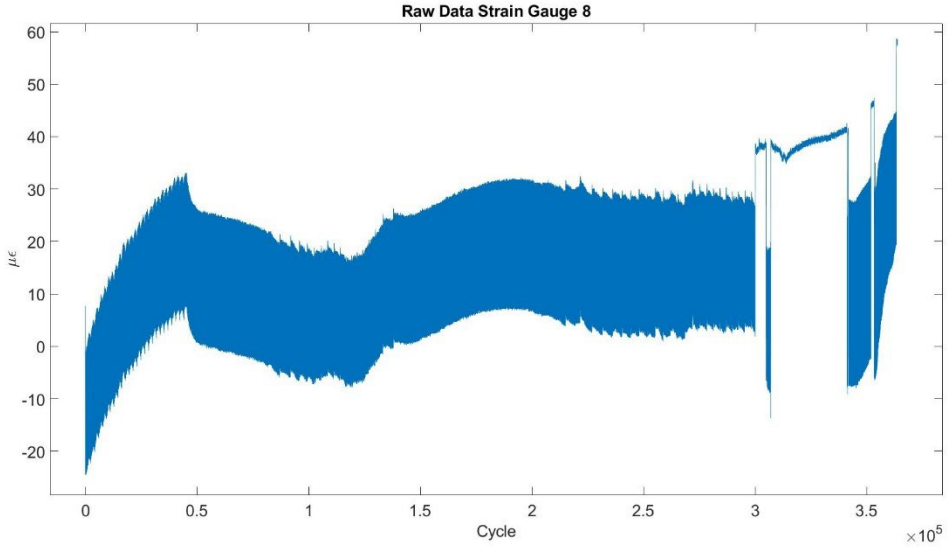

Figure F.23 Steel Gauge 8 – Raw

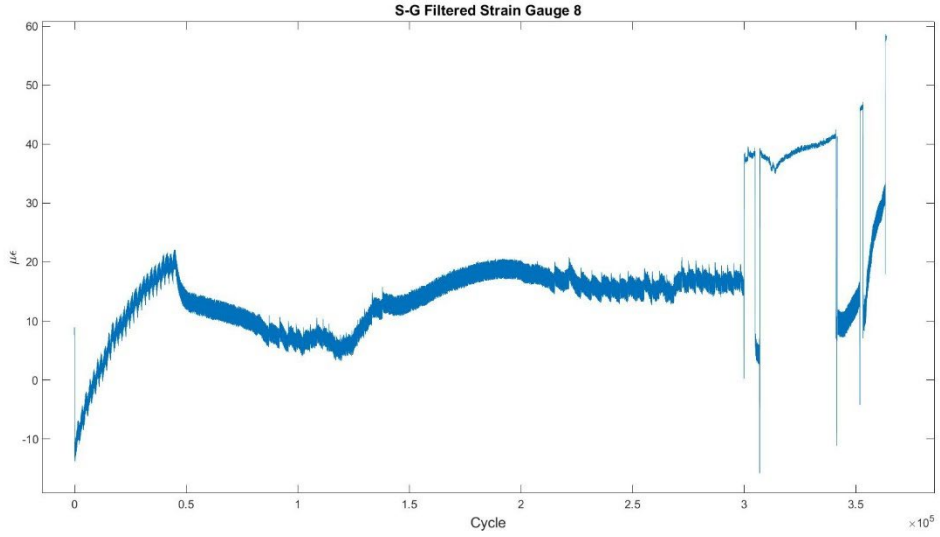

Figure F.24 Steel Gauge 8 – Filtered

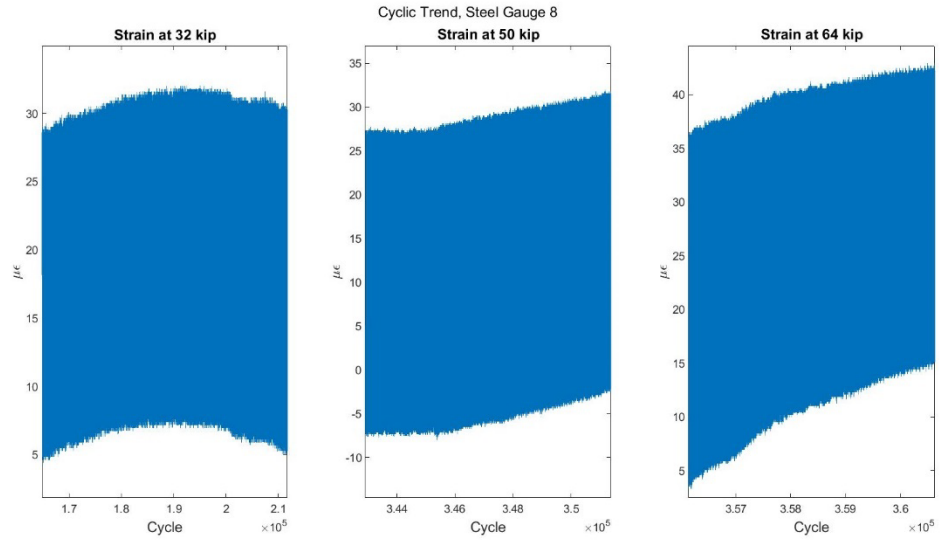

Figure F.25 Steel Gauge 8 – Cyclic Trend

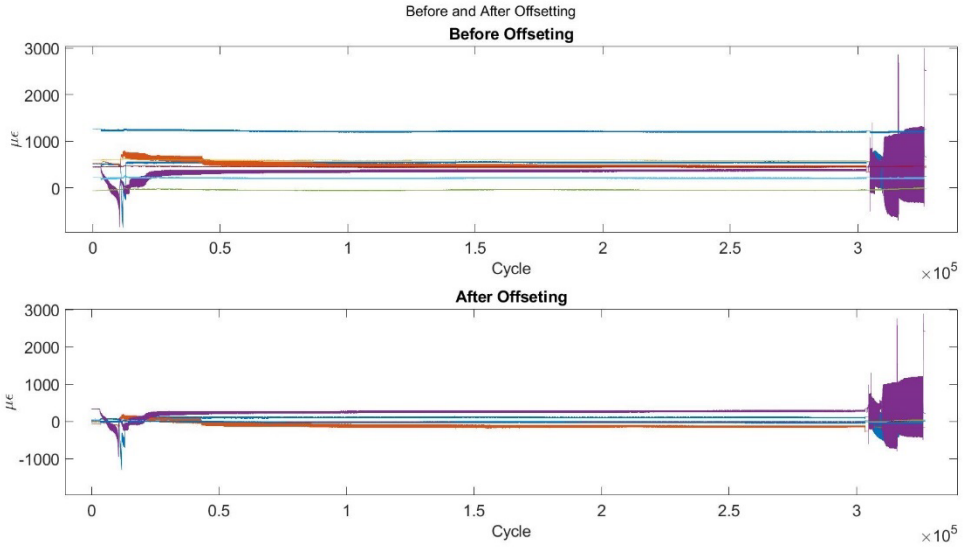

Figure F.26 GFRP Offsetting

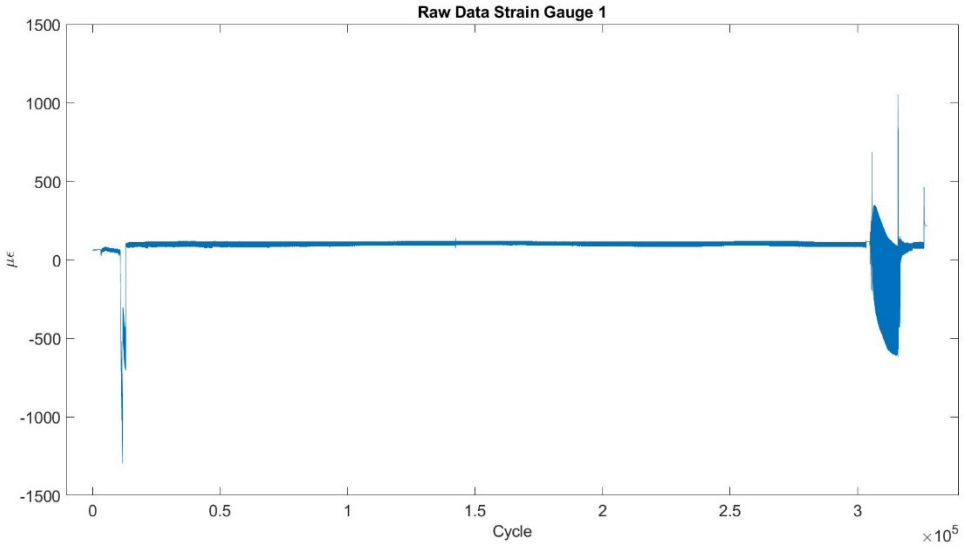

Figure F.27 GFRP Gauge 1 – Raw

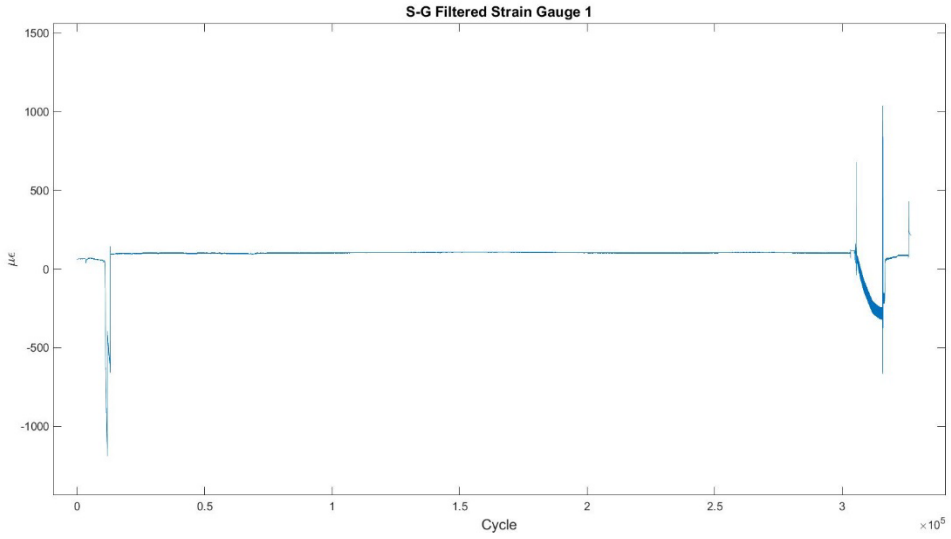

Figure F.28 GFRP Gauge 1 – Filtered

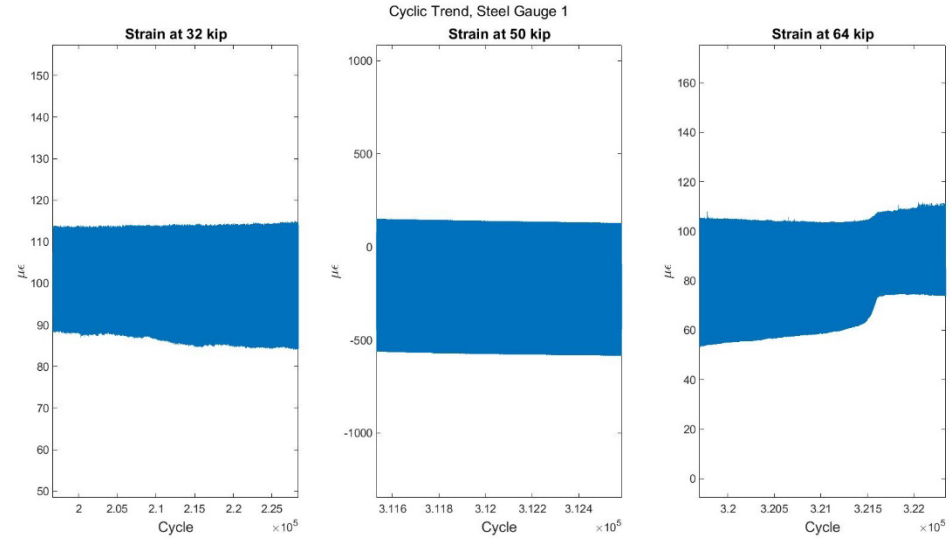

Figure F.29 GFRP Gauge 1 – Cyclic Trend

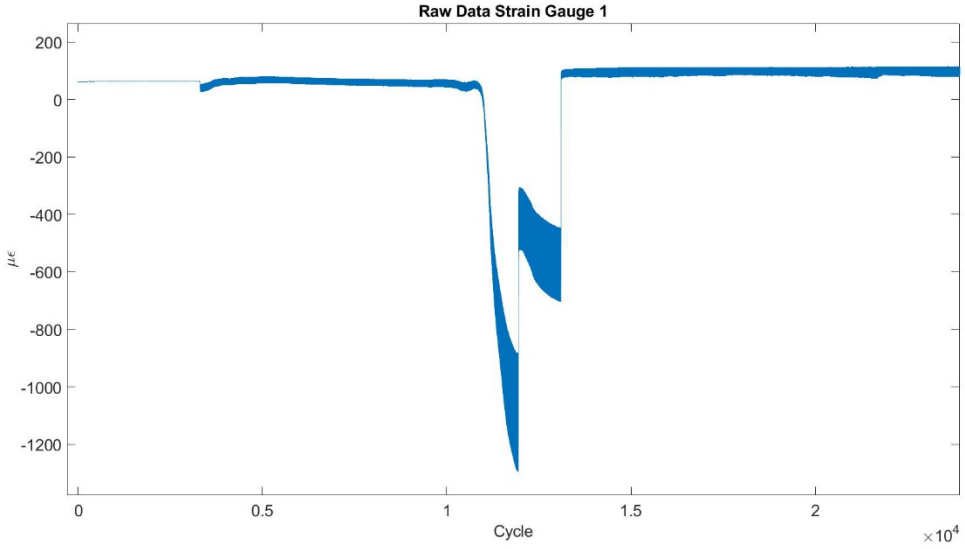

Figure F.30 GFRP Gauge 1 – Closeup

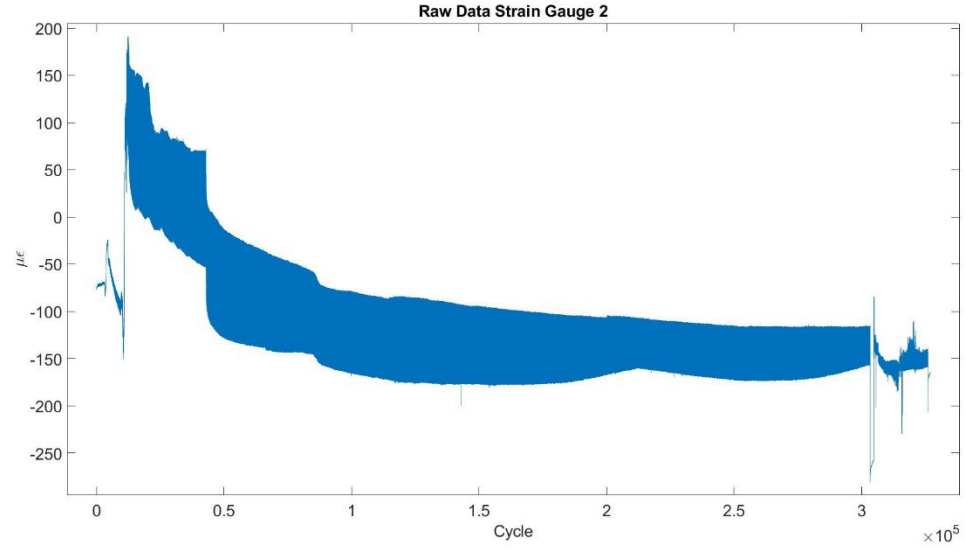

Figure F.31 GFRP Gauge 2 – Raw

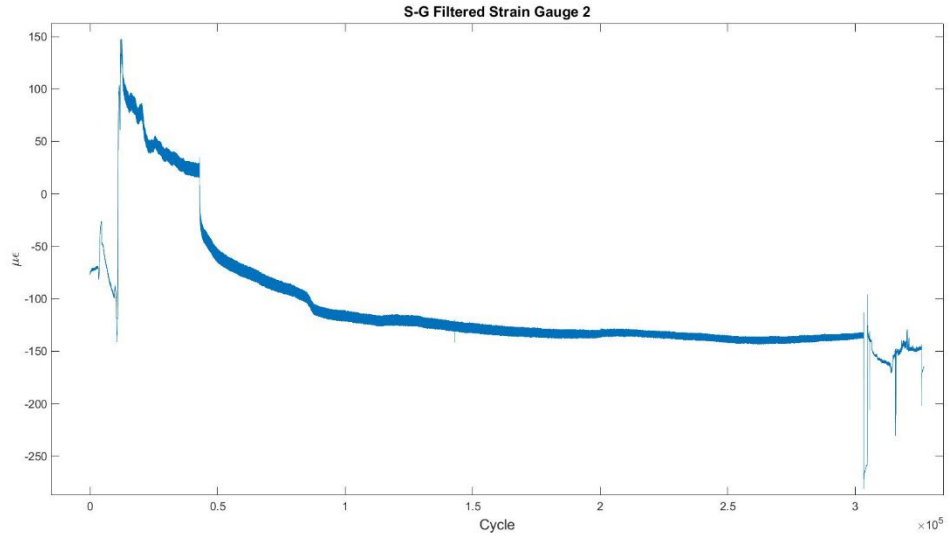

Figure F.32 GFRP Gauge 2 – Filtered

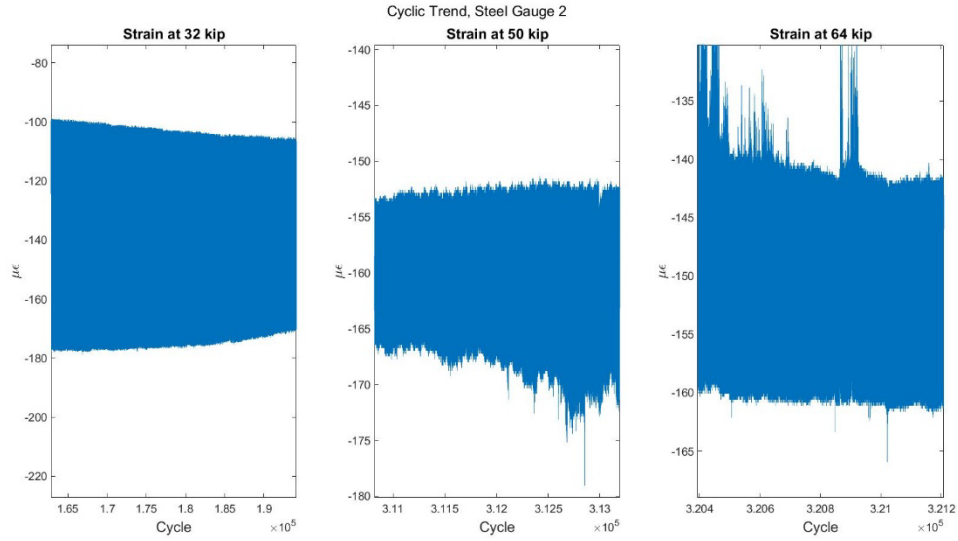

Figure F.33 GFRP Gauge 2 – Cyclic Trend

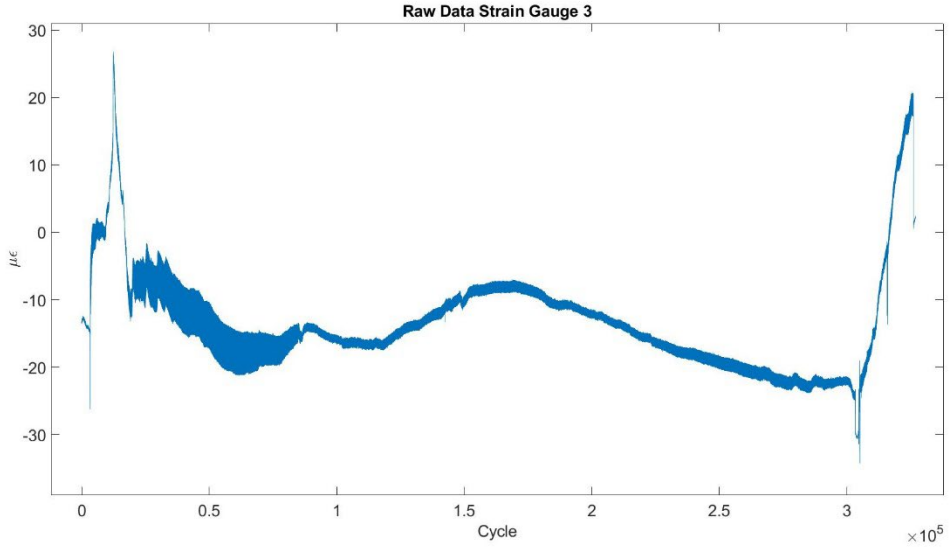

Figure F.34 GFRP Gauge 3 – Raw

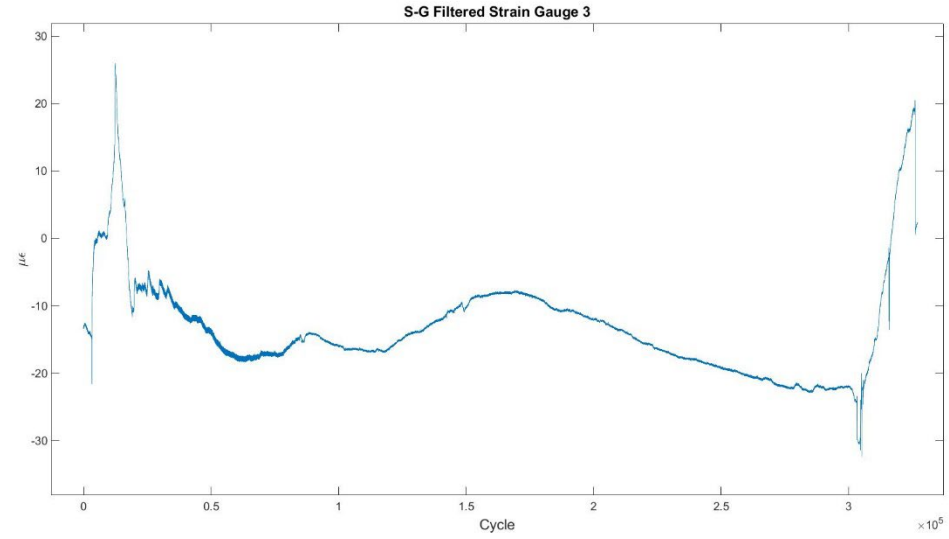

Figure F.35 GFRP Gauge 3 – Filtered

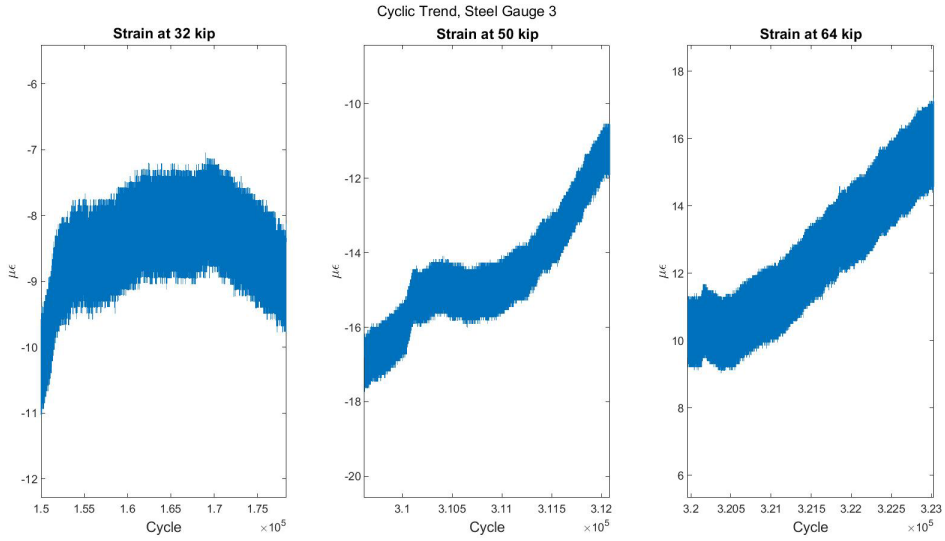

Figure F.36 GFRP Gauge 3 – Cyclic Trend

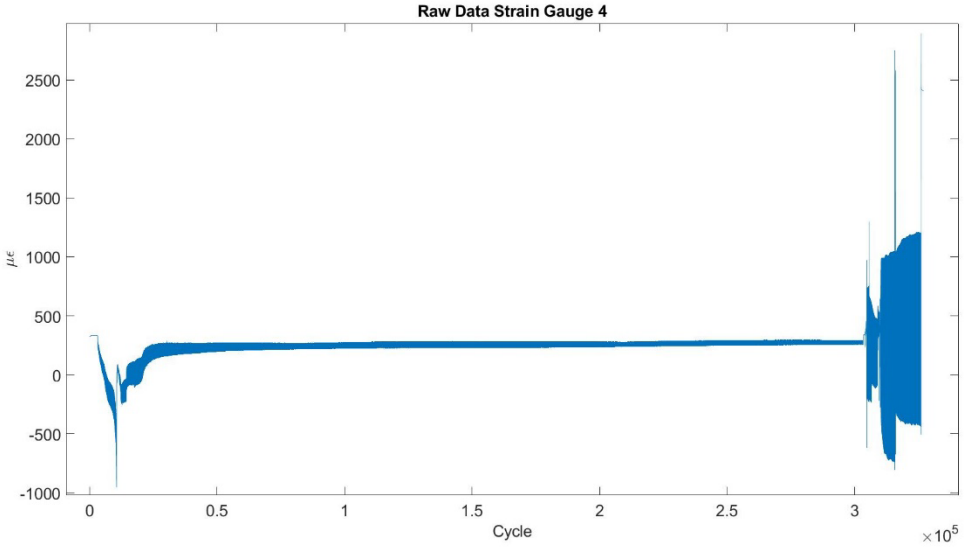

Figure F.37 GFRP Gauge 4 – Raw

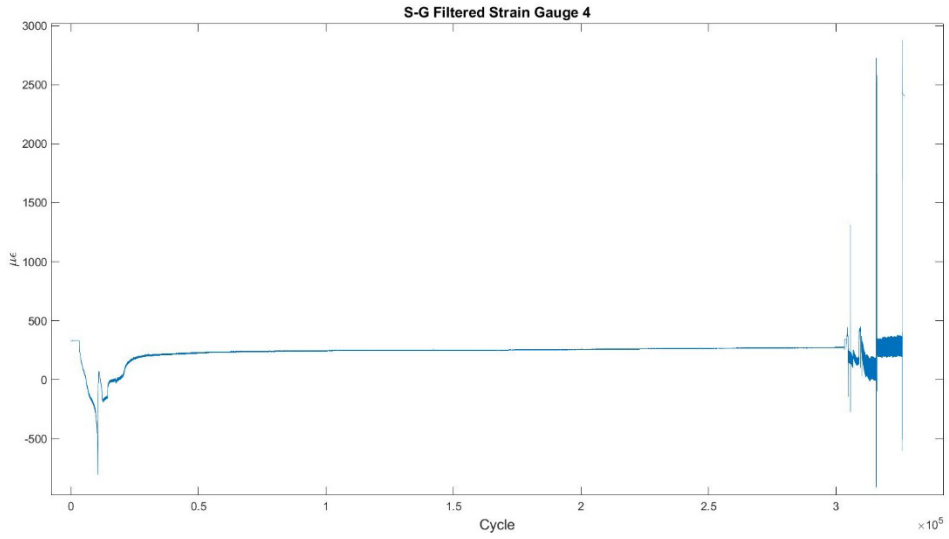

Figure F.38 GFRP Gauge 4 – Filtered

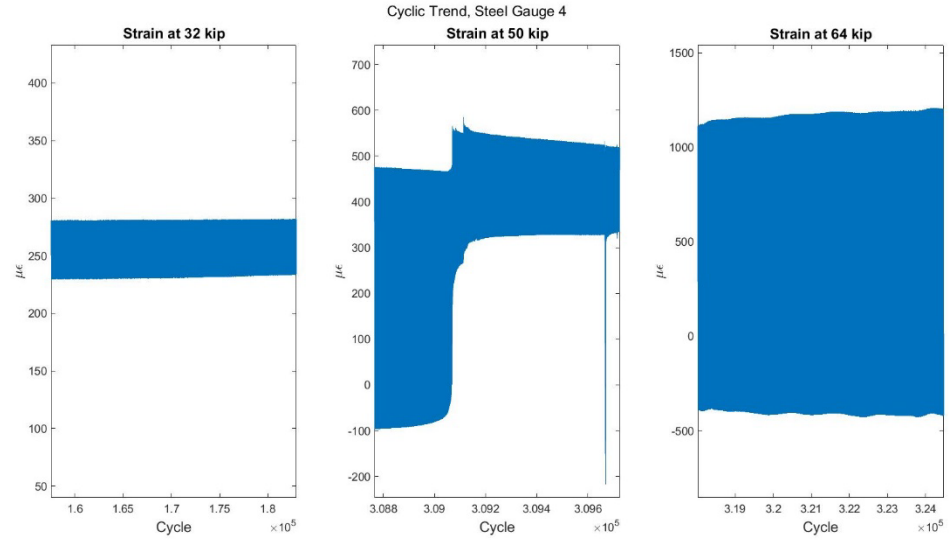

Figure F.39 GFRP Gauge 4 – Cyclic Trend

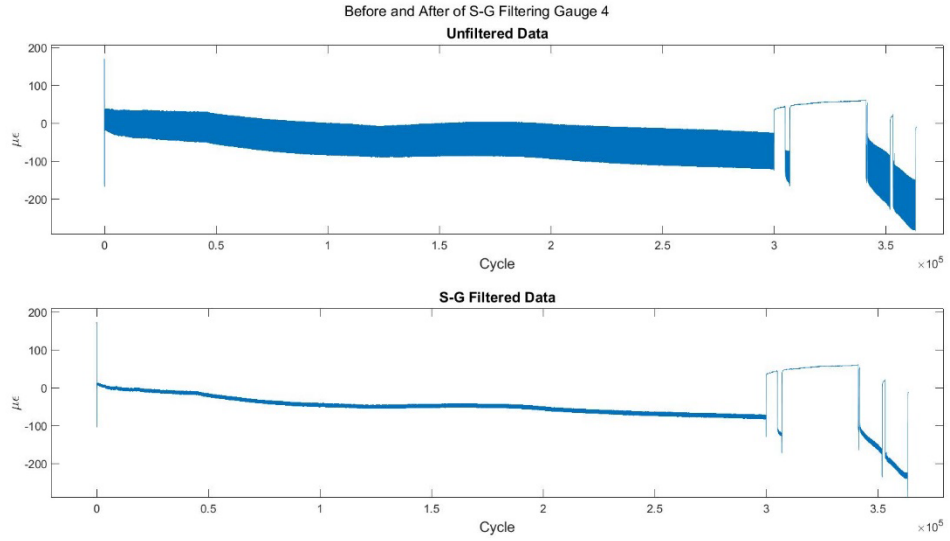

Figure F.40 GFRP Gauge 4 – Overview

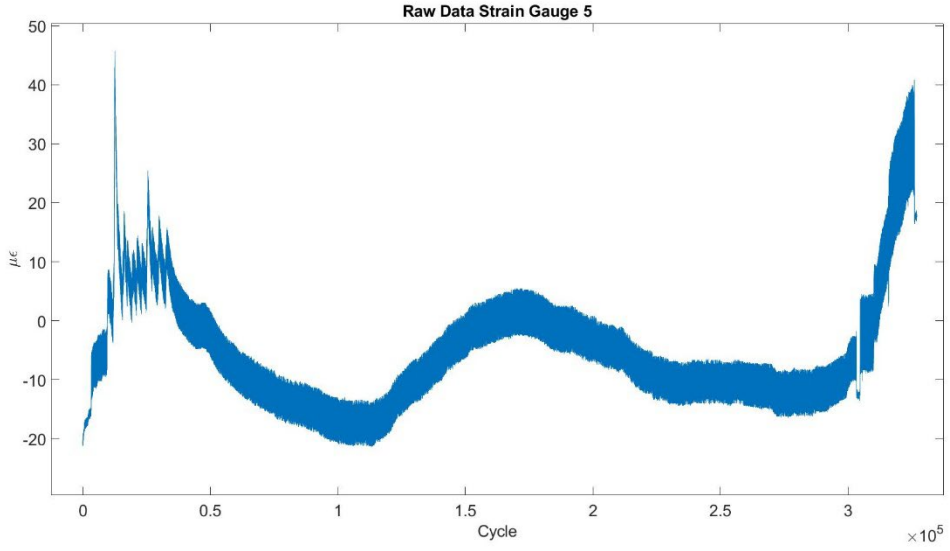

Figure F.41 GFRP Gauge 5 – Raw

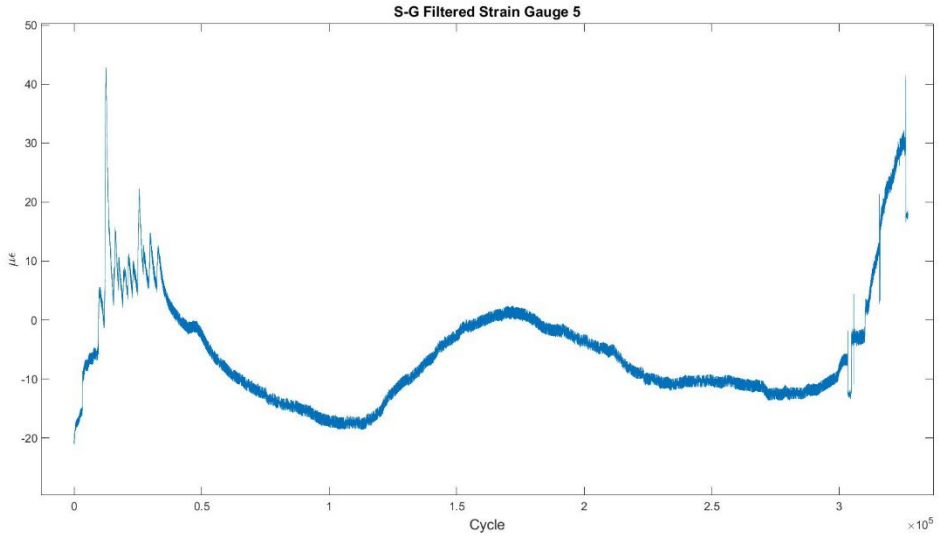

Figure F.42 GFRP Gauge 5 – Filtered

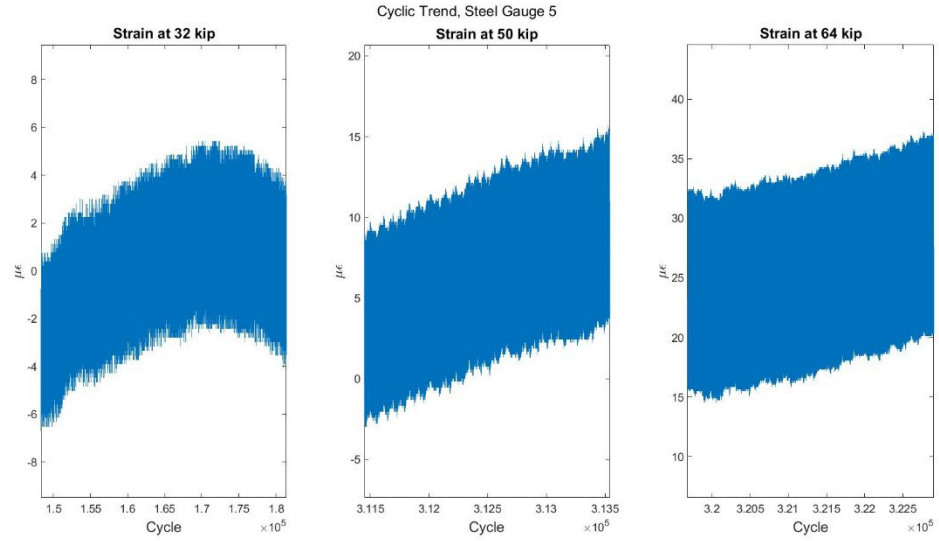

Figure F.43 GFRP Gauge 5 – Cyclic Trend

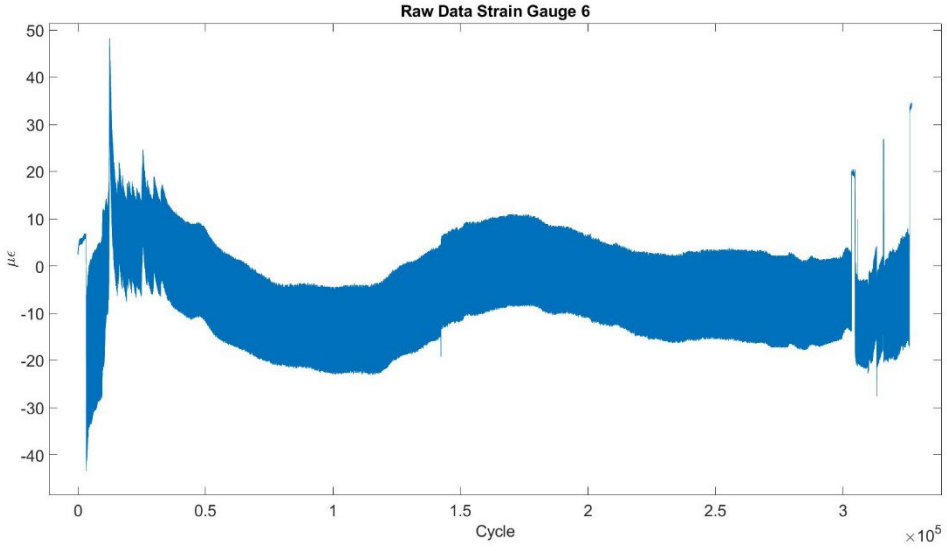

Figure F.44 GFRP Gauge 6 – Raw

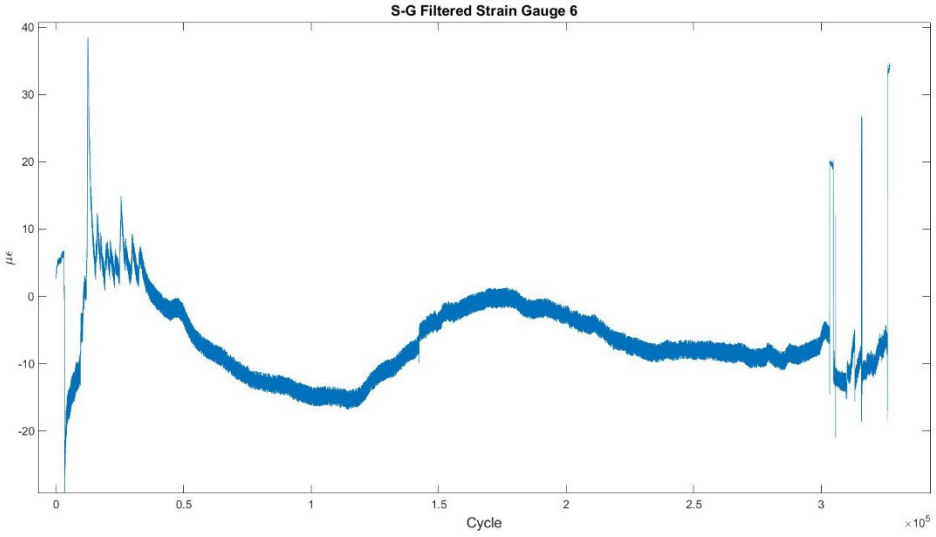

Figure F.45 GFRP Gauge 6 – Filtered

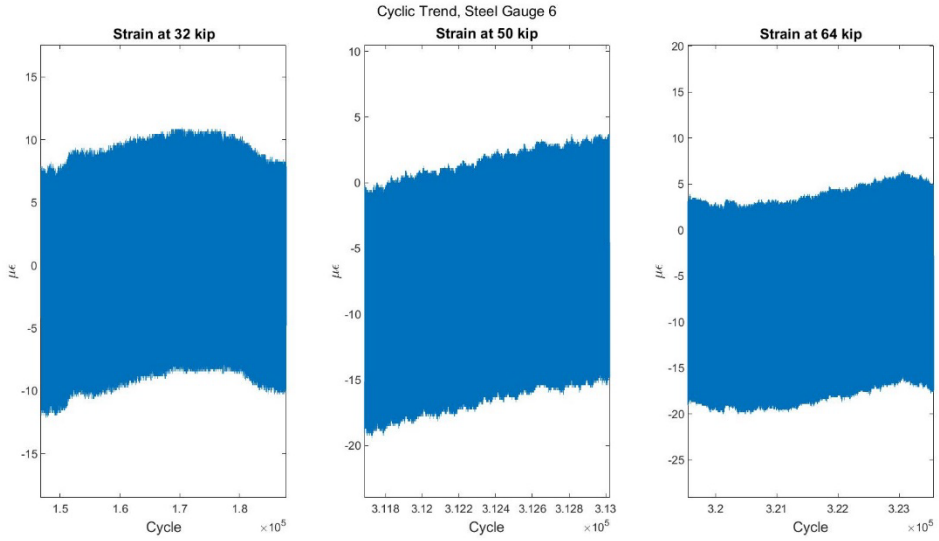

Figure F.46 GFRP Gauge 6 – Cyclic Trend

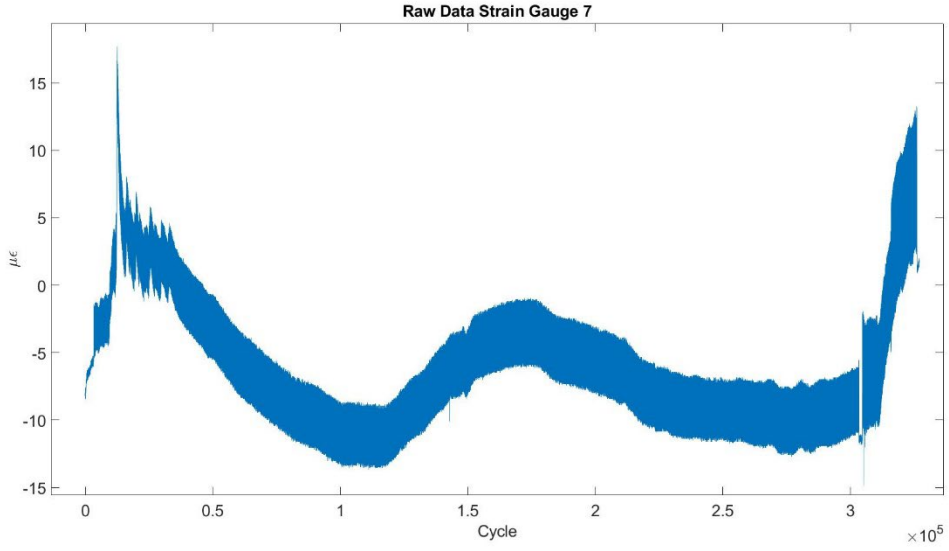

Figure F.47 GFRP Gauge 7 – Raw

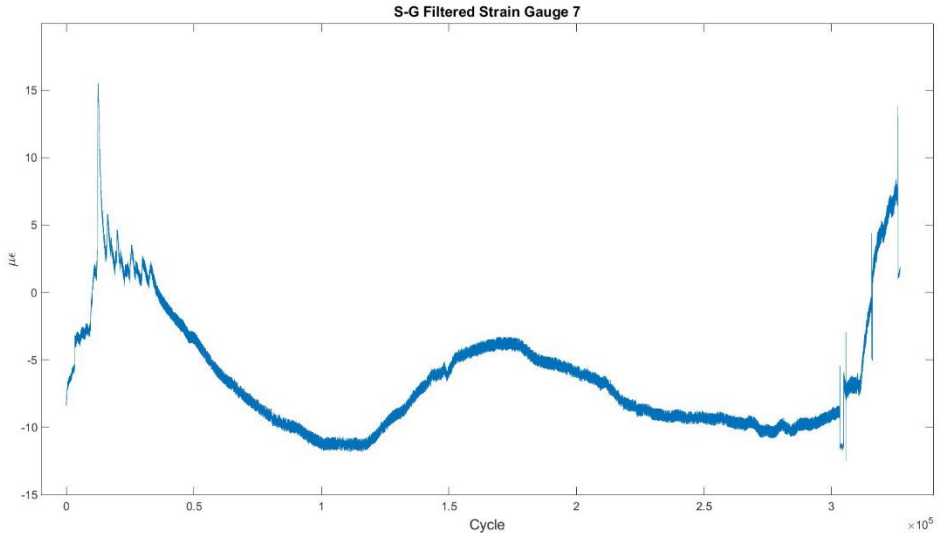

Figure F.48 GFRP Gauge 7 – Filtered

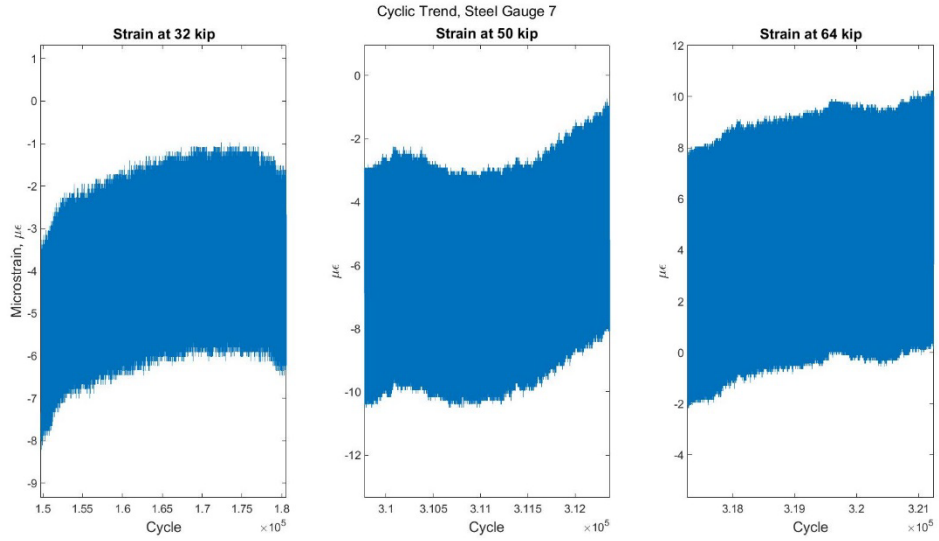

Figure F.49 GFRP Gauge 7 – Cyclic Trend

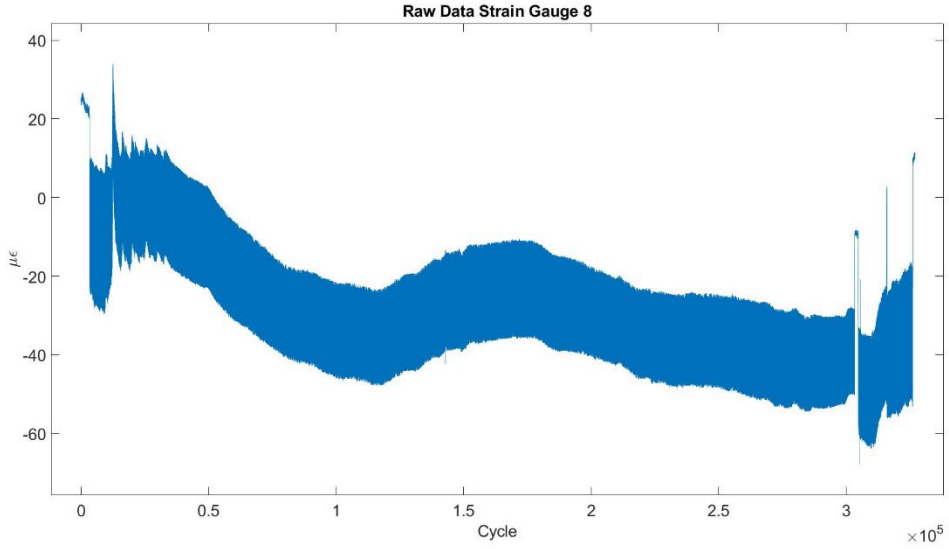

Figure F.50 GFRP Gauge 8 – Raw

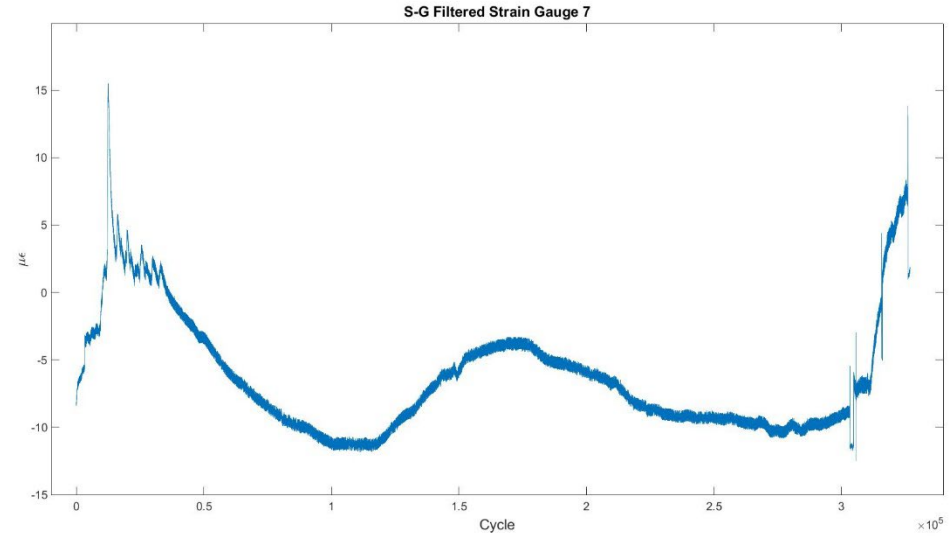

Figure F.51 GFRP Gauge 8 – Filtered

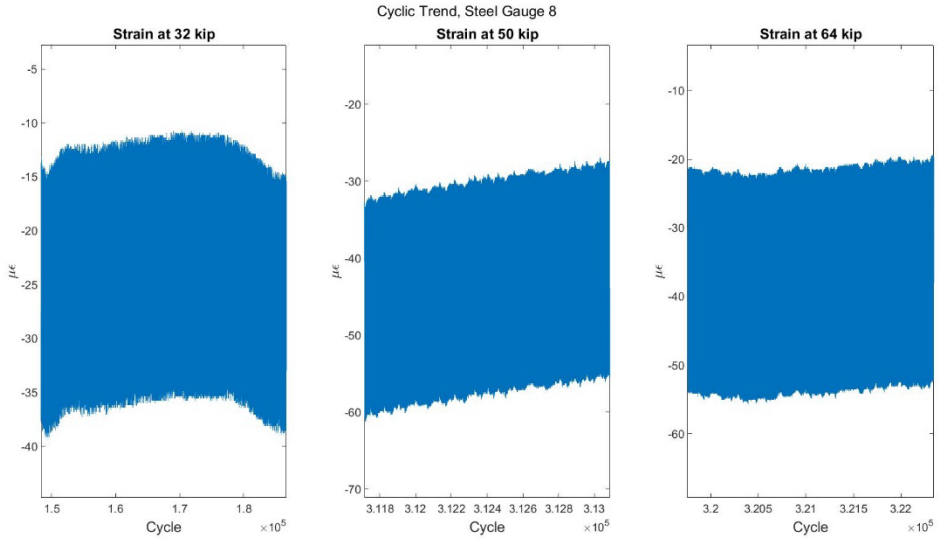

Figure F.52 GFRP Gauge 8 – Cyclic Trend

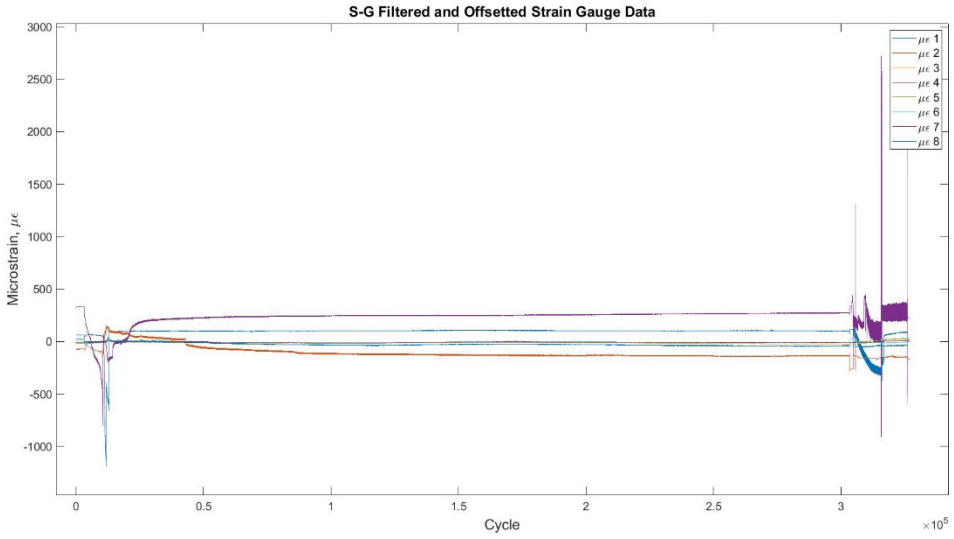

Figure F.53 GFRP Gauges Offset

APPENDIX G. HAND CALCULATION FOR STRENGTH OF CONCRETE AT TESTING

$L := 6\ ft = 72\ in$ $\sigma_{tested} := 3000$

$b := 4\ ft = 48\ in$

$d := 1\ ft = 12\ in$

$F_{steel} := 43730\ lb$ Strength to break the GFRP slab

ACI 3-point bending tests have shown to give a 15% higher Modulus of Rupture than corresponding 4-point bending tests. Therefore, to more accurately describe the estimation of compressive strength, the average of both tests was taken after decreasing the modulus of rupture by the maximum amount. This may give a conservative value, but will be the closest approximation given the available values.

$$\sigma_{MORsteel} := \frac{3 \cdot F_{steel} \cdot L}{2 \cdot b \cdot d^2} = 683.2812\ \frac{lb}{in^2}$$

Max Possible Concrete Strength

$$\sigma_{csteel} := \left(\frac{683.2812}{2.3}\right)^{\frac{3}{2}} = 5120.442\ \frac{lb}{in^2} \qquad increase := \frac{\left(5120.442 - \sigma_{tested}\right)}{\sigma_{tested}} \cdot 100 = 70.6814\ \%$$

Minimum Possible Concrete Strength

$$\sigma_{csteel} := \left(\frac{683.2812 \cdot .85}{2.3}\right)^{\frac{3}{2}} = 4012.6921\ \frac{lb}{in^2} \qquad increase := \frac{\left(4012.69 - \sigma_{tested}\right)}{\sigma_{tested}} \cdot 100 = 33.7563\ \%$$

Median Possible Concrete Strength

$$\sigma := \frac{\left(683.2812\right) + \left(683.2812 \cdot .85\right)}{2} = 632.0351$$

$$\sigma_{csteel} := \left(\frac{632.04}{2.3}\right)^{\frac{3}{2}} = 4555.3851\ \frac{lb}{in^2} \qquad increase := \frac{\left(4555.39 - \sigma_{tested}\right)}{\sigma_{tested}} \cdot 100 = 51.8463\ \%$$

$F_{GFRP} := 51475\ lb$ Strength to break the GFRP slab

$$\sigma_{MORGFRP} := \frac{3 \cdot F_{GFRP} \cdot L}{2 \cdot b \cdot d^2} = 804.2969\ \frac{lb}{in^2}$$

Max Possible Concrete Strength

$$\sigma_{cGFRP} := \left(\frac{804.2969}{2.3}\right)^{\frac{3}{2}} = 6539.3237\ \frac{lb}{in^2} \qquad increase := \frac{\left(6539.3237 - \sigma_{tested}\right)}{\sigma_{tested}} \cdot 100 = 117.9775\ \%$$

Minimum Possible Concrete Strength

$$\sigma_{cGFRP} := \left(\frac{804.2969 \cdot .85}{2.3}\right)^{\frac{3}{2}} = 5124.6148\ \frac{lb}{in^2} \qquad increase := \frac{\left(5124.6148 - \sigma_{tested}\right)}{\sigma_{tested}} \cdot 100 = 70.8205\ \%$$

Median Possible Concrete Strength

$$\sigma := \frac{(804.2969) + (804.2969 \cdot .85)}{2} = 743.9746 \quad \frac{lb}{in^2}$$

$$\sigma_{cGFRP} := \left(\frac{743.9746}{2.3}\right)^{\frac{3}{2}} = 5817.6208 \quad \frac{lb}{in^2} \qquad increase := \frac{\left(5817.621 - \sigma_{tested}\right)}{\sigma_{tested}} \cdot 100 = 93.9207\,\%$$

Average Possible Concrete Strength Between Both Tests

$$GFRP := 5124.6148$$
$$Steel := 4012.6918$$

$$\sigma_{average} := \frac{GFRP + Steel}{2} = 4568.6533 \quad \frac{lb}{in^2} \qquad increase := \frac{\left(\sigma_{average} - \sigma_{tested}\right)}{\sigma_{tested}} \cdot 100 = 52.2884\,\%$$

The final concrete strength at time of testing was close to 4567 lb/in^2, a 52% increase from the 28 day strength.

Figure G.1 Compressive Strength Hand Check

APPENDIX H. THEORETICAL STRAIN VERIFICATION

Uncracked concrete section

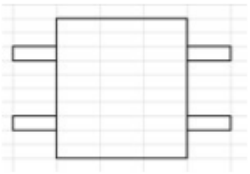

$f'c := 3000\ psi$

$E_s := 29000\ ksi$

$w_c := 150\ \frac{lb}{ft^3}$

$E_c := \frac{57000 \cdot \sqrt{f'c}}{1000} = 3122.0186\ ksi$

$n := \frac{E_s}{E_c} = 9.2889$

$y = \frac{\Sigma A_i \cdot y_i}{\Sigma A_i} \quad y := \frac{(12 \cdot 12 \cdot 6) + ((n-1) \cdot .2 \cdot 2) + ((n-1) \cdot .2 \cdot 2)}{(12 \cdot 12 + .2 + .2)} = 6\ in$

$I_{untr} = \Sigma I_i + A d_i^2$

$I_{untr} := \left(\frac{(12 \cdot 12^3)}{12}\right) + \left((n-1) \cdot .2 \cdot (6-2)^2\right) + \left((n-1) \cdot .2 \cdot (6-2)^2\right) = 1781.0487\ in^4$

$f_t := \frac{7.5 \cdot \sqrt{f'c}}{1000} = 0.4108\ ksi$

$M_{cr} := \frac{f_t \cdot I_{untr}}{y} = 121.3475\ k-in$

Moment uses the beam diagram shown to the right

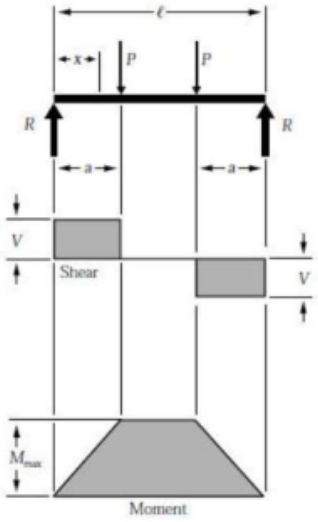

$F := 32000\ lbs \qquad a := 1\ ft \quad y_i := 4$

$P := \frac{F}{2} = 16000\ lbs$

$M := P \cdot a = 16000\ kft$

$M_{in} := M \cdot 12 = 1.92 \cdot 10^5\ k-in$

External Calculation

$\sigma_e := \frac{M_{in} \cdot y}{I_{untr}} = 649.9686\ psi$

Internal Calculation

$\sigma_i := \frac{M_{in} \cdot y_i}{I_{untr}} = 431.2066\ psi$

$E_c := w_c^{1.5} \cdot 33 \cdot \sqrt{f'c} = 3.3206 \cdot 10^6$

$\varepsilon_e := \frac{\sigma_e}{E_c} \cdot 1000000 = 195.7406\ \mu\varepsilon \qquad \varepsilon_i := \frac{\sigma_i}{E_c} \cdot 1000000 = 129.8596\ \mu\varepsilon$

Figure H.1 Theoretical Hand Check Strain Verification